NOVA SCHOOL OF SCIENCE & TECHNOLOGY

DEPARTMENT OF ELECTRICAL AND COMPUTER ENGINEERING

AFONSO FERNANDES OLIVEIRA

BSc in Electrical and Computer Engineering

DECISION SUPPORT PLATFORM FOR ENHANCED WILDFIRE PREVENTION AND MANAGEMENT

MASTER IN ELECTRICAL AND COMPUTER ENGINEERING

NOVA University Lisbon
September, 2023

NOVA SCHOOL OF
SCIENCE & TECHNOLOGY

DEPARTMENT OF ELECTRICAL
AND COMPUTER ENGINEERING

DECISION SUPPORT PLATFORM FOR ENHANCED WILDFIRE PREVENTION AND MANAGEMENT

AFONSO FERNANDES OLIVEIRA

BSc in Electrical and Computer Engineering

Adviser: Filipe de Carvalho Moutinho
Assistant Professor, School of Science and Technology, NOVA University Lisbon

Co-adviser: João Pedro Leal Abalada de Matos Carvalho
Assistant Professor, Universidade Lusófona

Examination Committee

Chair: Rui Manuel Leitão Tavares
Assistant Professor, FCT-NOVA

Rapporteur: André Teixeira Bento Damas Mora
Assistant Professor, FCT-NOVA

Member: João Pedro Leal Abalada de Matos Carvalho
Assistant Professor, Universidade Lusófona

MASTER IN ELECTRICAL AND COMPUTER ENGINEERING

NOVA University Lisbon
September, 2023

Decision Support Platform for Enhanced Wildfire Prevention and Management

This document was created with the (pdf/Xe/Lua)LaTeX processor and the NOVAthesis template (v7.1.5) (Lourenço, 2021).

I dedicate this dissertation to my family, whose unwavering support and encouragement have been the driving force behind my academic journey.

Acknowledgements

I would like to express my deepest gratitude to the my advisors, professor Filipe Moutinho and professor João Carvalho, along with professor Nuno Fachada. Your expertise, insightful feedback, and constant encouragement were instrumental in shaping the direction and quality of this work.

I am grateful to NOVA School of Science and Technology, and COPELABS for providing a wonderful academic environment and resources essential for the successful completion of this dissertation and all scientific work derived from it. I would also like to thank Beyond Vision for providing the essential data so that this work could be realized.

Lastly, I would like to thank my family for their strength that has been my greatest motivation throughout this journey. And my friends, who kept me from descending into complete insanity. I am forever grateful for your support.

”

“Normal people [...] believe that if it ain’t broke, don’t fix it. Engineers believe that if it ain’t broke, it doesn’t have enough features yet.”

— Scott Adams, “The Dilbert Principle: a Cubicle’s-eye View of Bosses, Meetings, Management Fads & other Workplace Afflictions.” (Author and Cartoonist)

Abstract

The primary aim of this dissertation was to develop a comprehensive framework tailored for wildfire prevention and management, and forest rehabilitation, specifically designed to harness data collected from Unmanned Aerial Vehicles (UAV)s. This platform is intended to possess the capability to generate pertinent information about a given region and simulate wildfire incidents within that area.

The platform is composed of two independent modules—NABU and PYTHIA. The NABU module is responsible for extracting topographical and fuel data from the UAV-provided datasets, while PYTHIA is responsible for wildfire simulation.

The NABU module utilizes multispectral and LIDAR data to build region maps with good level of precision, and is able to characterize fuel with sufficient accuracy to generate dependable fuel maps for a given area without the need for external data sources. Furthermore, the inclusion of a weather data aggregation feature facilitates the generation of both historical and forecasted weather data on a global scale.

The PYTHIA module includes an implementation of the latest U.S. National Fire Danger Rating System model introduced in 2016, complemented by a cellular automation-based propagation system. Notably, this module has good accuracy, particularly concerning burn shape and overall fire direction when compared to the established FlamMap fire modeling software. Nevertheless, certain limitations associated with the speed and scalability of the simulations conducted within the PYTHIA. These shortcomings point to areas that warrant further refinement and optimization in future iterations. Nevertheless, the overall results obtained from PYTHIA are exceedingly encouraging, opening up a multitude of prospects for future research and development endeavors.

Keywords: Wildfire, Remote Sensing, Fire Modelling, Decision Support, Multispectral Imaging, Unmanned Aerial Vehicle

Resumo

O objetivo principal desta dissertação foi o desenvolvimento de uma plataforma de apoio à decisão para a prevenção, gestão e reabilitação de incêndios, especificamente concebida para aproveitar os dados recolhidos de drones. Pretendia-se que esta plataforma tenha a capacidade de gerar informação pertinente sobre uma determinada região e simular incêndios nessa área.

A plataforma é composta por dois módulos independentes—NABU e PYTHIA. O módulo NABU é responsável por extrair dados topográficos e de combustível dos conjuntos de dados fornecidos pelos drones, enquanto o PYTHIA é responsável pela simulação de incêndios.

O módulo NABU utiliza dados multiespectrais e LIDAR para criar mapas de uma região com um bom nível de precisão, e é capaz de caracterizar o combustível com precisão suficiente para gerar mapas de combustível para uma determinada área, sem a necessidade de fontes de dados externas. Além disso, a inclusão de uma funcionalidade de agregação de dados meteorológicos facilita a geração de dados meteorológicos históricos e previstos em escala global.

O módulo PYTHIA inclui uma implementação do modelo mais recente do *National Fire Danger Rating System* dos Estados Unidos introduzido em 2016 e complementado por um sistema de propagação baseado em automação celular. Notavelmente, este módulo possui boa precisão, especialmente no que diz respeito à forma de queima e à direção geral do incêndio, quando comparado ao estabelecido software de simulação de incêndios FlamMap. No entanto, existem certas limitações associadas à velocidade e escalabilidade das simulações realizadas dentro do PYTHIA. Essas limitações indicam áreas que merecem maior refinamento e otimização em futuras iterações. No entanto, os resultados gerais obtidos a partir do PYTHIA são extremamente encorajadores, abrindo uma série de perspetivas para futura pesquisa e desenvolvimento.

Palavras-chave: Incêndios Florestais, Sensoriamento Remoto, Modelação de Incêndios, Apoio à Decisão, Imagem Multispectral, Veículo Aéreo Não Tripulado

Contents

List of Figures

List of Tables

Acronyms

BAI Burning Area Index *(p. 20)*
BF Back Fire *(p. 49)*
BI Burning Index *(p. 53)*

CA Cellular Automation *(p. 21)*
CGFSM CSIRO Grassland Fire Spread Model *(p. 23)*
CIR Color-Infrared *(pp. 12, 13, 15, 16, 40)*
CNN Convolutional Neural Network *(pp. 19, 26, 27, 29)*

DEM Digital Elevation Model *(pp. 5, 7, 13, 14, 19, 24, 29)*
DNN Deep Neural Network *(p. 26)*
DSM Data Surface Model *(pp. 35, 44)*
DTM Data Terrain Model *(pp. 35, 41, 44)*
DVI Difference Vegetation Index *(pp. 18, 19)*

EFFIS European Forest Fire Information System *(p. 2)*
EO Earth Observation *(p. 28)*
EU European Union *(p. 2)*
EVI Enhanced Vegetation Index *(pp. 16, 18)*

FARSITE Fire Area Simulator *(p. 24)*
FNC Fully Convolution Network *(p. 26)*
FVC Fraction of Vegetation Cover *(p. 18)*

GARI Green Atmospherically Resistant Vegetation Index *(p. 41)*
GDAL Geospatial Data Abstraction Library *(p. 39)*
GNDVI Green Normalized Difference Vegetation Index *(p. 19)*

HEVI2 Hotspot-Signature 2-Band Enhanced Vegetation Index *(p. 18)*

HF Head Fire *(p. 49)*
HSVI Hotspot-Signature Soil-adjusted Vegetation Index *(p. 18)*

IDVI Inverted Difference Vegetation Index *(p. 16)*
IQR Interquartile Range *(p. 40)*

JRC Joint Research Centre *(p. 8)*

LAI Leaf Area Index *(pp. 16, 18)*
LANDFIRE Landscape Fire and Resource Management Planning Tools *(p. 27)*
LEO Low Earth Orbit *(p. 27)*
LIDAR Light Detection and Ranging *(pp. 4, 5, 7, 13, 14, 24)*
LOD Levels of Detail *(p. 24)*
LSTM Long Short-Term Memory *(p. 21)*

MSAVI Modified Soil-Adjusted Vegetation Index *(p. 19)*
MSE Mean Squared Error *(p. 22)*
MSR Modified Simple Ratio Vegetation Index *(p. 18)*
MVS Multi-View Stereo *(p. 25)*

NBR Normalized Burn Ratio Index *(p. 20)*
NBRT1 Normalized Burn Ratio Thermal Index *(p. 20)*
NDRE Normalized Difference Red Edge Index *(pp. 16, 18)*
NDVI Normalized Difference Vegetation Index *(pp. 13, 16, 18–20, 44)*
NDWI Normalized Difference Water Index *(pp. 16, 18–20, 41)*
NFDRS National Fire Danger Rating System *(pp. 5, 47)*
NHVI2 Normalized Hotspot-Signature Vegetation Index 2 *(p. 18)*
NIR Near Infra-Red *(pp. 13, 19, 28, 35, 39, 40)*
NWCG National Wildfire Coordinating Group *(p. 33)*

OSAVI Optimized Soil-Adjusted Vegetation Index *(p. 19)*
OSG OpenSceneGraph *(p. 24)*

REI Road Extraction Index *(p. 20)*
ROS Rate of Spread *(pp. 21, 49, 50, 61, 68)*
RVI Radio Vegetation Index *(pp. 16, 18)*

SAVI Soil-Adjusted Vegetation Index *(pp. 18–20)*
SFIDE Satellite FIre DEtection *(p. 28)*
SfM Structure-from-Motion *(p. 25)*

SR Simple Ratio Vegetation Index *(p. 19)*
SWIR Short-Wave Infrared *(p. 20)*
SZA Solar Zenith Angle *(p. 18)*

TAVI Topography-Adjusted Vegetation Index *(pp. 18, 19)*

UAV Unmanned Aerial Vehicles *(pp. ix, 4, 25, 26, 28, 30, 34, 67)*
UPDM Universal Pattern Decomposition Method *(p. 18)*

VI Vegetation Index *(pp. 13, 16)*
VIUPD Vegetation Index Based on Universal Pattern Decomposition Method *(p. 18)*
VWC Vegetation Water Content *(p. 18)*

1 Introduction

Wildfires are one of the most devastating natural disasters, inflicting profound devastation upon human and animal ecosystems alike. Moreover, given the exacerbation of fire-prone conditions attributable to climate change and the growing contributory role of human activities, the need for efficient measures aimed at wildfire prevention and management has reached an unprecedented level of urgency.

This chapter serves as an introductory note to the document, providing an overview of the impact of wildfires (Section 1.1). It also presents concerning statistics from recent years (Section 1.2). Furthermore, it briefly discusses current conventional approaches to wildfire response (Section 1.3). The chapter then outlines the objectives of this work (Section 1.4) and concludes by providing an overview of the document's structure (Section 1.5).

1.1 Wildfire Impact

Wildfires possess a formidable capacity to wreak havoc on ecosystems. Forests, in particular, serve as critical biodiversity hot-spots and contribute significantly to carbon sequestration. When affected, these ecosystems can suffer near irreparable damage, leading to long-term ecological disruptions and the release of substantial amounts of greenhouse gases. The recovery process is often slow, extending from a few decades to well over a century in extreme cases.

Beyond their ecological implications, wildfires engender profound economic consequences. The destruction of resources and infrastructure results in substantial financial losses for individuals, communities, and governments. Industries such as forestry, agriculture, and tourism, experience direct revenue losses, while associated sectors suffer from reduced economic activities. Additionally, the costs associated with traditional fire suppression efforts, emergency response, and post-fire rehabilitation can set significant burdens on public budgets.

Moreover, wildfires also pose substantial risks to public health. Wildfire smoke contains a mixture of toxic pollutants and fine particulate matter, which have severe detrimental effects on the respiratory and cardiovascular systems. Prolonged exposure

can result in increased morbidity and mortality rates, especially among vulnerable populations such as children, the elderly, and individuals with pre-existing conditions, thereby burdening healthcare systems.

1.2 Escalating Severity of Wildfires in Recent Years

In recent decades, the devastating impact of wildfires has exhibited an alarming and escalating trend, reaching unprecedented and unsustainable levels. This mounting phenomenon has been exacerbated by the increasing prevalence of extreme weather occurrences, such as severe heatwaves and droughts. Consequently, these events have imposed significant strains on existing wildfire prevention and combat strategies.

As of 2022, the United States has experienced a substantial and consistent increase of over 200% in the number of recorded wildfires and a 500% increase in the area burned over the past four decades (National Interagency Fire Center, 2022). This upward trend highlights the emergence of particularly devastating wildfires in recent years, resulting in significant financial losses. The costliest years in US history, excluding indirect damages, were estimated to be 2017 ($21.4 billion), 2018 ($27.8 billion), and 2020 ($18.4 billion) (Smith, 2020). This alarming situation is especially pronounced in warm states like California, where nearly half of the state's twenty largest wildfires have occurred within the past five years (California Department of Forestry and Fire Protection, 2022).

Similarly, the European Union (EU) and neighboring countries face similar challenges. According to the European Commission's Joint Research Centre (Centre, 2021), the five southern EU member states, which typically bear the brunt of these disasters (see Tables 1.1 and 1.2), experience significant economic, humanitarian, and environmental losses each year.

Considering the recovery period required after a wildfire event to allow further damage to the same geographical area, many countries exhibit a slow declining trend in the extent of land affected by such incidents, although the absolute area remains alarmingly high. However, it is noteworthy that the number of wildfires has shown a relatively stable pattern. In this context, Portugal emerges as a notable exception within the framework of the European Forest Fire Information System (EFFIS), which encompasses 43 constituent states. Despite Portugal's landmass accounting for less than 3% of the total territory of the EU, the country experiences a disproportionately high frequency of forest fires and associated burnt areas, with an upward trajectory in recent times.

Over the past four decades alone, the cumulative area consumed by wildfires in Portugal has exceeded 50% of its entire territory, representing approximately 27% of the total land scorched in the five most severely affected EU member states.

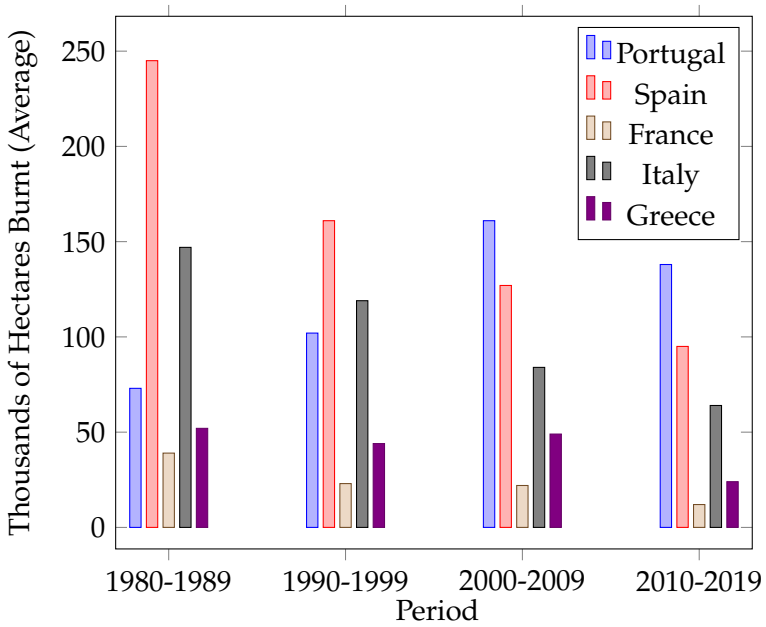

Figure 1.1: Average Burnt Area (in thousands of hectares) in the Five Most Affected EU Member States. Adapted from Centre, 2021.

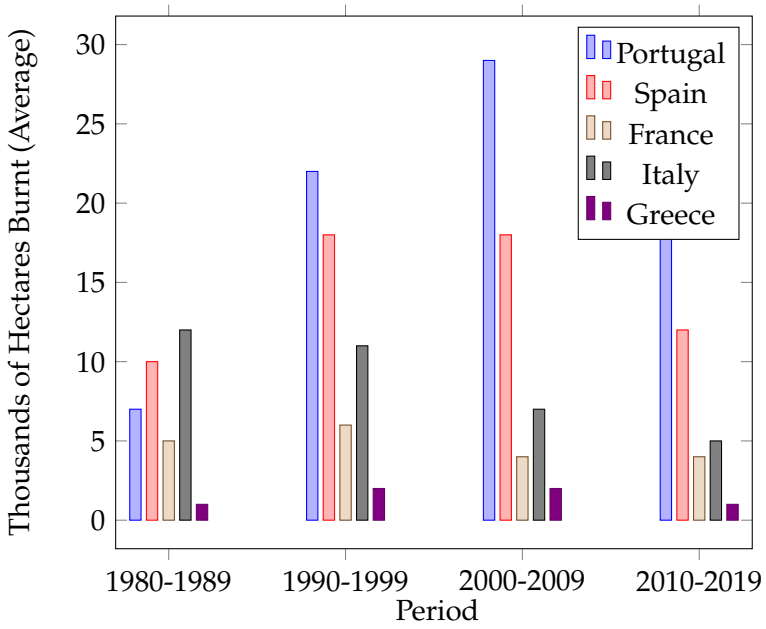

Figure 1.2: Average Number of Wildfires (in thousands of occurrences) in the Five Most Affected EU Member States. Adapted from Centre, 2021.

1.3 Conventional Approaches to Wildfire Action

Conventional approaches to wildfire action typically involve a combination of strategies centered on preemptive measures, early detection, effective management, and subsequent rehabilitation efforts.

Preventive measures constitute a comprehensive array of strategies, spanning from

educational and awareness-raising initiatives to legislative and regulatory measures. Complementary to these sociocultural endeavors, direct approaches such as forest clearing and other fuel management endeavors are also actively employed.

The early detection and quick response to wildfires hold paramount significance in ensuring their effective mitigation in their early stages. Fire lookouts are often employed in this process and although technological methodologies exist for the purpose of early fire detection, their implementation remains relatively limited as we'll see further in this document.

Firefighting forces play a pivotal role in the forefront of active wildfire management, assuming the primary responsibility for mitigating and suppressing these destructive events. This arduous task necessitates the deployment of trained firefighters, along with the utilization of aerial resources and ground equipment, in an effort to effectively contain and extinguish the fire. To optimize their efforts, authorities employ established strategies that have proven to be effective in combating wildfires.

Rehabilitation assumes paramount significance in the preservation and reestablishment of both natural ecosystems and human activities. These endeavors encompass a range of interventions, encompassing soil stabilization initiatives, reforestation endeavors, and strategic seed dispersal, among others.

It is evident that existing strategies and methods have been established to address various stages of wildfire response. Nevertheless, given the escalating frequency and severity of these incidents, it is crucial to enhance these approaches by utilizing all available resources.

The present circumstances inherently require a meticulous and inclusive reevaluation and modernization of endeavors pertaining to wildfire response. The exigency surrounding this issue imposes an obligation to undertake an exhaustive scrutiny of current approaches, with the aim of identifying domains that can be improved and formulating strategies for effecting such improvements.

1.4 Objectives

Given the previously highlighted severity of extreme wildfire occurrences and the pressing necessity to innovate and advance strategies for addressing them, this document strives to present a comprehensive decision-support platform geared towards wildfire prevention, early detection, effective management, and efficient rehabilitation.

The proposed platform would be equipped with advanced capabilities for analysis, including the generation of fuel and topographical maps. These functions would be specifically designed for the utilization of spectral and Light Detection and Ranging (LIDAR) data collected by UAVs. This data would allow the platform to perform the computation of wildfire simulations within specific areas of interest, depicting the overall progression and movement tendencies of wildfires. Additionally, the platform should

have the ability to provide wildfire danger insights, thereby providing valuable data to support wildfire management efforts.

1.5 Document Structure

This document consists of six chapters and five appendices, which are organized as follows:

Chapter 1: Introductory analysis of historical and recent trends of wildfire occurrences, exploring their severe impact and delineating avenues for investigation and development, followed by the objectives and organization of this document.

Chapter 2: Established theoretical concepts and technologies necessary for the better understanding of this work, including wildfire emergence and spread, remote sensing, multispectral imaging, LIDAR and Digital Elevation Models (DEMs).

Chapter 3: State of the art that presents the development in the fields of feature extraction, primarily through the utilization of multispectral imagery. It also includes the latest developments in wildfire modeling, simulation, and representation solutions, as well as available wildfire support frameworks.

Chapter 4: Methods employed during the development of this platform, along with essential elements to be applied during the implementation phase.

Chapter 5: Detailed records detailing the implementation of the platform system through two distinct modules, followed by the results of the validation phase.

Chapter 6: Conclusions of the developed work, accompanied by its contributions made and prospects for further future work, culminating in a few closing remarks.

Apendix A: Complete output of the NABU module for Map A.

Apendix B: Complete output of the NABU module for Map B.

Apendix C: Complete output of the NABU module for Map C.

Apendix D: List of equations that characterize the National Fire Danger Rating System (NFDRS) 2016 fire model.

Apendix E: Detailed specifications of the developed fuel model elements.

2

Theoretical Concepts and Technology

Given the growing wildfire threats, it's essential to gain a deep understanding of the core theoretical principles and the latest technologies that align with wildfire management before embarking on any development effort. This chapter aims to thoroughly explore the underlying mechanisms responsible for the emergence and behavior of wildfires (Section 2.1), followed by a concise overview of the field of remote sensing (Section 2.2). Subsequently, we will delve into the topics of multispectral imaging (Section 2.2.1), as well as the utilization of LIDAR and DEMs (Section 2.2.2).

2.1 Wildfire Emergence and Behaviour

Understanding the origins and dynamics of wildfires is crucial in the ongoing battle against these devastating phenomena. In this section, an extensive review of existing literature (de Castro et al., 2006; Gboloo, 2017; The National Wildfire Coordinating Group, 2019) is undertaken to provide a comprehensive understanding of the mechanisms of ignition (Section 2.1.1) and explore the multitude of factors that influence the spread of wildfires (refer to Section 2.1.2). By delving into these aspects, we can enhance our knowledge of the origins of wildfires and gain valuable insights into the patterns that govern their propagation. Equipped with this knowledge, we can develop effective strategies and implement measures to mitigate the impact of wildfires, protect vulnerable areas, and safeguard both the environment and human lives.

2.1.1 Ignition

Wildfires can be initiated by either natural or human-induced ignition sources. Natural ignition mechanisms, though rarer, include lightning strikes, volcanic activity, and spontaneous combustion. On the other hand, human-induced ignition mechanisms involve a wide range of factors.

Examples of human-induced ignition sources for wildfires include improperly extinguished campfires, discarded cigarette butts, and electrical malfunctions. These seemingly small and careless events can easily spark a wildfire. Arson, the intentional act of setting

fires, is also an alarming cause. Additionally, the use of industrial machinery, fireworks, and even some careless agricultural practices in highly flammable areas can also significantly increase the risk of ignition. Human negligence, which encompasses actions like disregarding fire safety guidelines or mishandling fire, plays a great role in wildfire occurrences. According to a report by the Joint Research Centre (JRC) in 2021, in Portugal, negligence was responsible for a staggering 50% of wildfires, followed by malicious acts accounting for 38% (Centre, 2021).

It is important to note that wildfires do not solely rely on ignition sources to occur. Several factors, such as fuel availability, weather conditions, and a receptive environment, also play crucial roles. To effectively prevent and minimize wildfires, responsible behavior, implementation of fire safety measures, and increased awareness are essential.

2.1.2 Spread Influencing Factors

2.1.2.1 Fuel

Fuel plays a critical role in shaping the behavior and progression of wildfires, encompassing a range of combustible materials that sustain and propagate fires, including vegetation, dead organic matter, and other flammable substances. Understanding the impact of fuel on the spread of wildfires is essential for predicting fire behavior, developing effective fire management strategies, and mitigating the risks associated with these devastating events.

Various fuel characteristics, including fuel type, moisture content, arrangement, and continuity, exert a significant influence on how wildfires develop and spread. Different types of fuel, such as grasses, shrubs, and trees, exhibit distinct combustion rates, heat release potentials, and burning characteristics. The moisture content of fuel plays a crucial role because dry fuel ignites more easily and burns more intensely compared to moist fuel.

The spatial distribution and arrangement of fuel elements, such as the proximity and configuration of trees and shrubs, can affect the rate and direction of fire spread. Fuel continuity refers to the connectivity and uninterrupted distribution of flammable materials. A continuous fuel bed enables fire to spread rapidly and cover extensive areas, while breaks or gaps in fuel can impede or restrict fire growth.

Moreover, fuel load, which represents the available fuel per unit area, is a vital consideration in understanding wildfire behavior. Higher fuel loads provide more material for combustion, resulting in increased fire intensity and a higher potential for rapid spread. Fuel load is influenced by factors such as vegetation density, fuel accumulation rates, and land management practices.

Dead fuel, including fallen leaves, twigs, branches, decaying plant matter, dead trees, snags, and logs, contributes significantly to the fuel load. It is particularly important because it serves as readily available fuel for ignition and combustion. Dead vegetation tends to have lower moisture content than live vegetation, making it more susceptible to ignition and contributing to the spread of wildfires.

Live fuel, including vibrant vegetation like trees and shrubs, plays a significant role in fuel accumulation within an ecosystem. While live fuel typically possesses high moisture content, acting as a natural deterrent to the spread of fires, it can become more susceptible to combustion under certain circumstances. During droughts, extended dry periods, or even during an ongoing blaze, live fuel experiences a reduction in moisture content, thereby intensifying its flammability. This decrease in moisture content contributes to the overall fuel load, exacerbating the potential for fire spread and intensifying the risk of wildfires.

2.1.2.2 Topography

The influence of topography on wildfire spread is a critical and multifaceted factor that significantly impacts the behavior and severity of wildfires. Topography encompasses various physical characteristics of the land, including elevation, slope, and the presence of natural features such as valleys, canyons, and water bodies.

Slope plays an incredibly important role in determining the spread of wildfires. Steep slopes can accelerate fire spread as flames travel more rapidly uphill. When combined with wind, steeper slopes create a chimney effect, drawing flames uphill and rapidly extending the fire front. Furthermore, the aspect, or orientation, of slopes affects the duration and intensity of solar radiation, which in turn impacts fuel moisture content and ignition potential.

Water features such as rivers, lakes, and reservoirs have also a significant impact on wildfire spread. Firstly, these natural water bodies act as effective firebreaks, significantly slowing down or even stopping the advance of the fire. Firefighters can strategically use these water features to establish containment lines, effectively preventing the fire from spreading further. Additionally, the presence of water in the surrounding area can lead to an increase in humidity levels. This higher humidity makes it more challenging for the fire to ignite and sustain itself. The moisture in the air reduces the overall flammability of the vegetation, acting as a natural deterrent to the fire's progression.

Complex topography distributions can give rise to intricate fire behavior patterns. In mountainous regions, wildfires often display extreme behaviors as a result of the interplay between various topographic features. The convergence of wind and the presence of ridges, canyons, and saddles can generate forceful gusts and turbulence, causing embers and burning debris to be propelled across the terrain. This dynamic fire movement leads to rapid spread in multiple directions, presenting significant challenges for firefighting operations.

Furthermore, topography influences the formation of fire-induced weather phenomena. When a wildfire spreads uphill, it has the potential to create a unique localized weather system called a pyrocumulus cloud. Pyrocumuli can give rise to powerful updrafts, turbulent winds, and even lightning, all of which contribute to the heightened intensity of the fire. These atmospheric conditions significantly exacerbate the challenges confronted

by firefighters, thereby amplifying the complexity and hazards associated with firefighting operations.

Finally, the role of topography in fire suppression strategies cannot be overstated. Firefighters can strategically utilize natural features such as ridges, roads, and rivers as effective firebreaks or control lines, effectively halting or redirecting the spread of wildfires. The consideration of topography is a critical aspect of containment planning, as firefighters leverage favorable terrain to establish safe zones, access points, and escape routes.

2.1.2.3 Weather

The role of weather in wildfire spread and behavior is crucial. Various factors, including temperature, humidity, wind speed, and precipitation, have significant impacts on the intensity and direction of wildfires. These factors not only affect firefighting efforts but also have consequences for the affected areas.

Temperature plays a vital role in wildfire behavior. High temperatures contribute to increased vegetation dryness, making it more susceptible to ignition. Additionally, they create favorable conditions for rapid fire growth by accelerating moisture evaporation. In extreme cases, high temperatures can lead to more intense and faster-spreading fires that are difficult to control.

Humidity levels also influence wildfire behavior. When combined with high temperatures, low humidity quickly draws moisture out of vegetation, providing abundant fuel for fires. Conversely, higher humidity reduces flammability and can impede the spread of fires. However, high humidity can also cause smoke to linger near the ground, impacting visibility and firefighting efforts.

Wind speed and direction are critical factors in determining the paths and rates of spread for wildfires. Strong winds carry embers and burning debris, allowing fires to jump containment lines and spread rapidly. These winds can accelerate fire spread by pushing flames into unburned areas and increasing the oxygen supply. Unpredictable wind patterns pose challenges to firefighting operations and increase risks to firefighters and communities.

Finally, precipitation, or the lack thereof, also significantly influences wildfire behavior. Drought and minimal rainfall contribute to highly flammable vegetation, facilitating fire ignition and spread. Conversely, heavy precipitation reduces vegetation flammability and slows down the progression of fires. However, even in wetter conditions, if followed by a dry period, increased plant growth can raise the fuel load, potentially exacerbating fire risks in the long term.

2.1.2.4 Artificial Structures

The presence of artificial structures in wildfire-prone areas has emerged as a significant factor influencing the behavior and intensity of these devastating events. In particular, structures constructed with flammable materials can act as ignition sources for wildfires.

Embers and radiant heat can travel significant distances, landing on or near structures and rapidly igniting them, thereby providing a continuous fuel source for the fire. As a result, the proximity of buildings to flammable vegetation significantly increases the risk of ignition and subsequent spread of wildfires.

Moreover, buildings, roads, and other infrastructure can create interconnected pathways that facilitate the spread of wildfires. These pathways serve as channels for flames and embers, allowing fires to leap across distances that would otherwise be difficult for flames alone to reach.

However, it is worth noting that roads can also play a crucial role as invaluable firebreaks in the battle against wildfires. Well-planned road networks can act as barriers, impeding the progress of flames and providing access for fire suppression activities. Furthermore, roads can facilitate the safe evacuation of residents and enable the smooth movement of firefighting personnel and equipment.

2.2 Remote Sensing

Remote Sensing involves the collection of information about a region, object or phenomenon without direct contact. Although this document focuses on the application of remote sensing to Earth, it is worth noting that this scientific discipline can also be utilized for studying celestial bodies.

The fundamental process of remote sensing can be understood as a two-step flow: data acquisition followed by data analysis. This concept is elaborated upon in the book *Remote Sensing and Image Interpretation* (Lillesand et al., 2015). While this document primarily emphasizes sensing methods based on electromagnetic energy, it is important to acknowledge the existence of other data sources, including acoustic and geodetic measurements.

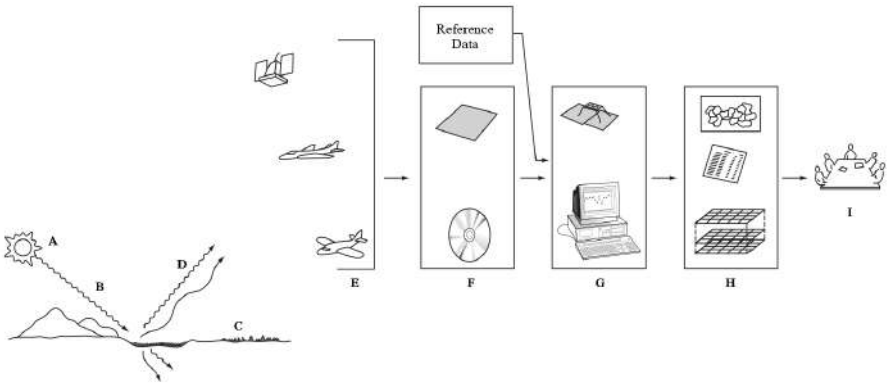

Figure 2.1: Remote Sensing Flow Example. Adapted from Lillesand et al., 2015.

To illustrate the process, refer to Figure 2.1. Remote sensing begins with a source of energy, typically electromagnetic radiation from the Sun (A). This energy travels through the atmosphere (B), undergoing scattering, until it reaches the Earth's surface.

The energy interacts with surface features (C) and is subsequently re-transmitted back into the atmosphere (D). Sensing technology (E) captures this energy and compiles it into data (F), which reflects the nature of the surface features. The generated data is then interpreted, analyzed (G), and compiled (H) into a user-friendly format that can be utilized by end-users (I).

Data acquisition in remote sensing is a multifaceted process that encompasses a range of methods, processes, and technologies employed to capture signals that faithfully represent real-world physical phenomena. Within this domain, two primary types of sensing instruments are utilized: active and passive (examples of which can be seen in Table 2.1).

Passive instruments depend on natural energy, such as sunlight, that is either reflected or emitted by the target of interest. As a result, they require favorable conditions to achieve accurate results.

In contrast, active sensors produce and emit a signal directed towards the target, and then receive the signal reflected or scattered back. Unlike passive instruments, active sensors are not constrained by external energy sources and are relatively unaffected by atmospheric scattering. This characteristic grants them greater versatility in their applications. Although the specific source of the signal varies among sensor types, the remaining processes involved in remote sensing remain largely consistent.

Table 2.1: Active and passive sensor examples

Active	**Passive**
Radar	Spectrometer
Lidar	Radiometer
Scatterometer	Accelerometer
Sonar	Sonar

2.2.1 Multispectral Imaging

Multispectral imaging is an immensely powerful methodology that extends our ability to capture information beyond the limits of the visible spectrum. Splitting the electromagnetic spectrum into distinct bands, multispectral imaging unveils hidden details that would otherwise remain unseen. These band names are commonly standardized across the industry, although their specific ranges may vary depending on the imaging instrument employed.

This document specifically focuses on five crucial bands: red, blue, green, near-infrared, and red-edge, with occasional outliers when deemed relevant. To provide a concrete illustration, we present the spectral specifications for the Micasense RedEdge-MX Camera in Table 2.2.

This document focuses on two key techniques for manipulating multispectral bands: Color-Infrared (CIR) imagery and multispectral indices.

Table 2.2: Spectral specifications of the Micasense RedEdge-MX camera

Band	**Range**
Blue	$475 \pm 20nm$
Green	$560 \pm 20nm$
Red	$668 \pm 10nm$
Red Edge	$717 \pm 10nm$
Near Infra-Red (NIR)	$840 \pm 40nm$

CIR is a multispectral processing technique that involves translating NIR information into the visible spectrum by combining the red, green, and NIR bands. This approach generates imagery that can be analyzed independently or subjected to further processing methods.

Multispectral indices, on the other hand, are composites of spectral bands that are specifically designed to enhance particular details in an image. This enhancement serves to increase the quantity and quality of data that can be extracted from the image. While some indices have a general purpose, others are tailored for specific objectives, such as the Vegetation Index (VI).

Further along in this document, we present a comprehensive list of widely used indexes, which have been evaluated and analyzed in terms of their applicability for assessing density performance, topographical aspects, and atmospheric resistance.

Assessing the effectiveness of an index for evaluating vegetation coverage heavily relies on the examination of density performance. A high-performance rating for a specific density level indicates that the index provides a more accurate representation of vegetation when applied to areas with similar density. One prominent index in widespread use is the Normalized Difference Vegetation Index (NDVI), which utilizes the reflective and absorptive properties of the chlorophyll pigment to augment vegetation details. However, the suitability of the NDVI is directly dependent on the density of chlorophyll-rich vegetation in an area, rendering it less effective in areas devoid of this pigment.

Topographic and atmospheric resistance are significant factors that can impact the accuracy and reliability of vegetation indices. Topographic resistance refers to the influence of terrain features, such as slopes and shadows, on vegetation indices. These features can affect the availability of sunlight and alter reflectance values. On the other hand, atmospheric resistance arises from atmospheric conditions, including aerosols and clouds, which distort solar radiation, resulting in errors in reflectance measurements. To address these challenges, methods like topographic normalization and atmospheric correction algorithms are utilized to enhance the precision of vegetation indices.

2.2.2 LIDAR Sensing and Digital Elevation Models

A thorough grasp of LIDAR sensing and DEMs is essential to fully comprehend the document and broaden our overall understanding.

LIDAR sensing is a remote sensing technique that utilizes laser light to measure distances and generate highly accurate three-dimensional representations of surfaces. This method involves emitting laser pulses from an aircraft or satellite and measuring the time it takes for the pulses to return after interacting with objects on the ground. By employing LIDAR sensors, one can obtain intricate details about the terrain, vegetation, buildings, and other objects that would be difficult to acquire through alternative methods.

On the other hand, DEMs are digital representations of a terrain's topography and elevation. These renderings are created by compiling elevation data from various sources, including LIDAR. DEMs provide comprehensive frameworks for analyzing and understanding surface features such as mountains, valleys, rivers, and coastlines - serving as valuable tools for studying and interpreting the Earth's landscape.

The utilization of LIDAR sensing in generating DEMs offers numerous advantages in the field of remote sensing. One of the primary benefits is the ability to create high-resolution and highly accurate DEMs using LIDAR data. This is achieved by capturing millions of data points in the form of point clouds, allowing for precise elevation measurements with exceptional spatial resolution. Such detailed information proves particularly valuable in areas with complex terrain or dense vegetation, where traditional sources of elevation data may fall short.

Moreover, employing LIDAR for DEM generation allows for the extraction of additional terrain attributes beyond elevation. These include slope, aspect, and curvature, providing a more comprehensive understanding of the terrain characteristics. By utilizing LIDAR data, remote sensing applications can go beyond mere elevation representation and obtain detailed information about the shape and features of the terrain.

3

State of the Art

Building upon the paradigm previously discussed in this document, this state-of-the-art section aims to provide a comprehensive overview of cutting-edge technologies, strategies, and practices that are highly relevant to the objectives outlined in this document. This chapter begins with a detailed examination of feature extraction techniques (Section 3.1), including vegetation attributes, water features, soil characteristics, artificial surfaces, and burnt areas. Specifically, it emphasizes the utilization of aerial imagery and multispectral indices for enhanced analysis. Subsequently, the chapter delves into advanced modeling, simulation, and representation approaches for wildfire management (Section 3.2), followed by an exploration of several already existing wildfire support frameworks (Section 3.3). Finally, it provides a discussion on the findings of this chapter (Section 3.4).

3.1 Feature Extraction

Evaluating the behavior of wildfires requires a comprehensive analysis of the spatial properties surrounding their occurrence. At the core of this analysis lies a deep understanding of the terrain characteristics within the affected region. As previously discussed, factors such as slope, elevation, and the arrangement of fuel significantly influence the progression of the fire.

Therefore, this section focuses on the utilization of two multispectral data processing techniques - color-infrared imagery and multispectral indices - to facilitate the extraction of relevant feature data. While there are multiple facets to consider in this endeavor, the document prioritizes the most pressing and significant aspects: vegetation attributes, water features, soil characteristics, artificial surfaces, and areas already affected by fire.

Lastly, it is important to note that all the image examples presented in this chapter were generated using internal data sources.

3.1.1 Color-Infrared Imagery

Utilizing CIR imagery for feature extraction offers numerous advantages over traditional visible color composites. This imaging method improves the differentiation among various

types of vegetation, soil compositions, water features, and even distinct human-made structures.

When examining CIR imagery, dense and healthy vegetation appears as vibrant red colors, which gradually shifts towards shades of pink as the health of the vegetation diminishes. Ultimately, deceased plants display shades encompassing green, cyan, and tan tones. The colors exhibited by bare soil depend on its composition. Clay soils appear as darker shades of tan and cyan, while sandy soils tend to display lighter shades of tan, gray, or white. The presence of moisture and the concentration of organic content within the soil can also darken its appearance in a CIR image.

Water generally appears as shades of blue and black, depending on its transparency. However, for shallow streams, the appearance of the water is directly related to the composition of the stream bed soil. The appearance of human-made structures in CIR images can significantly differ depending on their material composition. For example, gravel roads often exhibit a light color, while asphalt roads display various shades of dark blue and black.

3.1.2 Multispectral Indices

This field of study is constantly evolving, with new developments and advancements shaping its progress. Despite the rapid changes, there are certain indices that have stood the test of time and remain fundamental to this day. Table 3.1 presents a curated selection of these indices, chosen based on their relevance and as examples of notable advancements in the field. Each index is accompanied by its general formula and reference to the original study where they were introduced.

3.1.2.1 Vegetation Attributes

The utility of the NDVI is limited due to saturation in highly vegetated areas and inconsistency in highly arid regions (Mummoorthy et al., 2019).

In comparison to non-ratio indices like the Enhanced Vegetation Index (EVI), ratio indices such as NDVI, Normalized Difference Water Index (NDWI), and Normalized Difference Red Edge Index (NDRE) were found to reduce topographic effects to some extent (Zhou and Chen, 2019).

Several studies (Gonenc et al., 2019; Salvado et al., 2019) have demonstrated that the NDVI can serve as a viable alternative to the Radio Vegetation Index (RVI) since it relies solely on waveband data and produces similar results.

The Inverted Difference Vegetation Index (IDVI) offers advantages over NDVI as it is insensitive to leaf biochemical parameters and exhibits a wider variation range. Furthermore, a statistical model combining NDVI and IDVI, incorporating a dynamic scale factor, was shown to achieve more accurate and robust Leaf Area Index (LAI) estimation compared to single VI regression models (Kalpoma et al., 2019; Sun et al.,

Table 3.1: Considered multispectral indices.

Index	Formula	Reference
SR	$\frac{\rho_{NIR}}{\rho_R}$	Birth and McVey, 1968
NDVI	$\frac{\rho_{NIR}-\rho_R}{\rho_{NIR}+\rho_R}$	Rouse et al., 1974
DVI	$\rho_{NIR} - \rho_R$	Tucker, 1979
MSR	$\frac{\frac{\rho_{NIR}}{\rho_R}-1}{\sqrt{\frac{\rho_{NIR}}{\rho_R}+1}}$	J. M. Chen, 1996
GNDVI	$\frac{\rho_{NIR}-\rho_G}{\rho_{NIR}+\rho_G}$	Gitelson et al., 1996
NDRE	$\frac{\rho_{NIR}-\rho_{RE}}{\rho_{NIR}+\rho_{RE}}$	E. Barnes et al., 2000
IDVI	$\frac{1+(\rho_{NIR}-\rho_R)}{1-(\rho_{NIR}-\rho_R)}$	Sun et al., 2018
EVI	$\frac{2.5\times(\rho_{NIR}-\rho_R)}{\rho_{NIR}+6\times\rho_R-7.5\times\rho_B+1}$	H. Q. Liu and Huete, 1995
EVI2	$\frac{2.5\times(\rho_{NIR}-\rho_R)}{\rho_{NIR}+2.4\times\rho_R+1}$	Z. Jiang et al., 2006
SAVI	$1.5 \times \frac{\rho_{NIR}-\rho_R}{\rho_{NIR}+\rho_R+0.5}$	Huete, 1988
MSAVI	$\frac{2\times\rho_{NIR}+1-\sqrt{(2\times\rho_{NIR}+1)^2-8\times(\rho_{NIR}-\rho_{RED})}}{2}$	Qi et al., 1994
OSAVI	$1.16 \times \frac{\rho_{NIR}-\rho_R}{\rho_{NIR}+\rho_R+0.16}$	Rondeaux et al., 1996
TAVI	$\frac{\rho_{NIR}+f(\Delta)\times(M_R-\rho_R)}{\rho_R}$	H. Jiang et al., 2011
NDHD	$\frac{\rho_{HS}-\rho_{DS}}{\rho_{HS}+\rho_{DS}}$	Leblanc et al., 2001
NHVI2	NDVI × NDHD	Zhen et al., 2020
HSVI	SAVI × NDHD	Zhen et al., 2020
HEVI2	EVI2 × NDHD	Zhen et al., 2020
VIUPD	$\frac{C_V-0.1\times C_S-C_4}{C_W+C_V+C_S}$	Zhang et al., 2007
MBI	$\frac{\rho_{SWIR1}-\rho_{SWIR2}-\rho_{NIR}}{\rho_{SWIR1}+\rho_{SWIR2}+\rho_{NIR}} + 0.5$	Nguyen et al., 2021
EMBI	$\frac{MBI-MNDWI-0.5}{MBI+MNDWI+1.5}$	Zhao and Zhu, 2022
NDWI	$\frac{\rho_G-\rho_{NIR}}{\rho_G+\rho_{NIR}}$	Gao, 1996
MNDWI	$\frac{\rho_G-\rho_{SWIRL}}{\rho_G+\rho_{SWIRL}}$	H. Xu, 2006
NBR	$\frac{\rho_{NIR}-\rho_{SWIR}}{\rho_{NIR}+\rho_{SWIR}}$	García and Caselles, 1991
BAI	$\frac{1}{(0.1-R)^2+(0.06-NIR)^2}$	Chuvieco and Martín, 1998
NBRT1	$\frac{\rho_{NIR}-\rho_{SWIR}(\frac{\rho_{Thermal}}{1000})}{\rho_{NIR}+\rho_{SWIR}(\frac{\rho_{Thermal}}{1000})}$	Holden et al., 2005a
REI	$\frac{\rho_{NIR}-\rho_B}{\rho_{NIR}+\rho_B\times\rho_{NIR}}$	Shahi et al., 2015

ρ_B: Blue Band Reflectance
ρ_G: Green Band Reflectance
ρ_R: Red Band Reflectance
ρ_{RE}: Red-Edge Band Reflectance
ρ_{NIR}: Near Infra-Red Band Reflectance
ρ_{SWIR}: Short-Wave Infra-Red Reflectance
$\rho_{Thermal}$: Thermal Reflectance
ρ_{HS}: Hotspot Reflectance
ρ_{DS}: Darkspot Reflectance
C_V: Vegetation Reflectance Coefficient
C_S: Soil Reflectance Coefficient
C_W: Water Reflectance Coefficient
C_Y: Yellow Leaf Reflectance Coefficient
$f(\Delta)$: Topography Adjusting Coefficient
M_{RED}: Maximized Red Band Reflectance
$\phi(\#)$: Min–Max Normalization Function Based on the Entire Image

2018). However, single models and LAI still show high correlations particularly in the near-infrared, red, and blue spectral ranges (Jingguo et al., 2015).

A study (Yan et al., 2022) presented compelling findings regarding the estimation of Fraction of Vegetation Cover (FVC) using different models, with a particular focus on the Difference Vegetation Index (DVI). The study concluded that the DVI-based model exhibited the highest levels of accuracy and stability in estimating FVC. Moreover, the research demonstrated that the RVI and EVI models were considerably affected by theoretical uncertainty stemming from sensor characteristics. Conversely, the Normalized NDVI model exhibited a high sensitivity to variations in Solar Zenith Angle (SZA).

In the domain of LAI estimation, substantial research efforts have been dedicated to exploring various methodologies. Notably, multiple recent studies (Kang et al., 2016; S. Liu et al., 2021; Mourad et al., 2020) have contributed to this field and based on the existing literature, it is suggested thatNDVI outperforms glssr and Modified Simple Ratio Vegetation Index (MSR) based methods in accurately estimating LAI (Xie et al., 2014).

Notably, the NDWI demonstrates high precision when estimating plant Vegetation Water Content (VWC). Additionally, given that a plant's moisture content frequently reflects its condition, the NDWI can be relied upon as a trustworthy gauge of vegetation well-being (Lu et al., 2011).

The novel Vegetation Index Based on Universal Pattern Decomposition Method (VIUPD) is based on the Universal Pattern Decomposition Method (UPDM) (Zhang et al., 2003) for multispectral data. This index was formulated as a modification of the revised vegetation index, which was originally established using the UPDM as its foundation (Daigo et al., 2004), and its results demonstrate higher sensitivity to vegetation density compared to the NDVI and other common indices. While most of the complexity lies in the calculation of the coefficients, a later study (She et al., 2016) demonstrates the computation of these coefficients in a simple three-step process. VIUPD is an improvement to the NDVI, having a larger domain range and performing better in high vegetation cover areas. Compared to other common indices, the VIUPD demonstrates higher sensitivity to vegetation health and CO_2 concentration.

Within arid regions, the NDRE offers an alternative method for estimating the proportion of green vegetation, as opposed to relying on NDVI (Li et al., 2012).

In order to improve the accuracy and applicability of the Soil-Adjusted Vegetation Index (SAVI) for estimating vegetation in a heterogeneous canopy, several alternative indices have been developed and studied. These include the the Normalized Hotspot-Signature Vegetation Index 2 (NHVI2), the Hotspot-Signature Soil-adjusted Vegetation Index (HSVI), and the Hotspot-Signature 2-Band Enhanced Vegetation Index (HEVI2). These indices have shown consistent performance when compared to traditional multispectral vegetation indices and have demonstrated high resistance to soil noise (Zhen et al., 2020).

A particular index—the Topography-Adjusted Vegetation Index (TAVI)—was specially crafted to tackle the difficulties presented by uneven landscapes. Its primary objective is to mitigate the naturally occurring strong association between the cosine of solar incidence

and conventional vegetation indices, which has the potential to result in diminished accuracy. The proposed TAVI introduces two coefficients: M_{RED}, which represents the maximized value of the red waveband, and $f(\Delta)$, the topography adjusting coefficient. The coefficient $f(\Delta)$ was optimized to minimize the mean difference between darker and brighter inclines and was determined to be 2.280. Notably, the TAVI effectively mitigates topographic effects in rugged terrains by solely utilizing red and NIR band data, without requiring additional support from DEM data.

The results of the study demonstrate that the TAVI significantly enhances the estimation of vegetation in rugged terrains. By accounting for topographic influences and relying only on the red and NIR bands, the TAVI overcomes the limitations of traditional vegetation indices and provides more accurate assessments of vegetation cover and distribution in challenging environments. This advancement offers valuable insights for applications such as land management, ecological studies, and remote sensing analyses in rugged terrains.

3.1.2.2 Water Features

While the NDWI is widely recognized as a invaluable tool specifically designed for delineating water features, it is worth noting that the NDVI can also be effectively utilized for this purpose. The NDVI demonstrates its capability in successfully identifying water features as well.

3.1.2.3 Terrain Characteristics

Previous studies have proposed models using the NDVI and surface temperature for the estimation of soil moisture (Sandholt et al., 2002). However, more recent research has expanded on this approach by incorporating other indices, such as the Green Normalized Difference Vegetation Index (GNDVI), SAVI, Modified Soil-Adjusted Vegetation Index (MSAVI), and Optimized Soil-Adjusted Vegetation Index (OSAVI). These studies have demonstrated high accuracy in estimating soil moisture (Deng et al., 2023; Swain et al., 2021). Another promising approach involves utilizing multispectral data, including infrared and thermal information, in combination with advanced analysis techniques like Convolutional Neural Networks (CNNs) (Bertalan et al., 2022; Seo et al., 2021).

The organic matter content of soil can significantly impact wildfire behavior. Increased levels of organic matter elevate the amount of fuel present, rendering the soil more susceptible to ignition and exacerbating the impact of fires. These areas may experience deep-seated and persistent underground fires. Recent studies have shown promising results by employing combinations of Simple Ratio Vegetation Index (SR), DVI, NDVI, and GNDVI as auxiliary data in addressing this issue (Guo et al., 2020, 2021).

3.1.2.4 Artificial Surfaces

The proposed method in the Road Extraction Index (REI) shows promise in accurately capturing asphalt road networks during extraction. However, it is important to acknowledge certain limitations associated with this approach. Challenges arise when dealing with roads covered by trees or shadows, and there is also a possibility of misclassifying building boundaries as roads (Shahi et al., 2015).

Furthermore, the literature highlights that relying solely on single indices is insufficient for achieving accurate road extraction. To enhance the extraction process and reduce misclassifications, it is crucial to integrate advanced high-level vision algorithms. Studies have demonstrated that methods incorporating machine learning and data fusion techniques outperform single indices like NDVI, NDWI, and SAVI in terms of accuracy specifically for road extraction (Puttinaovarat and Horkaew, 2018).

3.1.2.5 Burnt Areas

The introduction of the Burning Area Index (BAI) has significantly enhanced the ease of estimating burnt areas, demonstrating its superior discrimination ability compared to the NDVI and SAVI (Chuvieco et al., 2002). However, it is prudent to exercise caution when employing the BAI for mapping burned land, as there is substantial variability within the areas affected by fire. To achieve accurate results, it is recommended to set stringent thresholds. Furthermore, the study suggests the potential inclusion of a shape refinement algorithm to further enhance result accuracy.

A subsequent study successfully integrated an approach based on the Normalized Burn Ratio Index (NBR), utilizing satellite imagery to identify the severity of burns (Key and Benson, 2006). This approach has demonstrated remarkable success, particularly in its ability to compare results and aggregate information across wide geographical areas and over time. It should be noted that this approach requires the utilization of the Short-Wave Infrared (SWIR) band, which can be costly to acquire.

Lastly, a study highlights the potential of the Normalized Burn Ratio Thermal Index (NBRT1) index, which incorporates a thermal component, in identifying lightly burned areas (Holden et al., 2005b). However, the study underscores the necessity for additional research to explore how the timing of post-fire image capture impacts the differentiation between burned and unburned regions when employing two- or three-dimensional indices.

3.2 Wildfire Modeling, Simulation and Representation

The study of wildfire behavioral patterns is an intricate area of research, characterized by a continuous evolution spanning nearly half a century. Throughout this time, numerous mathematical models have been developed with the aim of accurately characterizing the complex behaviors exhibited by wildfires. These models can be broadly classified as

empirical or physical, exhibiting substantial variations in their methodological approaches and levels of complexity. The present document centers its attention on a specific category of models known as *crown fire models*, which hold historical significance, serve as field-defining benchmarks, and are frequently cited in the literature (Rothermel, 1972; Wagner, 1977; Alexander, 1998). These models primarily focus on the computation of the Rate of Spread (ROS) and have consistently served as foundational frameworks upon which more sophisticated models are built. Furthermore, they find extensive application in simulation solutions, effectively facilitating accurate results.

In addition to simulation solutions, the representation of wildfires within a three-dimensional environment is of great importance within the scope of this document. Consequently, we also include a discussion on platforms that incorporate advanced renderization systems, as well as standalone rendering frameworks that exhibit promising potential for fulfilling the objectives of this study.

3.2.1 Simulation Based on Cellular Automaton

Cellular Automation (CA) is a computational model that utilizes a mathematical space divided into a regular grid of cells. Each cell has a finite number of states and is associated with a designated *neighborhood*. This model operates in a generational manner, updating the state of each cell at discrete moments based on a predefined *transference rule*, the current state of the cell, and the states of its neighboring cells.

A study (Yongzhong et al., 2004) demonstrated the direct implementation of a CA model for simulating wildfires. The model employed a hexagonal tessellation grid with a six-cell *neighborhood*. It integrated multiple established mathematical models for fire behavior, such as those proposed by (Rothermel, 1972, Gill et al., 1981, Weise and Biging, 1996, and Du Fei, 2001), to govern the interactions during the state transitions. The proposed model underwent verification and validation processes using controlled simulated environments to examine general variable interactions, as well as a case study based on a real wildfire incident, which yielded satisfactory results.

More recently, a novel solution (Li et al., 2022) was developed by combining CA with a Long Short-Term Memory (LSTM)-based speed model, aiming to simplify input complexity and address limitations identified in previous models. The developed S-LSTM model focuses on capturing the interplay between the ROS and the wind speed within the wildfire's zone of influence. It generates predictions for both parameters at each discrete moment. An illustration of the proposed solution's flow is presented in Figure 3.1.

The CA structure described in Li et al., 2022 is computed using the Moore *neighborhood*, where each cell is assigned one of three states: unburned, incomplete, or complete (spreadable), based on the fraction of its burned area (Rui et al., 2018). The *transference rule* is then determined by considering three coeficients:

$$V = V_c \cdot K_{evc} \cdot K_{slope}$$

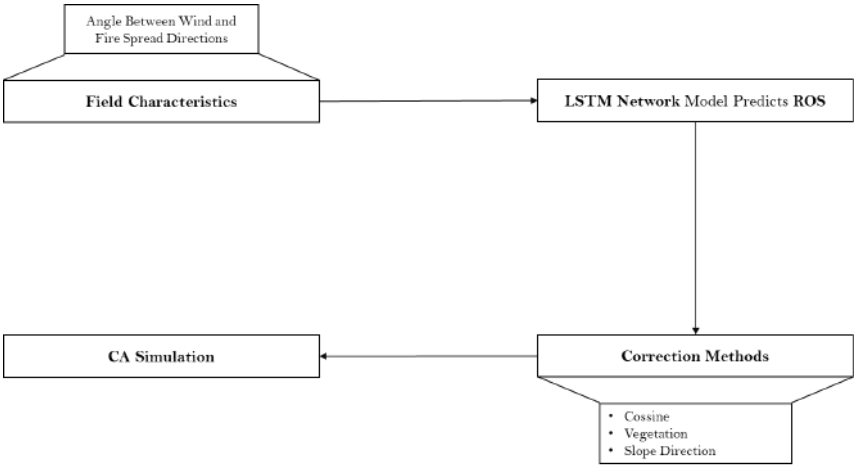

Figure 3.1: LSTM-CA Framework Structure. Adapted from Li et al., 2022.

where V_c denotes the prediction from the S-LSTM model, after cosine correction. K_{evc} represents the vegetation influence factor, calculated using external vegetation data, while K_{slope} represents the influence factor related to slope direction. Figure 3.2 provides an illustrative example of fire spreading behaviors.

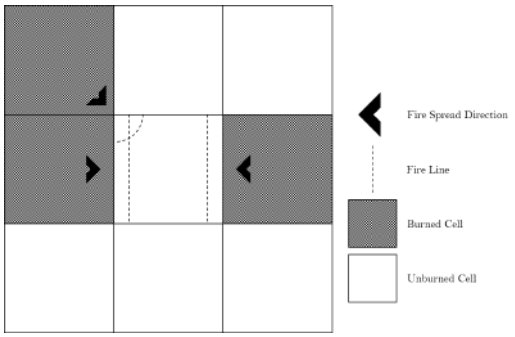

Figure 3.2: LSTM-CA General Spreading Behaviour. Adapted from Li et al., 2022.

This approach was initially validated by analyzing the mean squared error (Mean Squared Error (MSE)) of the S-LSTM model on 15 test sets. The results were highly encouraging, as only one-third of the test cases had an MSE greater than one, with a maximum value of 2.73.

Furthermore, the complete LSTM-CA model was utilized to simulate three actual wildfire incidents. Although it showed a slightly higher propensity for commission error emergence, it also demonstrated superior accuracy and consistency compared to alternative approaches.

3.2.2 Centroid Extraction Method

A newly proposed method (X. Liu et al., 2018) was developed, leveraging the motion rate of a *burned area centroid* to model the spreading of fire in the form of a growing ellipse at a predetermined speed. This innovative approach utilizes geostationary satellite data,

employing a pre-existing algorithm (G. Xu and Zhong, 2017) to identify hotspots. The fire spread rate is defined as follows:

$$V_{t,t+1} = \frac{D_{t,t+1}}{T_r}$$

Here, $D_{t,t+1}$ represents the distance of centroid movement from time t to $t+1$, and T_r corresponds to the time resolution of the satellite.

It is important to note that this method is subject to the limitations imposed by the resolution of the satellite instruments. Nonetheless, the model's performance was evaluated by computing the wildfire spread behavior of an actual incident using Himawari-8 image data. The results were then compared with those obtained from the established CSIRO Grassland Fire Spread Model (CGFSM), demonstrating favorable performance with an R^2 value of 0.76 and an RMSE of 0.50 $m \cdot s^{-1}$.

3.2.3 Digital-Twin Framework and Interactive Simulator

The platform described in Hyeong-su et al., 2019 leverages a modeling framework grounded in digital-twin architecture and incorporates external sensing data. Its primary objective is to enhance prediction accuracy, improve overall performance, and reduce the complexity associated with wildfire simulation processes. This platform comprises three noteworthy modules, as depicted in Figure 3.3.

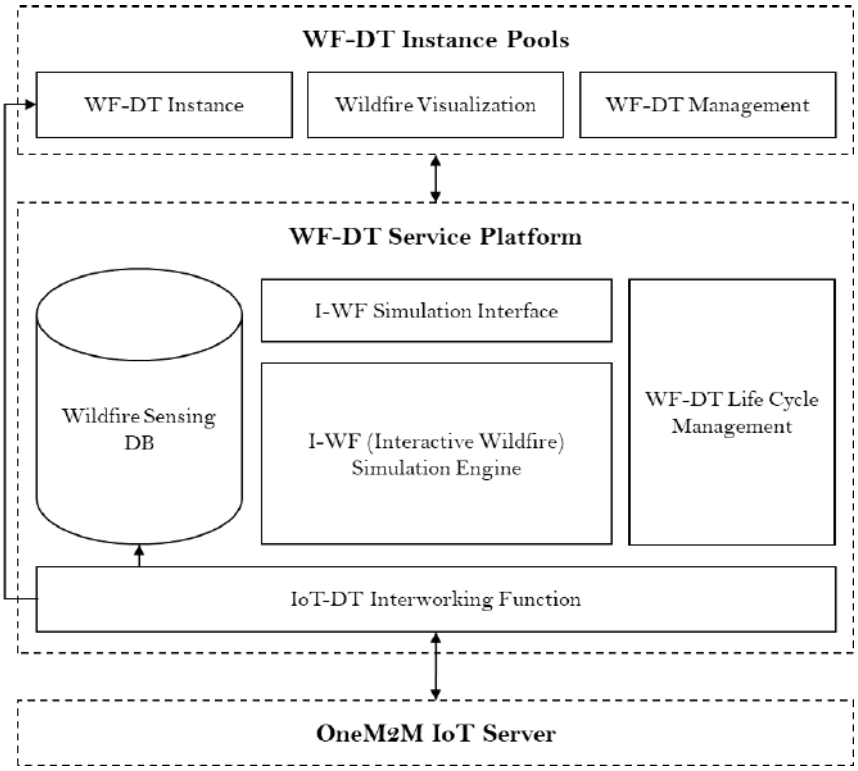

Figure 3.3: WF-DT/I-WF Platform Architecture. Adapted from Hyeong-su et al., 2019.

The Interactive Wildfire simulator integrated into the platform consists of three key components, as illustrated in Figure 3.4. This simulator employs data assimilation techniques to refine and improve the accuracy of its predictions by incorporating external sensing data.

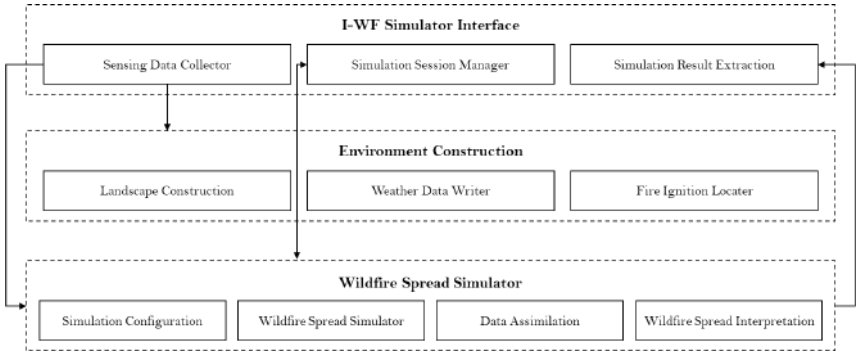

Figure 3.4: I-WF Architecture. Adapted from Hyeong-su et al., 2019.

3.2.4 OSG/FARSITE 3D Simulation Environment

The simulation environment described in Yun et al., 2011 utilizes the powerful graphical capabilities of OpenSceneGraph (OSG) to render the topographical space and visualize the 3D progression of a wildfire. Notably, this environment relies solely on particle systems for rendering purposes, while all wildfire simulation computations are performed using the Fire Area Simulator (FARSITE) Engine (Finney, 1998).

The environment itself comprises a wildfire simulation engine and visualization modules. Additionally, it features multi-layer terrain and vegetation renderers, leveraging digital DEMs and external satellite data. Moreover, it includes a scene management system and a panel for tracking damage statistics.

3.2.5 POTREE Web-GL Toolkit

POTREE (Schütz, 2016) is a renderer based on WebGL[1], designed specifically for the visualization of large point clouds. It possesses the capability to process billions of points in real time, making it a highly efficient tool. Notably, POTREE excels in representing LIDAR data, which is of particular relevance to the focus of this document. The toolkit's user-friendly interface is another noteworthy aspect, as it enables seamless collaboration by facilitating data set sharing without the need for extensive data transfers or dependence on external applications. This feature significantly contributes to efficient data analysis and validation processes. The toolkit achieves its performance through the integration of advanced techniques such as compounded dynamic resolution, region culling, and dynamic Levels of Detail (LOD) methods. These techniques ensure stable and reliable rendering of 3D spaces.

[1]JavaScript API based on the OpenGL ES standard that enables high-performance 2D and 3D graphics rendering directly within web browsers.

POTREE has been successfully applied in diverse areas of study, demonstrating its versatility. Examples of notable applications include its utilization in the analysis of human behavioral patterns (Carey et al., 2021), the generation of structure models (Kumar et al., 2019; Berto et al., 2021), and the assessment of post-disaster damages (Atasoy and Kocaman, 2021). These instances highlight the broad utility and practicality of POTREE across various domains.

3.2.6 Open-SfM Pipeline

Open-SfM (Adorjan, 2016) is an open-source software library developed for Structure-from-Motion (SfM) applications, complemented by support for Multi-View Stereo (MVS) technology, which facilitates the generation of detailed 3D reconstructions from large-scale point cloud datasets. The library offers a collaborative pipeline environment that promotes efficient data sharing and encompasses essential functionalities for uploading, editing, and analyzing SfM datasets. It also provides back-end processing capabilities and internal database storage.

A noteworthy aspect of Open-SfM is its front-end feature, which includes a point cloud renderer tailored for virtual tourism purposes. Moreover, the library allows for the integration of external applications and libraries, such as OpenDroneMap, thereby extending its functionalities and enhancing its utility.

Given its versatility, Open-SfM holds significant potential for diverse applications, ranging from general implementations (Amer et al., 2018) to highly specific use cases (Tsouros et al., 2020; Meza et al., 2019).

3.3 Established Frameworks for Wildfire Support

The culmination of wildfire behavior study and modeling undoubtedly resides on the application of that knowledge to protect and improve lives (Bolaño-Diaz et al., 2022; Ivanova et al., 2022) and to safeguard our infrastructure (Vaz et al., 2022). The frameworks described in this section were developed to aid civilians and authorities before, during and after these catastrophes. We explore particular solutions that range from established commercial applications to novel approaches still in early development. These solutions can be characterized with one or more of the following capabilities: prevention (before the incident), detection (detection of the incident; either smoke detection, fire/flame detection or mixed), management (resource and information availability during the incident), and/or post-management (damage assessment after the incident). Table 3.2 summarizes the solutions explored in this section, which are grouped by data collection approach, namely terrestrial (3.3.1), satellite (3.3.2), UAV (3.3.3), and mobile crowdsourcing (3.3.4).

Table 3.2: Analyzed frameworks.

Collection Type	Prevention	Detection	Management	Aftermath	Dev. Status	Reference
Ground Sensing	•	M	•	○	C	Stipaničev, 2010⊗
	•	M	○	○	PV	Guede-Fernández et al., 2021
	•	S	○	○	PV	Ko et al., 2012
Satellite Imagery	•	S	•	•	SV	McCarthy et al., 2020⊗
	•	S	•	•	UD	Casula et al., 2022⊗
	•	S	○	○	SV	S. Chen et al., 2022
Piloted UAV(s)	•	F	○	○	SV	Zhao et al., 2018
	•	S	•	○	SV	Karma et al., 2015
Autonomous UAV(s)	○	M	•	○	SV	Seraj and Gombolay, 2020
	○	-	•	○	PV	Aydin et al., 2019
	○	-	•	○	PV	Pham et al., 2017
	•	-	○	○	SV	Wardihani et al., 2018
Mobile Crowdsourcing	•	M	•	○	PV	Bogdos and Manolakos, 2019⊗

S: Smoke Detection
F: Fire/Flame Detection
M: Mixed Detection
-: N/A or No Information
UD: Under/Early Development
SV: Simulation Validation
PV: Practical Validation
C: Commercialized
⊗: Explored in Detail Further in this Document

3.3.1 Terrestrial Sensing

Ground-based sensor solutions are widely discussed in the literature and encompass a range of applications, from individual wildfire detection systems to comprehensive wildfire combat platforms.

In contemporary wildfire detection, terrestrial sensing approaches primarily employ image classification techniques utilizing advanced neural networks like CNNs, Fully Convolution Networks (FNCs), and Deep Neural Networks (DNNs). One recently proposed method for dual smoke and fire/flame detection utilizes a faster region-based CNN architecture, achieving a detection rate of 90% and a response time of 6.3 minutes (Guede-Fernández et al., 2021). However, alternative methodologies are also employed in certain studies, yielding promising results. For instance, a statistical model based on extended key-frame analysis demonstrates good performance in wildfire detection (Ko et al., 2012).

The iForestFire framework (Stipaničev, 2010; Stipaničev et al., 2012) is an interesting platform that utilizes advanced sensing methods for terrestrial vision-based wildfire monitoring and surveillance. It operates as a cloud computing system, focusing on early wildfire detection and later integrating a sophisticated confabulation-based detection

classifier. The framework comprises field units responsible for collecting and transmitting field data, as well as a main server. The general network structure and data flow, along with its constituent features, are illustrated in Fig. 3.5.

The detection system operates on a day-night cycle, specifically targeting smoke detection during the day and fire/flame detection during the night. Upon detecting a wildfire, an alarm is triggered, prompting a human operator to evaluate the corresponding image. The operator then exercises their judgment to validate or discard the alarm. To interact with the system, the end user can utilize a standard web browser interface, facilitating seamless accessibility and usability.

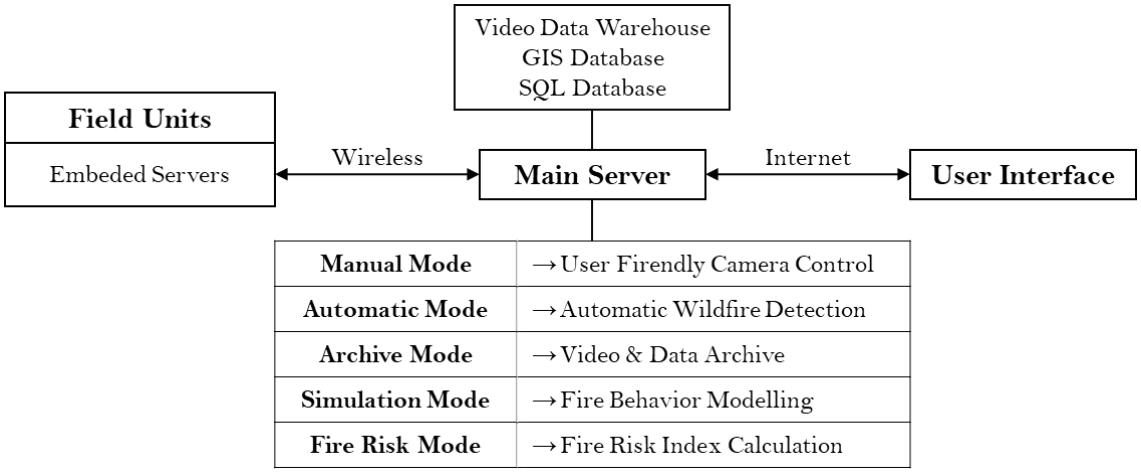

Figure 3.5: IForestFire Network Structure and Features. Adapted from *Vision Based Wildfire and Natural Risk Observers* (Stipaničev et al., 2012).

Although the iForestFire framework is a commercially available solution, its implementation has been primarily limited to its home country, specifically in several Croatian National and Nature Parks.

3.3.2 Satellite Imagery

Despite the limitations imposed by the spatial and temporal resolution of the available instruments, satellite imagery continues to offer numerous solutions. One such solution is the proposed U-Net CNN-based system (McCarthy et al., 2020), which provides near-real-time identification of fire pixels in geostationary satellite images by employing a statistical downscaling algorithm to enhance spatial resolution. The system utilizes a custom-designed U-Net CNN (Long et al., 2015) that is trained with active fire data from Low Earth Orbit (LEO) satellites and supported by external vegetation, terrain, and land use data from the Landscape Fire and Resource Management Planning Tools (LANDFIRE) Program. The system's structure is depicted in Figure 3.6.

To validate the system, simulation data from two wildfire incidents were employed, yielding modest results with critical success index values of 0.511 and 0.646.

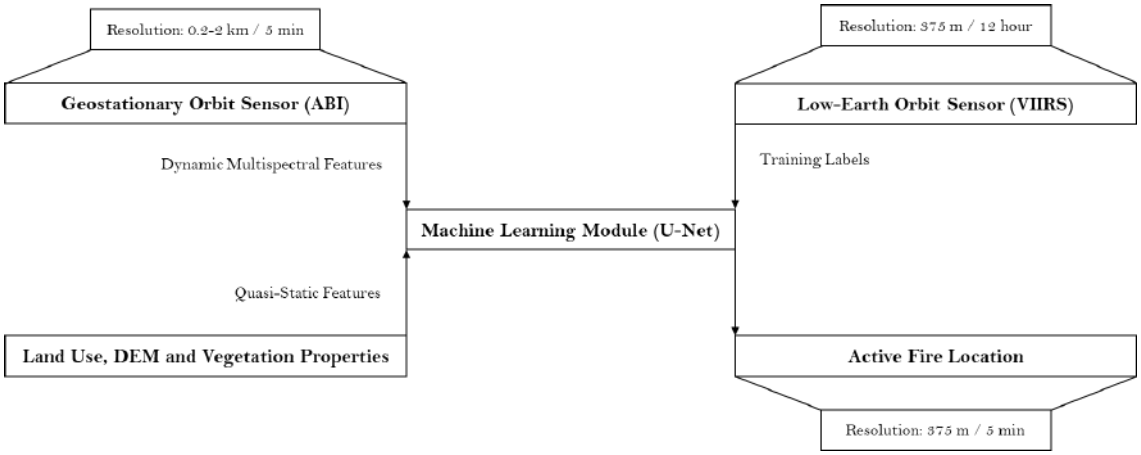

Figure 3.6: U-Net Based System Structure. Adapted from McCarthy et al., 2020.

Another notable project in early development is the S2IGI Project (Casula et al., 2022), which follows a similar approach for wildfire prevention and management. The project incorporates an imporved Satellite FIre DEtection (SFIDE) algorithm (Di Biase and Laneve, 2018) for fire detection. It aims to support three key phases: prevention, monitoring, and damage assessment. The project's offerings include weekly assessments of wildfire risk and damage, as well as real-time simulation capabilities for wildfire spread. These services rely on Earth Observation (EO) remote sensing and meteorological models and are complemented by a decision platform.

3.3.3 UAV-based Systems

UAVs, commonly known as drones, are aircraft that can be piloted remotely and/or autonomously. Their adaptability to various environments and relative affordability has generated significant interest in utilizing them for wildfire prevention, detection, and management. In terms of detection, UAVs have proven to be highly valuable. For instance, a study Cruz et al., 2016 proposed a novel index specifically designed for UAVs, which demonstrated remarkably high efficiency and an exceptionally precise coefficient (96.52%).

In recent years, several studies have aimed to provide a comprehensive overview of this approach (Nex and Remondino, 2019). Among all the reviewed solutions, there is a consistent factor: the data collection instrument. These vehicles are typically equipped with cameras capable of capturing real-time continuous images in one or multiple spectral bands, with the most common being visible (Jiao et al., 2019; Seraj and Gombolay, 2020), infrared (Aydin et al., 2019; Lin et al., 2019), and NIR (Martins et al., 2007).

While standalone UAV solutions do exist (Wardihani et al., 2018; Zhao et al., 2018), the majority are organized into networks of multiple UAVs with varying levels of autonomy and coordination (Ausonio et al., 2021; Karma et al., 2015; Seraj and Gombolay, 2020). These UAV networks process the data stream and often combine real-time data with additional wildfire datasets, as well as external geolocation and fire identification/modeling outputs.

Numerous approaches to fire identification within these frameworks rely solely on image segmentation, but the most relevant ones incorporate deep learning techniques. These frameworks frequently employ well-established CNN architectures, such as Fire_Net (Zhao et al., 2018), and regression-based algorithms like YOLO3 (Jiao et al., 2020; Redmon and Farhadi, 2018), to achieve their results.

It is worth noting that many of the implementations discussed in the literature are predominantly theoretical, relying heavily on simulated validation.

3.3.4 Mobile Crowdsourcing

Mobile crowdsourcing is a powerful technique that leverages the widespread use of mobile devices, such as smartphones and tablets, to gather data from a large number of individuals. In the context of wildfire management, mobile crowdsourcing emerges as a valuable tool for effectively collecting real-time information on crucial aspects such as the velocity and spread of wildfires, as well as the identification of affected areas.

While mobile crowdsourcing solutions are not yet extensively employed compared to other methods, there are notable instances where this approach has been successfully utilized. A recent exemplar is the CITISENS platform (Bogdos and Manolakos, 2019), which harnesses the collective effort of volunteer citizens as the sensing component, collecting and relaying the gathered data to the authorities. The platform encompasses two distinctive modes: reporting and decision-making, facilitated through mobile and PC applications, respectively. The entire system workflow is illustrated in Figure 3.7.

Once a registered citizen captures an active hotspot using their smartphone camera, the CITISENS application employs advanced computations to determine the precise location, elevation, and orientation of the device, enabling the computation of its view ray. By intersecting the device's view ray with the terrain topography derived from a DEM, the application extracts pertinent characteristics of the hotspot. All collected data is promptly shared with a central decision center, which aggregates the reports to generate or update a simulation of the wildfire's projected progression, utilizing the well-established FLogA tool (Bogdos and Manolakos, 2013). The hotspot information and simulation data are stored and conveniently accessible within an internal 3D mapping environment.

During field testing, the crowdsourced sensing aspect of the CITISENS application demonstrated remarkable accuracy, even without performing any calibration. In comparison to available satellite hotspot data products, the reported maximum expected offset for the CITISENS application, with no calibration, was approximately 150 meters, significantly outperforming other comparable solutions that offer an offset of 375 meters or more.

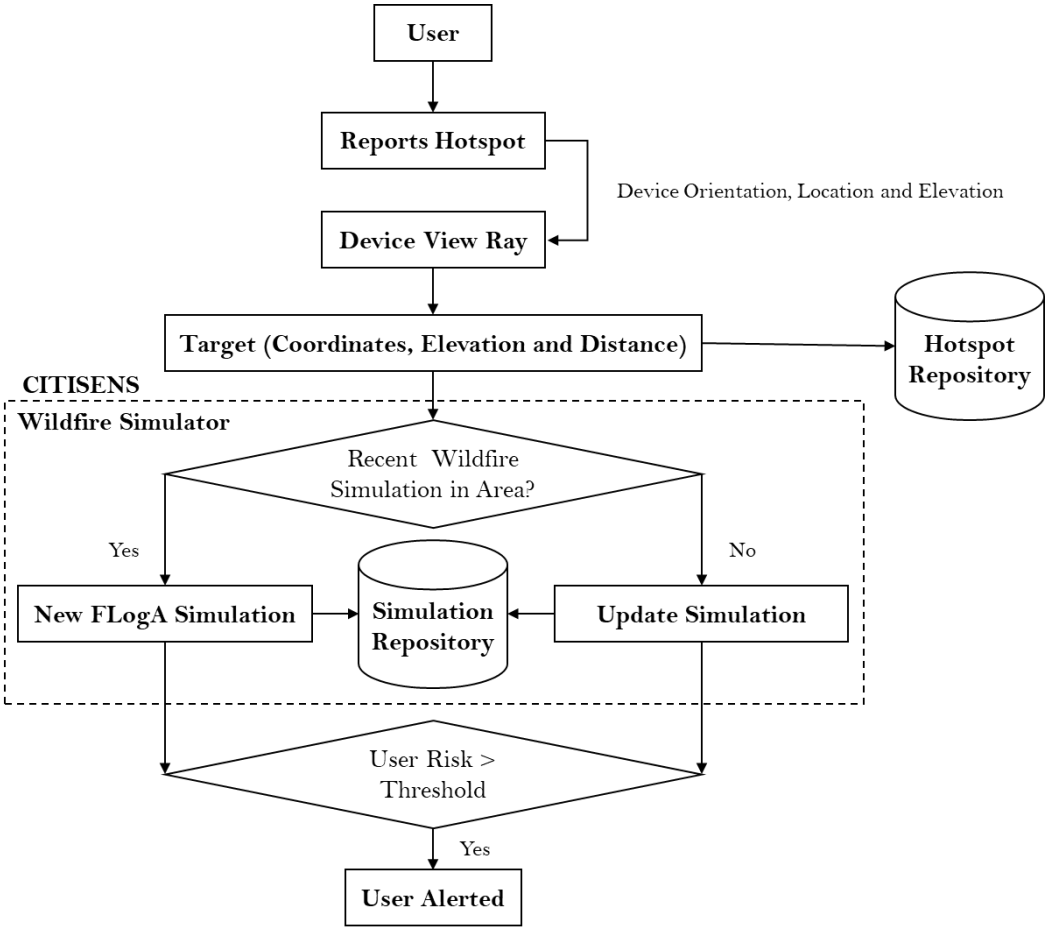

Figure 3.7: CITISENS System Structure. Adapted from Bogdos and Manolakos, 2019.

3.4 Discussion

While the development of wildfire support frameworks is not a new concept, the literature suggests that there are significant gaps in the development and successful implementation of such frameworks in some of the most severely affected regions worldwide.

Throughout this document, were identified the primary advantages and drawbacks of each type of framework. One prevalent challenge is the heavy reliance on continuous streams of external data, which is difficult to completely eliminate but can be mitigated to some extent. Additionally, the spatiotemporal resolution of data collection instruments is a critical factor that can greatly impact the system's performance if not taken into consideration and properly managed.

In this regard, the process of crowdsourcing data collection proves to be effective, offering the highest available spatiotemporal resolution. However, due to its reliance on crowdsourcing, the quality and quantity of data can never be guaranteed.

It is evident that while most of the mentioned frameworks share a common goal, their differentiation lies in their implementation. This presents an excellent opportunity for further development, especially when considering the utilization of UAVs as a robust

data collection method within a comprehensive support platform. Moreover, we strongly believe that the information gathered on vegetation identification, wildfire simulation, and visualization, as well as the frameworks themselves, can provide invaluable insights into the current state and progress of this field of study. These insights can then be leveraged to foster the development of innovative solutions.

4

Methodology

This chapter serves as a brief introduction to the general methodology employed in research and development planning. It encompasses key aspects such as the design of the platform's overarching structure (Section 4.1), the creation of a customized fuel model (Section 4.2), the selection and availability of experimental data sources (Section 4.3), and the formulation of validation strategies (Section 4.4).

4.1 Dual Module Structure

The platform has been programmed using Python and is structured around two distinct modules—NABU and PYTHIA. The NABU module specializes in generating all relevant data that the wildfire simulation module uses, including topographical and fuel maps, and weather variables. In turn, the PYTHIA module performs the necessary calculations to create a realistic simulation with the provided data and produces easy-to-read results. It was crucial to ensure that these modules were designed to operate entirely independently of each other, allowing for the seamless integration of external data sources. For instance, NABU generates a fuel map intended for use in PYTHIA; however, as long as the format specifications are met, any other external file can be effortlessly substituted in its place. A deeper dive into the intricacies of both the NABU and PYTHIA modules will be provided in Chapter 5. A simplified general structure pipeline of the dual module system is depicted in Figure 4.1.

4.2 Fuel Model Structuring

In order to achieve the most accurate fire behavior simulation possible its needed descriptions of the vegetation and other flammable materials that make up the fuel for a potential wildfire. In the first approach, these values were estimated with the use of data from the TRY Plant Database (Contributors, 2023). The final fuel model was derived from two primary sources: the surface fuel model descriptions provided by the National Wildfire Coordinating Group (NWCG) (NWCG, 2014), and the comprehensive fuel description

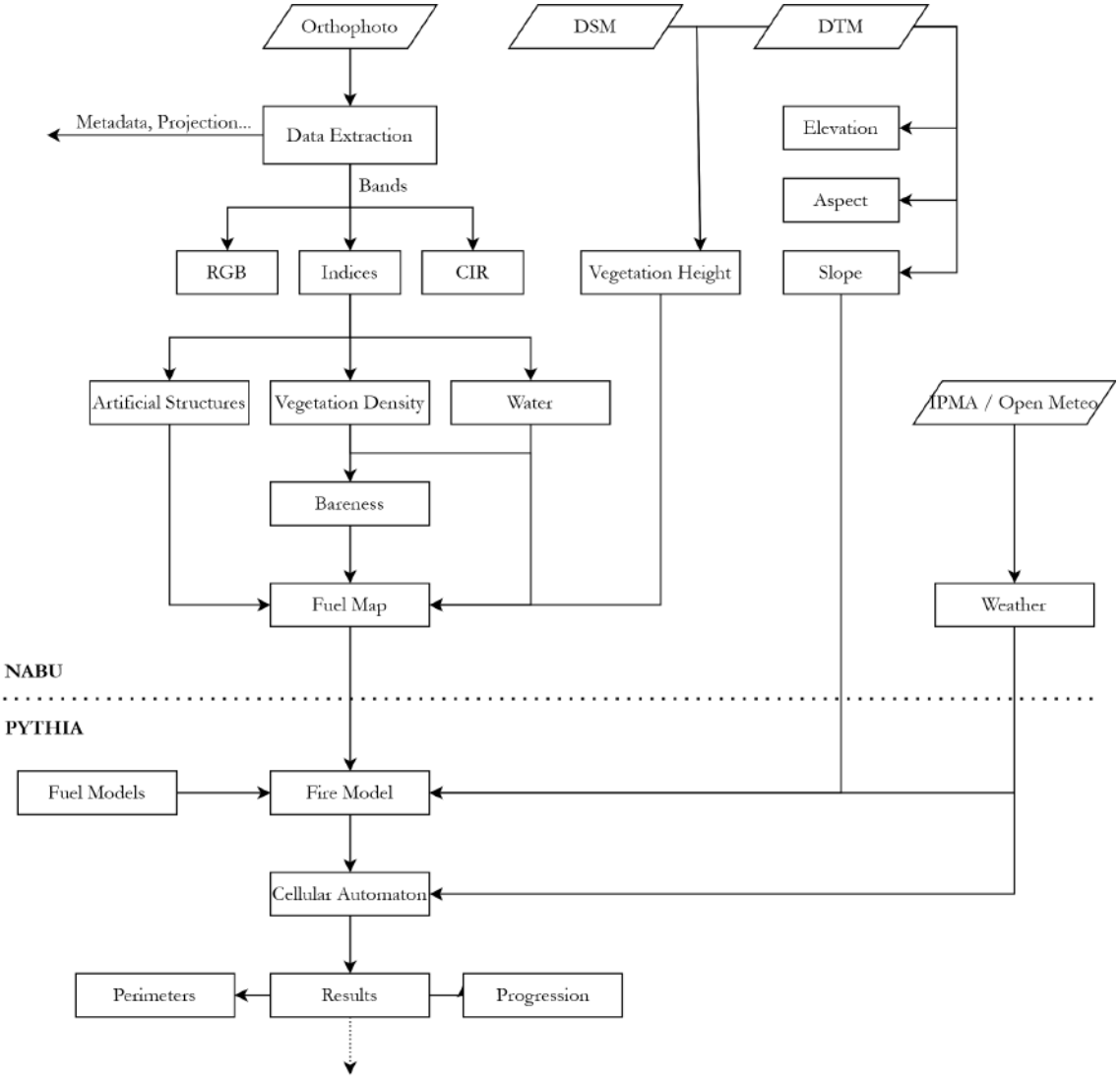

Figure 4.1: Simplified dual module pipeline.

centered around Portugal found in "Modelos de Combustível Florestal para Portugal" (Fernandes and Loureiro, 2022). This model is described in Table 4.1 and the values for its variables are available in Appendix E.

4.3 Experiment Data

Weather data was sourced from IPMA and Open Meteo, while remote sensing data was provided by Beyond Vision, a UAV manufacturer. Beyond Vision has made accessible a library of maps covering various regions throughout Portugal. The data was collected using two models of UAV—HEIFU Class 3 Hexacopter and BEHVT QuadPlane. These have been equipped with a Micasense Rededge-MX camera, which is a multi-spectral imaging system specifically designed for agricultural and environmental applications.

Table 4.1: Fuel model utilized. Adapted from Fernandes and Loureiro, 2022; NWCG, 2014.

Group	Model ID		Fuel Description
	Name	Number	
F	F-RAC	214	Very compact conifer duff.
	F-FOL	212	Compact deciduous duff.
	F-PIN	213	Medium to long pine duff.
	F-EUC	211	Eucalyptus duff.
M	M-CAD	221	Deciduous duff with shrubby undergrowth.
	M-ESC	222	Sclerophyll duff with shrubby undergrowth.
	M-PIN	227	Medium to long pine duff with shrubby undergrowth.
	M-EUC	223	Eucalyptus duff with shrubby undergrowth.
	M-EUCd	224	Discontinuous eucalyptus duff.
	M-H	226	Duff with herbaceous undergrowth.
	M-F	225	Duff with fern undergrowth.
V	V-MAb	234	Low bushes, rich in dead fuel.
	V-MAa	233	Tall bushes, rich in dead fuel.
	V-MMb	237	Low bushes, poor in dead fuel.
	V-MMa	236	Tall bushes, poor in dead fuel.
	V-MH	235	Low discontinuous green bushes and herbaceous plants.
	V-Hb	232	Low grass.
	V-Ha	231	Tall grass.
NB	NB-URB	91	Urban areas and structures.
	NB-WAT	98	Open water.
	NB-BARE	99	Soil devoid of sufficient fuel to support fire spread.

The camera produces five distinct spectral bands, encompassing red, blue, green, red-edge, and NIR. Detailed specifications of the aforementioned instrument are described in Table 4.2.

To accomplish the validation process, three maps have been selected, and henceforth, they will be referred to as Maps A, B, and C. Each of these maps uniquely represents different environments within continental Portugal, showcasing their distinctive characteristics. Map A depicts a semi-arid coastal area, Map B showcases a lush and densely vegetated, and Map C presents an extended stretch of highway enveloped by the surrounding rural scenery. For more detailed information regarding their precise locations, please refer to Table 4.3. Each of the chosen maps includes three distinct files: an orthophoto file, as well as Data Terrain Model (DTM) and Data Surface Model (DSM) files. An illustrative depiction of the study areas will be provided in Section 5.2.3, as shown in Figure 5.1.

4.4 FlamMap Validation

To validate the results of the PYTHIA simulation process, it was essential to establish a benchmark for comparison. For this purpose, FlamMap (Finney, n.d.) was selected. FlamMap is a software tool employed in wildfire management and research. Developed and maintained by the U.S. Department of Agriculture's Forest Service and various collaborators since 2003, and has a strong capacity to accurately model fire behavior and

Table 4.2: Micasense RedEdge-MX lens, imager, and band information. Adapted from MicaSense, 2020.

Lens and Imager Information		
Parameter	Value	
Pixel Size	3.75 μ m	
Resolution	1280 × 960 (1.2 MP × 5 Imagers)	
Aspect Ratio	4:3	
Sensor Size	4.8 mm × 3.6 mm	
Focal Length	5.4 mm	
Field of View	47.2° Horizontal, 35.4° Vertical	
Output Bit Depth	12-Bit	
GSD @ 120 m (400 ft)	8 cm/Pixel per Band	
GSD @ 60 m (200 ft)	4 cm/Pixel per Band	
Band Information		
Name	Center (nm)	Bandwidth (nm)
Blue	475	32
Green	560	27
Red	668	16
Red-Edge	717	12
Near Infrared	842	57

Table 4.3: Selected maps identification and positional information. All maps lie within continental Portugal.

Map	Location	Coordinates	Size (Km^2)
A	Tróia, Setúbal	38°25'34.1"N 8°49'27.0"W	0.55
B	Amadora, Lisbon	38°44'18.7"N 9°14'24.1"W	0.05
C	Sobral de Monte Agraço, Lisbon	39°02'32.1"N 9°10'56.5"W	1.78

related phenomena. This system incorporates engines such as the FARSITE (Finney, 1998) and FlamMap BASIC Finney, 2006, providing a rich suite for wildfire-related simulations.

5

Implementation

This chapter delves into an analysis of the implementation steps undertaken throughout the development of this solution, accompanied by the results it has yielded. It begins by exploring common mechanisms shared by both modules (Section 5.1), followed by a detailed examination of the NABU module (Section 5.2) and the PYTHIA module (Section 5.3).

5.1 Commonalities

Both modules share certain characteristics, including their overall folder structure (Section 5.1.1), initial argument processing (Section 5.1.2), and a brief description of the configuration mechanism (Section 5.1.3).

5.1.1 General Folder Structure

Both modules exhibit a similar outer folder structure, encompassing four items:

- `__data`: Folder responsible for housing all the raw files, predominantly consisting of `.tif` files, including any input files.
- `figures`: Folder responsible for containing all the figure outputs. Figures, in the context of the modules, refer to structured data plots that may include additional elements such as coordinate grids.
- `images`: Folder responsible for containing all the image outputs. These images are the basic outputs transformed into a visually comprehensible format, typically in PNG, without any additional enhancements.
- `__settings.yml__` File: Configuration file, responsible for managing the operation of the module.

These items would be contained within a folder named after a unique `id` associated with that map or simulation run.

5.1.2 Starting Arguments

Each modules has its own starting arguments, as described in Table 5.1.

Table 5.1: Modules starting arguments.

Argument	Command	Data	
		Type	Example
NABU			
Map ID	`-id`	`str`	'TROIA_2022'
Maps Folder Path	`-path`	`str`	'.../files/maps'
PYTHIA			
Simulation Run ID	`-id`	`str`	'TROIA_WINDLOW'
Simulations Folder Path	`-path`	`str`	'.../files/simulations'
Map Path	`-map`	`str`	'.../files/maps/TROIA_2022'
GPU Computation Trigger	`-gpu`	`Boolean`	—

5.1.3 Configuration File

Deep configuration for both modules is established through a YAML (.yml) file. However, since each module requires different inputs and triggers, the file structure is mostly distinct. Consequently, these configuration options will be discussed further for each individual module.

5.2 NABU Module

As mentioned previously, the NABU module focuses on transforming raw data into valuable information required for establishing a wildfire simulation—providing a total of 17 distinct outputs, as detailed in Table 5.2. This section is dedicated to examining the implementation of each of these outputs. An introduction to the module's configuration options are detailed in Section 5.2.1. Subsequently, the process of extracting band data and other pertinent file characteristics will be addressed, as outlined in Section 5.2.2. Following this, the utilization of the extracted data to generate image composites, including multispectral indices, will be explained in Section 5.2.3. The computation of terrain and fuel attributes will then be undertaken, as outlined in Sections 5.2.4 and 5.2.5, respectively. Lastly, the generation of weather variables will be handled in Section 5.2.6. Throughout this section, the results of the NABU module will be presented and analyzed. To examine these and additional results in greater detail, refer to Appendices A, B, and C.

5.2.1 Configuration Options

The configuration file for the NABU module consists of 29 components, as detailed in Table 5.3. The majority of these components are *switches*, and they play a crucial role in governing the module's operation and output.

Table 5.2: NABU module output elements.

Element	Channels	Data			Output Format(s)
		Type	Limits	Units	
Metadata	—	`key : value`	—	—	JSON
Transform	—	`[float]`	—	—	CSV
Projection	—	`str`	—	—	PRJ
Bounds	—	`[(float,float)]`	—	—	CSV
RGB	4[a]	`int`	[0,255]	—	TIFF, PNG
CIR	4[a]	`int`	[0,255]	—	TIFF, PNG
Index[b]	1	`float`	[-1,1]	—	TIFF, PNG
Elevation	1	`float`	[-∞,∞]	Meters[c]	TIFF, PNG
Slope	1	`float`	[0,90]	Degrees	TIFF, PNG
Aspect	1	`float`	[0,360]	Degrees	TIFF, PNG
Water	1	`int`	$0 \vee 1$	—	TIFF, PNG
Artificial Structures	1	`int`	$0 \vee 1$	—	TIFF, PNG
Coverage	1	`float`	[0,100]	Percentage	TIFF, PNG
Bareness	1	`float`	[0,inf]	Pixels[d]	TIFF, PNG
Canopy Height	1	`float`	[0,inf]	Meters	TIFF, PNG
Fuel	1	`int`	[0,255]	Fuel Model ID	TIFF, PNG
Weather	—	`float/int`	—	—	DSV

[a] Includes alpha channel.
[b] Available indices: SR, NDVI, DVI, RDVI, MSR, GNDVI, GARI, IDVI, NDRE, DVI2, GRVI, NDWI, ARI, MARI, EVI, EVI2, SAVI, MSAVI, OSAVI, TAVI, REI.
[c] Meters above sea level.
[d] Pixels to the nearest non-empty cell.

5.2.2 Initial Data Extraction

The raw orthophoto file contains five bands—red, green, blue, NIR and red-edge— with an additional alpha component. These bands are extracted through the utilization of the Geospatial Data Abstraction Library (GDAL) library (GDAL/OGR contributors, 2023), subsequently undergoing conversion into an 8-bit integer range. Note that the band data is never exported but is instead directly utilized by the system.

In addition to the band data, the orthophoto also offers important auxiliary information for geospatial calculations and plotting. These include the `metadata`, containing valuable geotagging[1] information, the `projection` which supplies information about the coordinate system used, and the geographic `transform` that provides the origin coordinates, pixel dimensions (width and height), and image rotation. Furthermore, a `spatial bounds` file defines a bounding box of coordinates around the region.

5.2.3 Composite Generation

In the context of this work, a *composite* image denotes the outcome of merging distinct color components. For instance, RGB represents a composite image created by combining the Red, Green, and Blue color components, while NDVI is formed through the fusion of

[1] Process of adding geographical information, such as latitude and longitude coordinates, to digital media.

Table 5.3: NABU configuration options.

Key		Value	
Group	Inner	Type	Description
`exports`	`figures`	Boolean	Export Switch
	`images`	Boolean	Export Switch
`nabu`	`metadata`	Boolean	Operation Switch
	`geo-transform`	Boolean	Operation Switch
	`projection`	Boolean	Operation Switch
	`bounds`	Boolean	Operation Switch
	`rgb`	Boolean	Operation Switch
	`cir`	Boolean	Operation Switch
	`indices`	str[]	List of Indices
	`elevation`	Boolean	Operation Switch
	`slope`	Boolean	Operation Switch
	`aspect`	Boolean	Operation Switch
	`water`	[str,float[2]]	Index and Threshold
	`artificial`	[str,float[2]]	Index and Threshold
	`bareness`	Boolean	Operation Switch
	`height`	Boolean	Operation Switch
	`sav`	Boolean	Operation Switch
	`coverage`	[str,float[2]]	Index and Threshold
	`fuel`	int[3]	Fuel Model IDs for F, M and V Groups.
	`weather`	Boolean	Operation Switch
`scale`	—	int	Pixel Width and Height (Meters)

the Red and NIR components. In this section, when a color component is mentioned, it can be inferred that the channel data used is the resulting raw extraction data described in Section 5.2.2. This section will focus on three types of composites–RGB, CIR, and multispectral indices.

The RGB composite is created by stacking the red, blue, and green bands in that order, and subsequently applying a gamma correction based on the power law transformation $I^{\frac{1}{G}}$, where I represents the input image and G the gamma value. The CIR composite, in turn, simply consists of the NIR, red, and green bands joined together. The resulting outputs are displayed in Figure 5.1.

To assemble the indices, the band data is applied as reflectance values per the index formula. Subsequently, to mitigate instrument errors and prevent overblown values, some outlier detection methods were tried, including Z-Score and Interquartile Range (IQR). Ultimately, it was determined that the most effective approach for this application was constraining the data within the range of $\bar{x} \pm 3 \times \sigma$, where $\bar{x}$ and σ represent the mean and the standard deviation of the data, respectively. The data finally normalized to a range of [-1, 1] using the formula $\frac{(X - X_{min}) * (b-a)}{(X_{max} - X_{min})} + a$, with $a = -1$ and $b = 1$, and where X, X_{min} and X_{max} represent the data, its minimum and maximum, respectively. Figure 5.2 illustrates the most relevant indices to be used further.

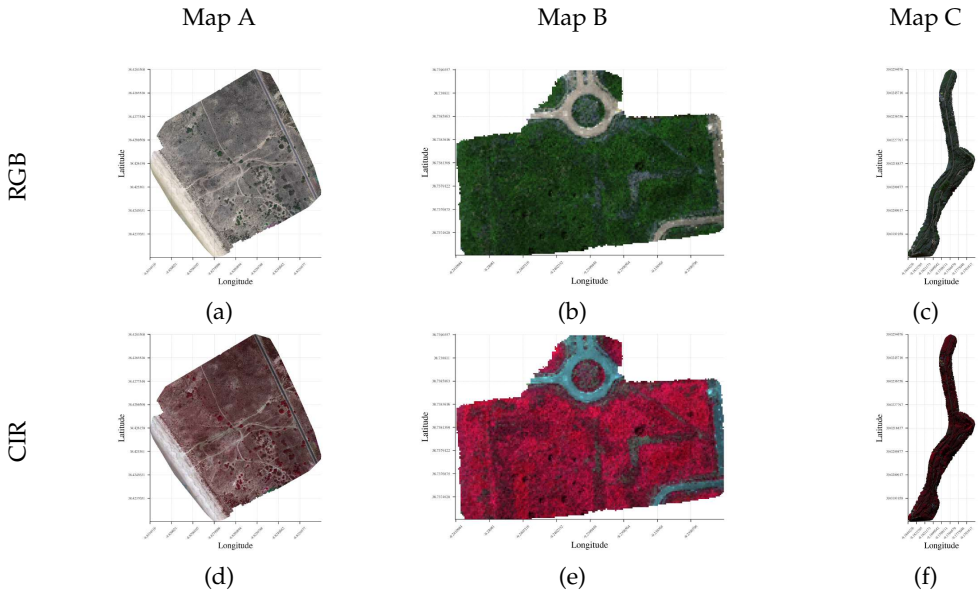

Figure 5.1: RGB and CIR composite maps generated by the NABU module, computed with a scale of 1 pixel per square meter.

5.2.4 Terrain Attributes

Terrain attributes encompass all physical characteristics of the landscape that are not related to vegetation. These encompass topographical features such as elevation, slope, and aspect, as well as other terrain elements, including water features and artificial structures like roads.

Elevation, slope, and aspect values are derived directly from the DTM (`dtm.tif`). The elevation data directly reproduces the DTM with adjustments made to rectify instrument-related errors. Meanwhile, the slope and aspect maps are generated from their definition in "Hill Shading and the Reflectance Map" (Horn, 1981), using the `richdem` R. Barnes, 2016 library. The results of these computations are illustrated in Figure 5.3.

In order to generate the water and artificial structure maps, a threshold was applied to a selected index, effectively isolating the details deemed most relevant (Table 5.4). The indices and thresholds were chosen empirically through the careful study of the results from the composite index generation described in Section 5.2.3 and effort was made to establish a generalized approach that maximizes the effectiveness of both components. Green Atmospherically Resistant Vegetation Index (GARI) was found to successfully isolate the artificial structures of Maps A (Figure 5.4a) and B (Figure 5.4b), while Map C (Figure 5.4c) required a different solution. Regarding water detection, the NDWI detected the edge of the water near the coast in the lower left region of Map A (Figure 5.4d). Maps B and C did not contain any water features to be detected, so the process was not applied to these maps.

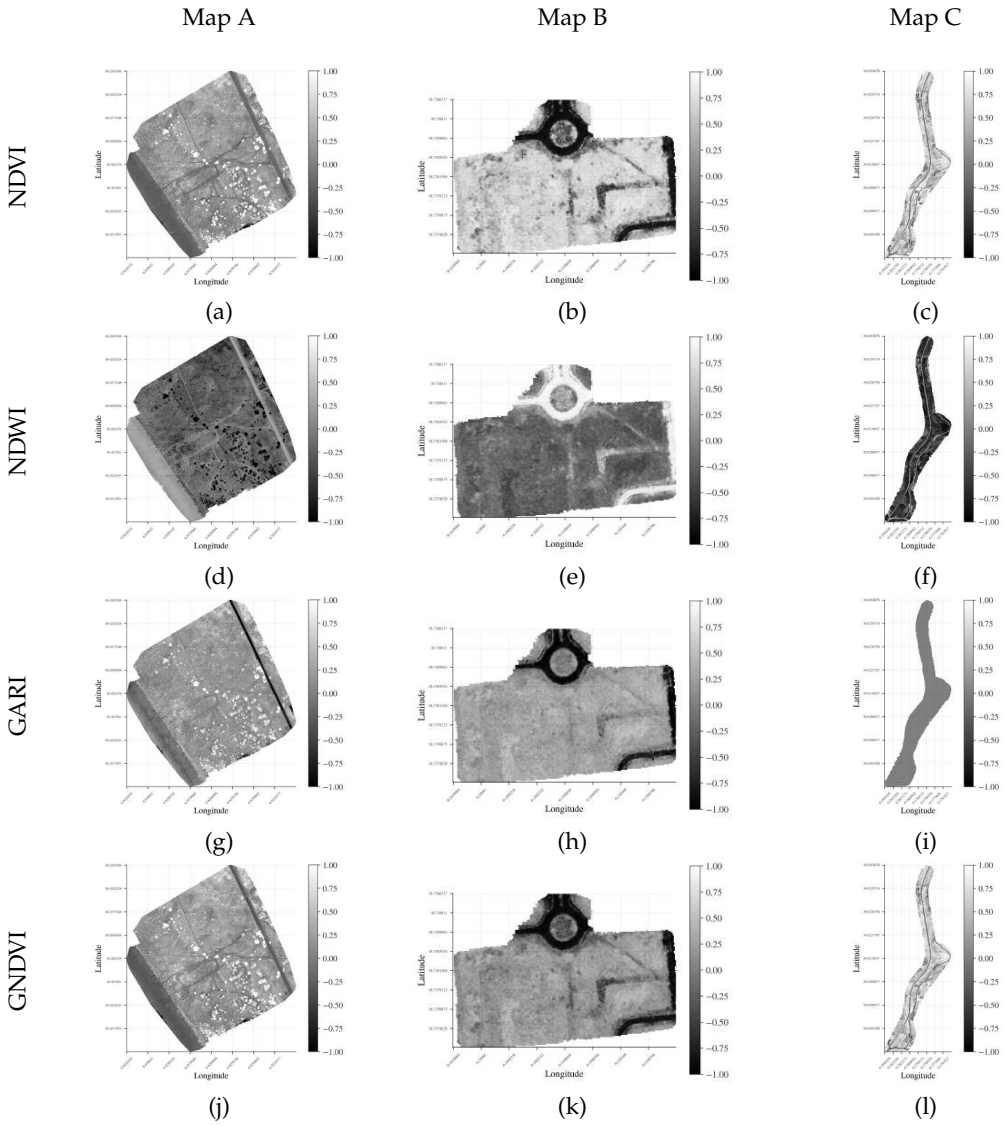

Figure 5.2: Relevant index maps generated by the NABU module, computed with a scale of 1 pixel per square meter.

Table 5.4: Water and artificial structure thresholding limits.

Map	Map A			Map B			Map C		
	Index	Low	High	Index	Low	High	Index	Low	High
Water	NDWI	0.5	0.9	—	—	—	—	—	—
Artificial Structures	GARI	-1	-0.5	GARI	-1	-0.5	GNDVI	-1	0

5.2.5 Fuel Attributes

Fuel attributes encompass the defining characteristics of vegetation within a given region. These include factors such as vegetation density, canopy height, and fuel map itself, which are of great importance in the context of wildfire simulation.

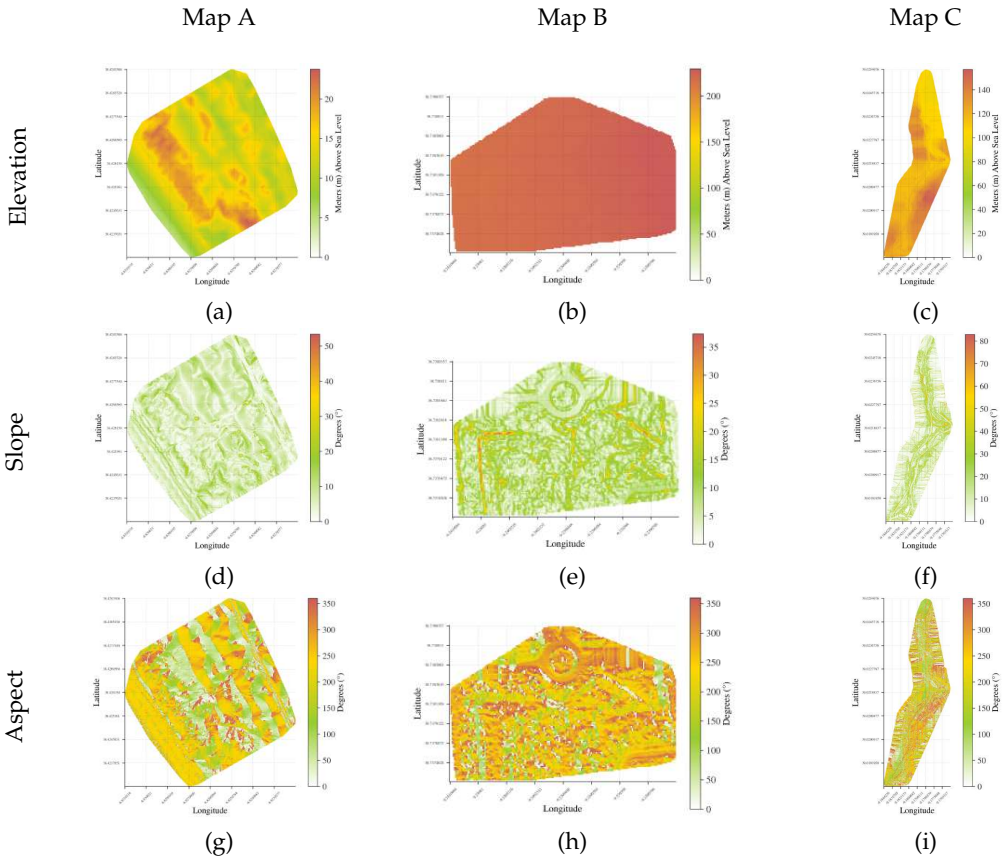

Figure 5.3: Topographical maps generated by the NABU module, computed with a scale of 1 pixel per square meter.

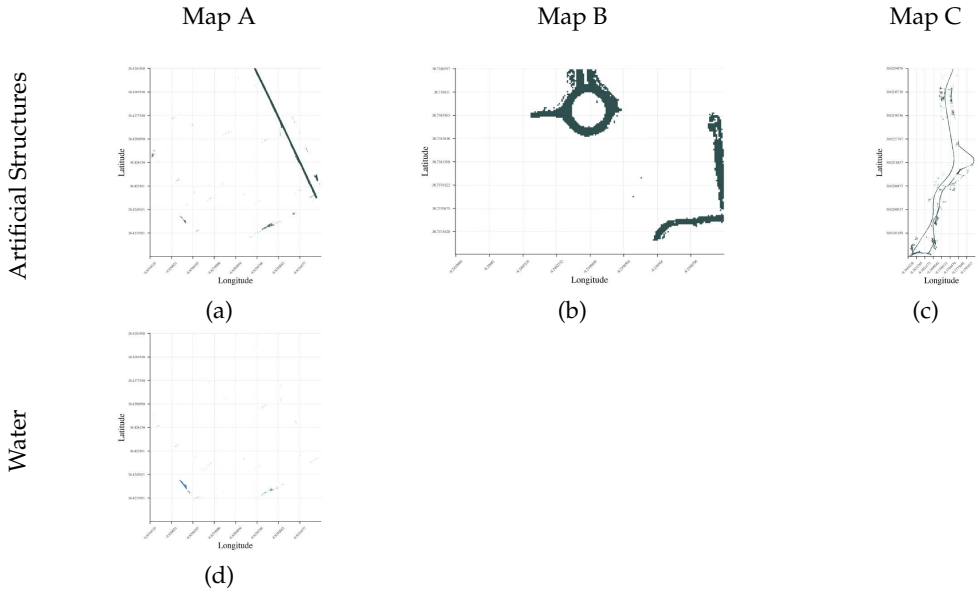

Figure 5.4: Water and artificial structure maps generated by the NABU module, computed with a scale of 1 pixel per square meter.

Creation of the coverage map follows a process similar to that employed for creating the water and artificial structure maps, as discussed in Section 5.2.4. This process involves the application of a threshold to a pre-selected multispectral index to extract the relevant data. In this particular case, the chosen index and threshold remain consistent across all text maps. The NDVI was utilized with a threshold range of [0.1, 0.9] to filter out extreme values before scaling the output to a range of [0, 100].

The bareness map is intricately linked to the coverage map, essentially representing its inverse in some capacity. To achieve this, start with the binarization of the coverage map. Subsequently, a distance transform is applied, yielding an image where each pixel value represents the distance between that pixel and the nearest non-zero (vegetated) pixel.

Canopy height can be determined by employing both the DTM and the DSM inputs. The measurement of bare earth's topography is represented by the DTM, while the DSM includes vegetation, buildings, or other above-ground features. The height of the vegetation is obtained by subtracting the DTM from the DSM. Further steps will be taken in the fuel map construction process to mitigate the error-inducing contribution of man-made structures.

Examples of the three previously discussed outputs can be observed in Figure 5.5.

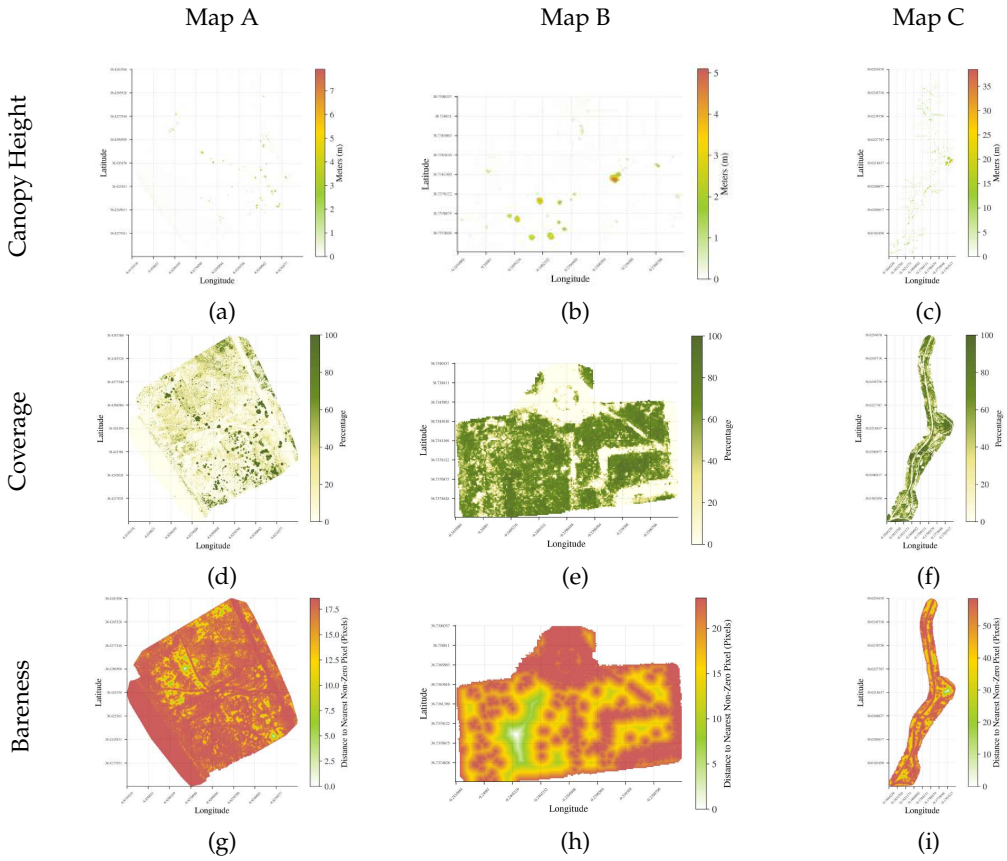

Figure 5.5: Coverage, bareness, and canopy height maps generated by the NABU module, computed with a scale of 1 pixel per square meter.

The process of fuel map modeling involves a set of sequential steps. Initially, an estimation of the undergrowth coverage density is calculated using data from the coverage and canopy height maps. This calculation helps us understand the prevalence of density beneath the tree line. It is assumed that this density value extends below the tree lines. If the value is sufficiently large, it is indicative of the presence of a fuel model from fuel group M, representing trees with a shrubby undergrowth. Conversely, if the density is lower, a fuel model from fuel group F, which represents trees with no undergrowth, is assigned to the areas where trees would typically grow. Subsequently, by utilizing the bareness map, the areas where bareness exceeds 95% of its maximum value are determined and filled with the appropriate model—NB-BARE. The remaining areas are filled with the model from fuel group V. Additionally, the bareness data is used to establish a transition zone between the bare and vegetated areas, which is set to fuel 224. Finally, data from the water and artificial feature maps are incorporated into the model. This comprehensive approach yields reasonably accurate results, considering the available data sources (visual representations of the fuel map can be seen in Figure 5.6). Note that the three fuel models representing the three fuel groups are chosen by the user from the available fuel model components described in Section 4.2.

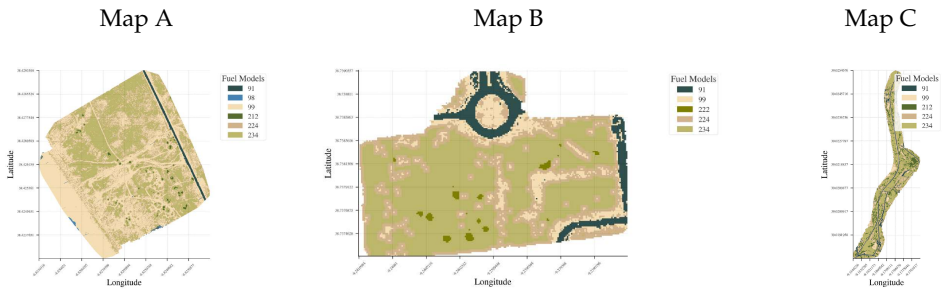

(a) (b) (c)

Figure 5.6: Fuel map generated by the NABU module, computed with a scale of 1 pixel per square meter.

5.2.6 Meteorological Variables

Meteorological data is retrieved through a choice of two distinct APIs: the IPMA API do Mar e da Atmosfera, 2023, maintained by Portuguese sources, and the Open Meteo API Team, 2023. While the IPMA API originates from and is managed by Portuguese authorities, the Open Meteo API offers a more comprehensive range of available data.

The generated text file adheres to the following format: Year, Month, Day, Time (in a 24-hour format from 0000 to 2359), Temperature (in Celsius), Relative Humidity (ranging from 0 to 99 as a percentage), Hourly Precipitation, Wind Speed (in Km/h), Wind Direction (measured from 0 to 360 degrees, clockwise from the north), and Cloud Cover (ranging from 0 to 99 as a percentage).

This component of the NABU module has the capability to aggregate a forecast file for up to 7 days into the future or to compile historical weather data between two specified dates.

5.3 PYTHIA Module

The PYTHIA module is responsible for building and realizing the wildfire simulation based on the maps produced by the NABU module. It generates 11 distinct outputs, which are outlined in Table 5.5. In the following sections, this document will delve into the underlying mechanisms responsible for producing these outputs, namely, the options for configuration of the module (Section 5.3.1),the fire model to be discussed in Section 5.3.2 and the cellular automaton propagation structure elaborated upon in Section 5.3.3. Subsequently, a brief description of the module's output types are described and illustrated (Section 5.3.4). Finally, the PYTHIA output results are explored and validated in a comparison to the established software FlamMap (Section 5.3.5).

Table 5.5: PYTHIA module output elements.

Element	Channels	Data			Output Format(s)
		Type	Limits	Units	
Fire Model					
Burning Index	1	`int`	[0,+∞]	—	TIFF, PNG
Energy Release Component	1	`int`	[0,+∞]	—	TIFF, PNG
Spread Component	1	`int`	[0,+∞]	—	TIFF, PNG
Fireline Intensity	1	`float`	[0,+∞]	Btu/ft/sec	TIFF, PNG
Flame Lenght	1	`float`	[0,+∞]	ft	TIFF, PNG
Heat per Unit Area	1	`float`	[0,+∞]	Btu/ft^2	TIFF, PNG
Rate of Spread	1	`float`	[0,+∞]	m/min*	TIFF, PNG
Residence Time	1	`float`	[0,+∞]	min	TIFF, PNG
Simulator					
Wind Direction Field	—	—	—	Km/H	TIFF, PNG
Perimeters**	1	`int`	[0,+∞]	Hours	TIFF, PNG
Progression**	1	`int`	[0,+∞]	Hours	TIFF, PNG

Note: Outputs available for each step of the simulation.
* Converted to metric system for cellular automaton operation.
** Output also available as a final agglomerated result.

5.3.1 Configuration Options

The configuration file for the PYTHIA module consists of 29 components, as detailed in Table 5.6. The majority of these components are *switches*, and they play a crucial role in governing the module's operation and output.

Table 5.6: PYTHIA configuration options.

Key		Value	
Group	Inner	Type	Description
`exports`	`figures`	Boolean	Export Switch
	`images`	Boolean	Export Switch
`pythia`	`run`	str	Type of Simulation
	`fire-model`	Boolean	Operation Switch
	`centroids`	Boolean	Operation Switch
	`perimeters`	Boolean	Operation Switch
	`polygons`	Boolean	Operation Switch
	`progression`	Boolean	Operation Switch
	`stats`	Boolean	Operation Switch
	`wind-vectors`	Boolean	Operation Switch
	`max-time`	int	Maximum Simulation Time (Hours)
	`min-time`	int	Minimum Simulation Time (Hours)
	`sat-threshold`	float	Saturaton Threshold
	`save-interval`	float	Simulation Save Interval (Minutes)
`scale`	—	int	Pixel Width and Height (Meters)

5.3.2 Fire Model

The fire model plays a crucial role in the proper functioning of the PYTHIA module. It provides essential components for simulating fire spread and offers additional variables from which additional conclusions can be directly extrapolated. The fire model implemented was based on the NFDRS 2016 model and it provides eight distinct results, three of which are of vital interest:

- **Rate of Spread**—quantifies the speed at which the flames or front edge of the fire move through combustible materials. The original fire model output is in ft/min, however, for convenience, this is later converted to m/min.
- **Spread Component**—the **Rate of Spread** rounded to the nearest integer, which will be necessary for the validation process.
- **Burning Index (BI)**—a numerical scale utilized for evaluating the risk of wildfires, taking into account various factors such as weather conditions and more. It provides a clear indication of the level of danger in a specific area and underscores the need for vigilance and particular care in that area.

A set of inputs is necessary to initialize the model—these are sourced from the module initial configuration file, the slope map (Section 5.2.4), the weather file (Section 5.2.6), the fuel model (Section 4.2) and the fuel map (Section 5.2.5). The elements of the fire model are computed through an extensive set of equations, which are described in Appendix D.

Table 5.7: Input parameters for the fire model, and sources. Adapted from Andrews, 2018.

Symbol	Parameter	Source
$(S_\sigma)_{ij}$	Total Mineral Content	Constant= 0.0555
$(S_e)_{ij}$	Effective Mineral Content	Constant= 0.01
$(\rho_p)_{ij}$	Particle Density (lb/ft^3)	Constant= 32 lb/ft^3
h_{ij}	Heat Content	Fuel Model and Fuel Map
σ_{ij}	SA/V Ratio (ft^2/ft^3)	
$(w_0)_{ij}$	Oven-Dry Fuel Load (tons/ac)	
δ	Fuel Bed Depth (ft)	
$(M_x)_1$	Dead Fuel Moisture of Extinction (%)	
$(M_f)_{ij}$	Fuel Moisture (%)	Constant
U_{20}	Wind Speed (mi/h)	Weather File
ϕ	Slope (º)	Slope Map File

$i = 1 \Rightarrow$ Dead fuel. $i = 2 \Rightarrow$ Live fuel.
$j = 1, 2, 3, 4 \Rightarrow$ 1H, 10H, 100H and 1000H values.

5.3.3 Cellular Automaton

Simulating the propagation of a wildfire entails creating an artificial space in which the fire can expand and spread. This concept was implemented through the development of a cellular automaton based on the implementation by Yassemi et al., 2008. This implementation offered a great starting point for the cellular automaton, albeit some changes were necessary to accommodate the system. The automaton functions around two main values, the ROS and the direction of travel (RAZ), the latter of which would align with the wind direction, as it is one of the most critical factors influencing wildfire expansion. Moreover, this model considers three cell states (Untouched, Burning, and Burnt), and its state is calculated in function of the percentage of the cell that is burnt.

The initial cellular automaton model utilized a Moore Neighborhood, consisting of 9 cells. While alternative neighborhoods were explored, the Moore Neighborhood persisted as the used configuration for most cases.

At any given moment, a wildfire spreads in two opposing directions: along the travel direction—Head Fire (HF)—and against it—Back Fire (BF). When there is a wind of level zero, both the HF and BF will behave similarly, resulting in the fire spreading uniformly from its point of origin. Moreover, the HF is associated with a ROS just as the BF is associated with a back ROS. It's worth noting that the fire model does not explicitly provide a back ROS, so this value was estimated to be one-tenth of the normal ROS.

This particular design features three distinct levels for accommodating different wind speeds. Level zero is tailored for wind speeds below 10 km/h, prioritizing speed while disregarding directional components. Levels one and two, on the other hand, are designed for wind speeds between 10 and 20 km/h and exceeding 20 km/h, respectively. These levels incorporate directional components based on the originating neighborhood cell. Detailed ranges for these angles are outlined in Table 5.8.

Table 5.8: Ranges of RAZ permitting fire to spread to the cell, for levels 1 and 2. Adapted from Yassemi et al., 2008.

Neighbour	Level 2				Level 1			
	Head		Back		Head		Back	
Northwest	108	161	288	341	90	180	270	360
North	135	225	315	45	90	270	270	90
Northeast	198	251	18	71	180	270	0	90
West	45	135	225	315	0	180	180	360
East	225	315	45	135	180	360	0	180
Southwest	18	71	198	251	0	90	180	270
South	315	45	135	225	270	90	90	270
Southeast	288	341	108	161	270	360	90	180

Level 2 $\Rightarrow$ Wind Speed $> 20Km/H$
Level 1 $\Rightarrow 10Km/H <=$ Wind Speed $<= 20Km/H$

The directional components vary depending on whether the wind is coming from one of the cardinal directions or not. When the wind is not originating from a cardinal

direction, the spread components diverge between the two adjacent cardinal directions in the direction of travel. For instance, if the wind is blowing from the northwest, the spread will encompass components in both the west and north directions. However, if the wind is blowing directly from the north, its sole component will be in the northward direction. One particular quirk with the model lies precisely in its interaction with wind conditions that fall within the range of the cardinal directions. Should a cell become isolated and the wind is, for instance, blowing from the north, the fire will exclusively spread downward, persisting in this direction until either the wind shifts or its speed falls below the threshold of level zero. This behavior leads to the emergence of certain anomalies in the simulation, manifested as extended streaks of pixels. Although these artifacts are relatively infrequent, they do manifest on occasion.

Finally, one important factor to consider is the scale used in this simulation, where 1 pixel corresponds to 1 square meter. When the ROS values, expressed in meters per minute, are sufficiently high, they can lead to neighborhood saturation. This presents two significant challenges:

Firstly, since each cell represents 1 square meter by default, any burnt area larger than 1 m^2—a rather small amount— will result in the excess area being discarded. This would significantly slow down the simulation compared to real-world fire propagation.

Secondly, in environments with low wind, if the fire components are large enough, every cell in the neighborhood will instantly catch fire at each step. This unnatural behavior results in the fire spreading in a perfect square shape.

To address these issues, a few adjustments have been made. In low-wind conditions, a Von Neumann neighborhood is now used instead of a Moore neighborhood. This change helps achieve a more natural circular fire propagation pattern. Additionally, a multiplication coefficient has been introduced to the final cell calculations. This coefficient accelerates the spread in zones where the fire would naturally be slower, compensating for some of the propagation loss described earlier.

5.3.4 Simulation Output Types

PYTHIA generates two distinct types of outputs: visual representations, including Perimeter, Progression, and Wind maps (discussed in Sections 5.3.4.1,5.3.4.1, and5.3.4.3), as well as data-centric outputs like the statistics file (Section 5.3.4.4).

5.3.4.1 Progression

Progression maps provide a snapshot of the current status of a fire's progress at a specific moment in time. These maps are available either for a specified time frame (Figure 5.7a) or as an aggregation of all progress states (Figure 5.7b). Additionally, this information can be accessed in the form of a polygon dictionary, with the timestamps serving as keys corresponding to the recorded states.

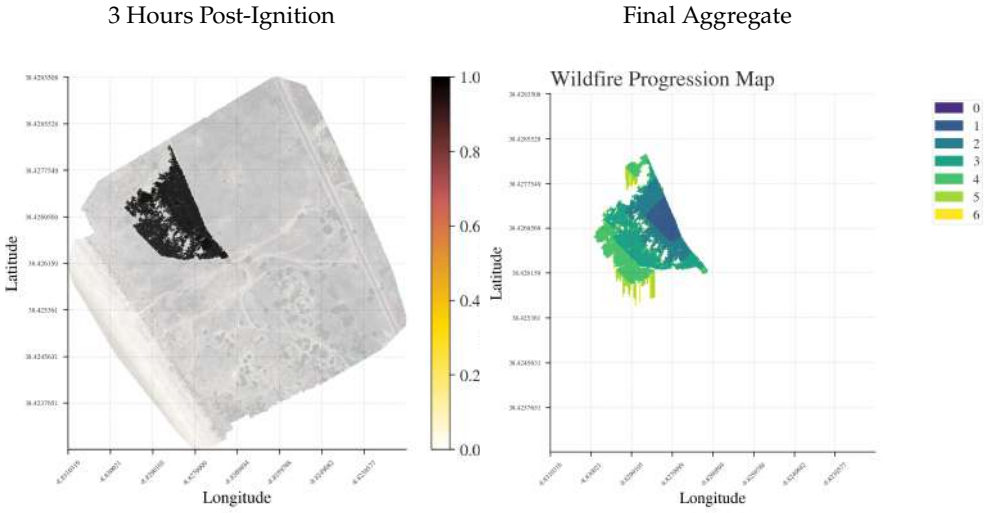

(a) (b)

Figure 5.7: Progression map examples, computed with a scale of 1 pixel per square meter. For the aggregated map, each color represents one hour of advancement.

5.3.4.2 Perimeters

Perimeter maps share similarities with progression maps, yet they exclusively display the boundaries of each state. This alternative visualization provides distinct advantages for certain fire shapes. Much like progression maps, perimeter maps are accessible for each time step (Figure 5.8a) and as an aggregated representation (Figure 5.8b).

5.3.4.3 Wind Vectors

Wind vector fields illustrate the prevailing wind direction at a specific time, offering valuable assistance in validating and visualizing weather conditions (Figure 5.9).

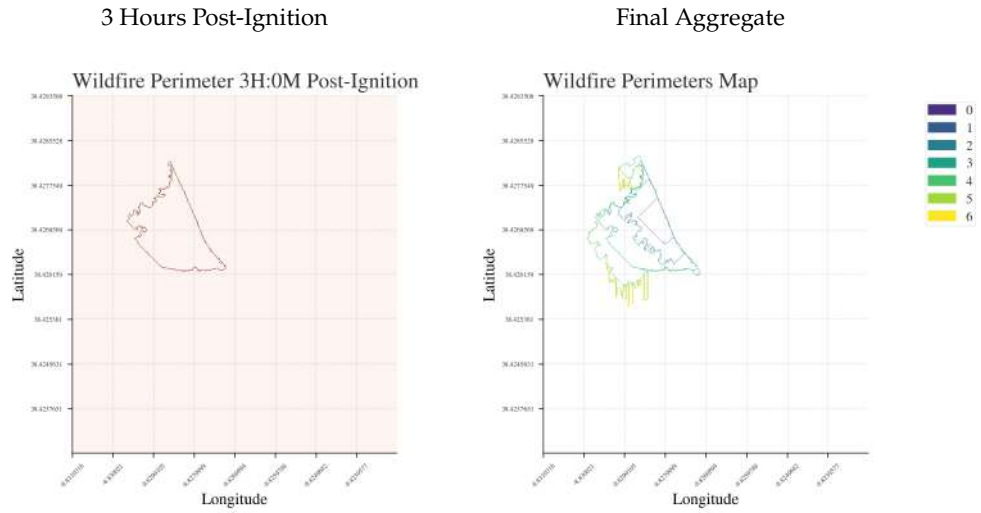

(a) (b)

Figure 5.8: Perimeter map examples, computed with a scale of 1 pixel per square meter. For the aggregated map, each color represents one hour of advancement.

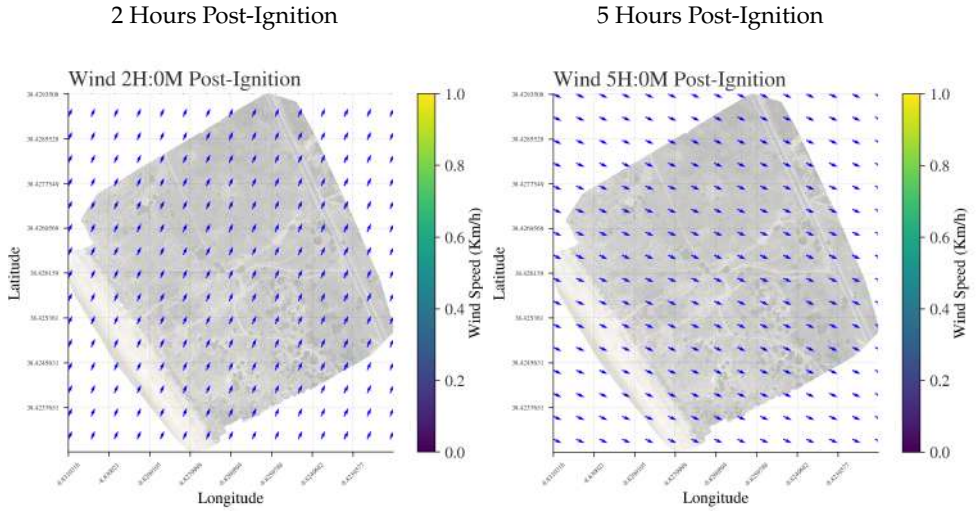

(a) (b)

Figure 5.9: Wind vector map examples, computed with a scale of 1 pixel per square meter.

5.3.4.4 Statistics

The statistics file provides a comprehensive record of pertinent information regarding the simulation, including details such as the time when the fire crossed its saturation threshold, the burnt area for each incremental step, and the cumulative total burnt area.

5.3.5 Results and Validation

Firstly, a brief exploration on the possible use of Burning Index (BI) as a danger indicator is presented (Section 5.3.5.1). Then, the remainder of this section aims to analyses the results generated by PYTHIA and compare them with those produced by FlamMap in order to establish a benchmark for assessing the accuracy of the developed module. To achieve this, several distinct weather and setting configurations were assembled to display the capabilities of the PYTHIA module (Section 5.3.5.2). Both systems are then employed in a plain constant map to evaluate the performance in the simplest possible environment (Section 5.3.5.3). Subsequently, their performance in a real-world scenario is assessed by employing Maps A and B as stage regions (Sections 5.3.5.4 and 5.3.5.5). Finally, a statistically approach to result evaluation is presented in Section 5.3.5.6.

5.3.5.1 Preliminary Danger Evaluation

The BI that the fire model provides can be utilized, as previously mentioned, as a danger indicator. Maps like the ones demonstrated in Figure 5.10 can be of significant value in assessing the susceptibility of a zone to wildfires and determining the appropriate level of care and intervention that authorities should deploy when addressing fires in those regions.

Not surprisingly, the highest BI values are observed in areas with dense patches of low to medium vegetation. Interestingly, despite containing a significant amount of fuel, trees tend to burn slowly, which explains the lower BI values associated with them. It's worth noting that the BI can change over time, and in this context, as wind strength intensifies, so does the BI, especially in proximity to low vegetation areas.

5.3.5.2 Test Configurations

As mentioned previously, to facilitate testing and validation of the module, the outputs from the regional maps A and B were complemented with an additional constant plane map based on the geographical location of map A, as described in Figure 5.9.

Table 5.9: Constant plane map specifications.

Element	Value	Unit
Elevation	0	Meters
Slope	0	Degrees
Aspect	0	Degrees
Fuel Model	222	—
Coverage	75	%

Furthermore, three distinct weather presets were designed:

- **WAT (Weather Angle Test)**: Steady wind flow, progressively shifting wind direction from 0º to 360º in 45º increments. Its purpose is to confirm the accuracy of wind

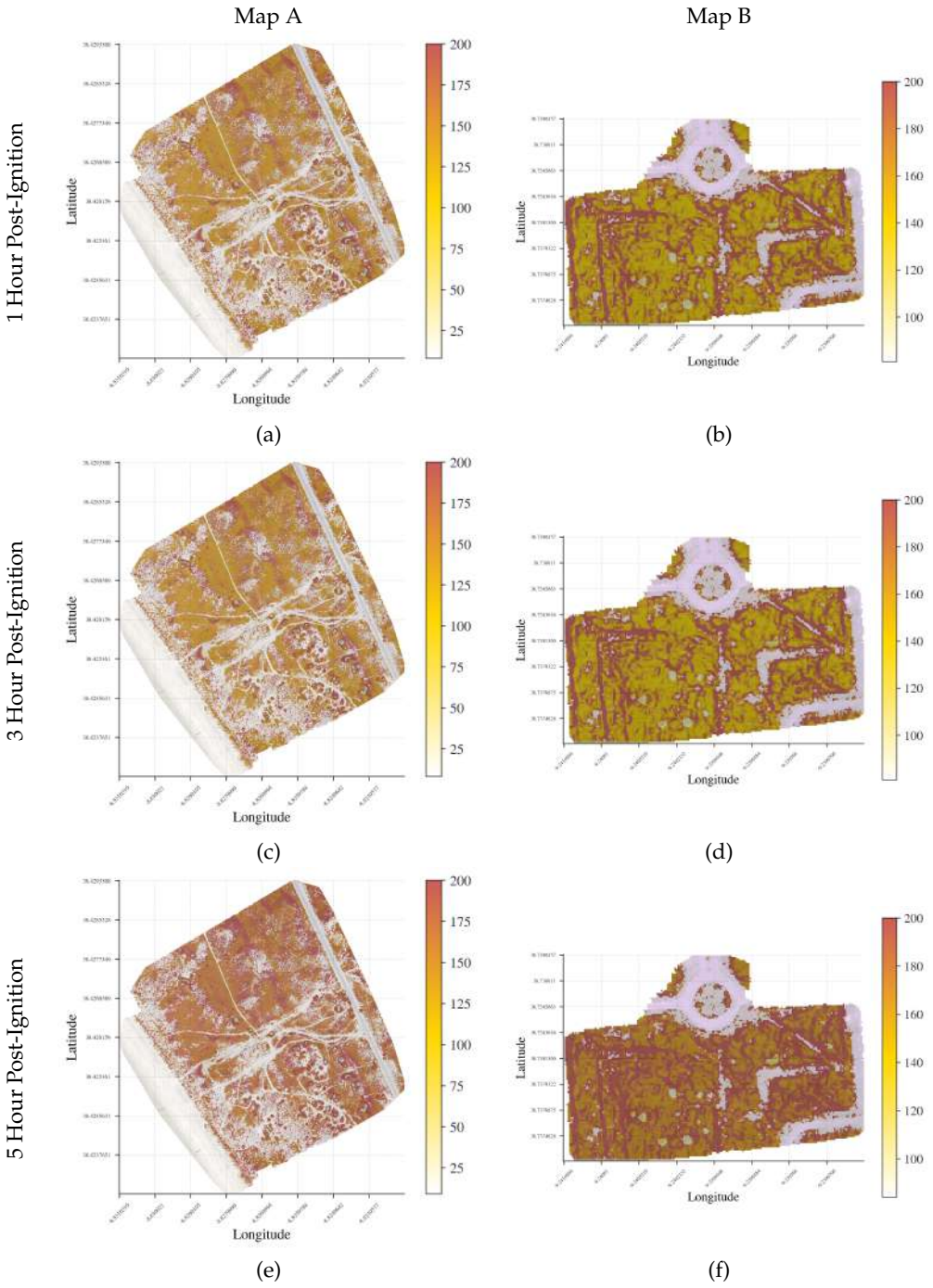

Figure 5.10: Burning Index (BI) results, computed with a scale of 1 pixel per square meter.

direction behavior.

- **W1 (Weather Preset #1)**: Consistently low wind speed with minimal fluctuations and a constant wind direction.
- **W2 (Weather Preset #2)**: Low to medium wind speed with some occasional spikes and a variable wind direction.

- **W2 (Weather Preset #3)**: Medium to high wind speed with some occasional spikes and a variable wind direction.

These presets were devised to assess behavior and performance across diverse scenarios, with detailed descriptions provided in Table 5.10. While the constant plain map utilizes the entire 12-hour dataset, the assessment of Map A and B focuses solely on the initial 6-hour window.

Table 5.10: Weather variables for the first 12 hours of WAT, W1, W2 and W3.

				WAT		W1		W2		W3		
T	TMP	RH	P	WS	WD	WS	WD	WS	WD	WS	WD	CC
0000	20	65	0.00	10	0	5	0	5	325	20	5	0
0100	20	65	0.00	10	45	5	0	5	155	20	55	0
0200	20	65	0.00	10	90	5	0	5	205	20	55	0
0300	20	65	0.00	10	135	5	0	15	345	20	245	0
0400	20	65	0.00	10	180	10	0	5	260	20	200	0
0500	20	65	0.00	10	225	15	0	5	295	20	40	0
0600	20	65	0.00	10	270	10	0	5	235	20	25	0
0700	20	65	0.00	10	315	5	0	10	285	20	90	0
0800	20	65	0.00	10	360	5	0	10	335	20	0	0
0900	20	65	0.00	10	0	5	0	15	350	20	0	0
1000	20	65	0.00	10	0	5	0	20	320	20	120	0
1100	20	65	0.00	10	0	10	0	25	300	20	140	0
1200	20	65	0.00	10	0	10	0	20	50	20	120	0

T ⇒ Time (0-2359), TMP ⇒ Temperature (ºC)
RH ⇒ Relative Humidity (%), P ⇒ Percipitation (mm)
WS ⇒ Wind Speed (Km/H), TMP ⇒ Wind Direction (º)
CC ⇒ Cloud Cover (º)

5.3.5.3 Assessment on Constant Plane Map

In the plane map, the initial objective was to evaluate the behavior of wind direction. Following a thorough analysis of the results, it is evident that the wind direction functions correctly, as illustrated in Figure 5.11—wind direction is indicated in a clockwise manner, such that 0º signifies wind originating from the north, while 90º indicates wind from the east.

Three additional simulations were conducted on this map, each simulating the progression of a fire over a period of twelve hours. The outcomes generated by the module exhibit resemblances to the outputs from FlamMap. It can be ascertained in Figure 5.12 that while a similarity of both the fire propagation direction and the overall burn shape is observable, this is most accentuated in for W1 and degrades with W2 and W3. This suggests that while the module performs satisfactory in providing estimates in a constant plane environment, higher wind speeds and variations in wind direction will lead to greater deviations from the expected results.

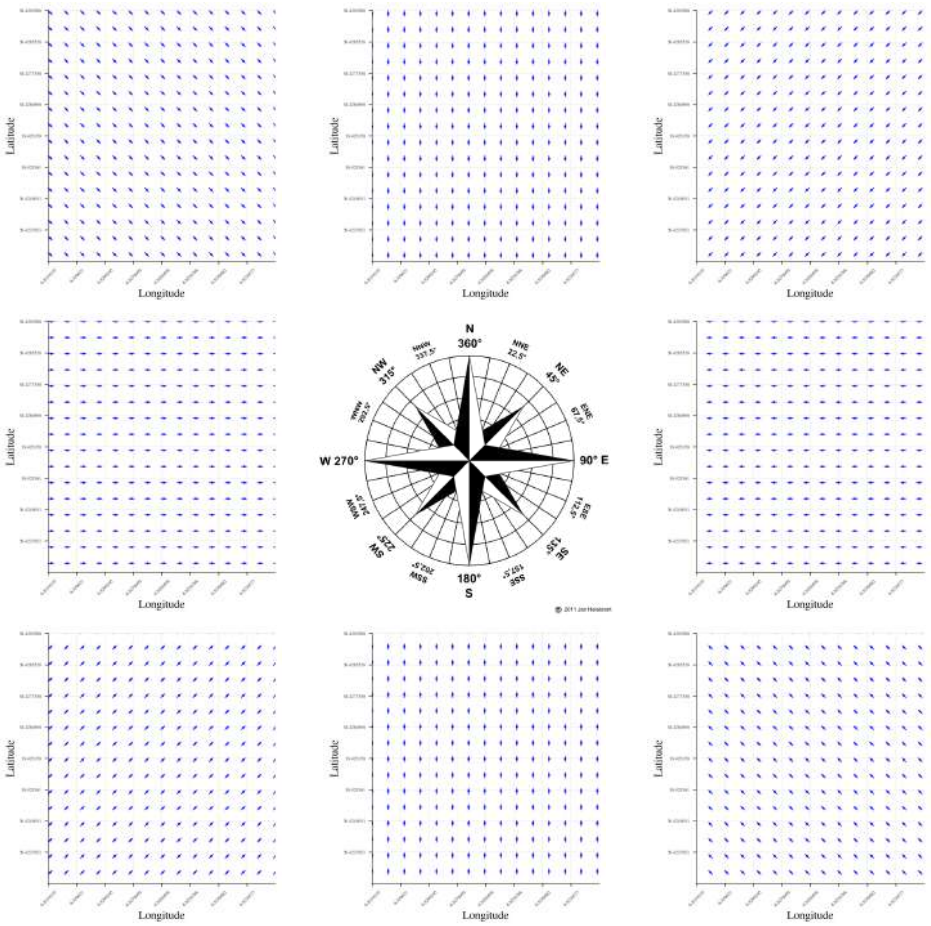

Figure 5.11: Wind direction behavior assessment. Clockwise from the North (0º).

5.3.5.4 Assessment on Map A

Fifteen distinct simulations were conducted in total on this map, each simulating the progression of a fire over a period of six hours.

The results obtained with Map A seem to align with our prior observations, as the directional patterns and overall shapes remain highly consistent, especially with W1 (Figure 5.13). With W2 and W3 (Figures 5.14 and 5.15), the results are more variable in nature, however their overall progression still correlates with the expected.

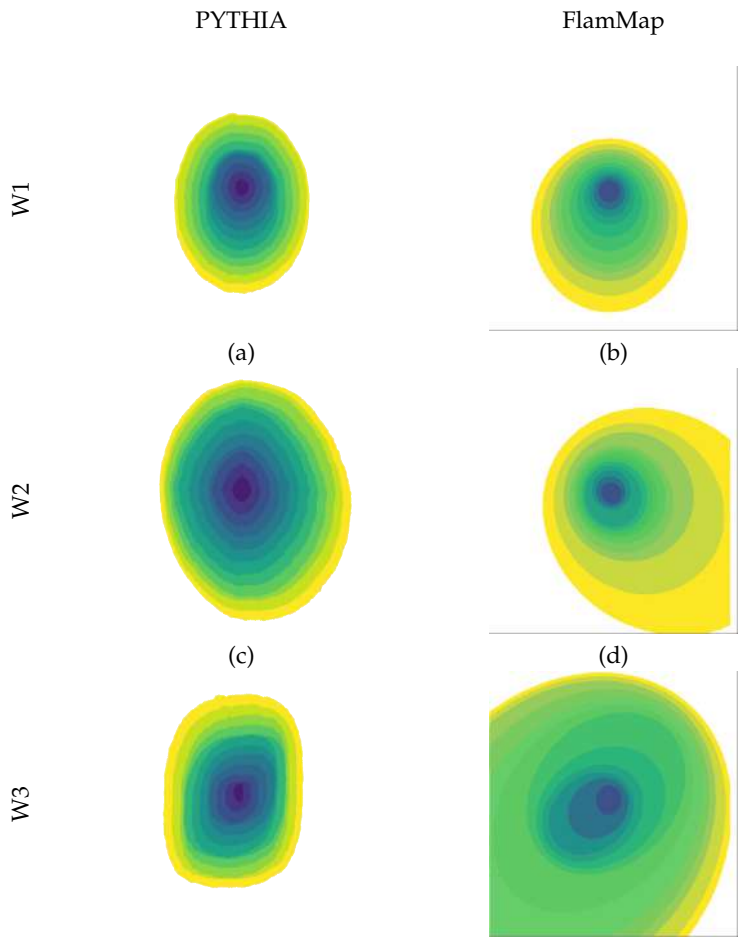

Figure 5.12: Constant plane fire progression map results with presets #1, #2 and #3, computed with a scale of 1 pixel per square meter. Each color represents one hour of advancement.

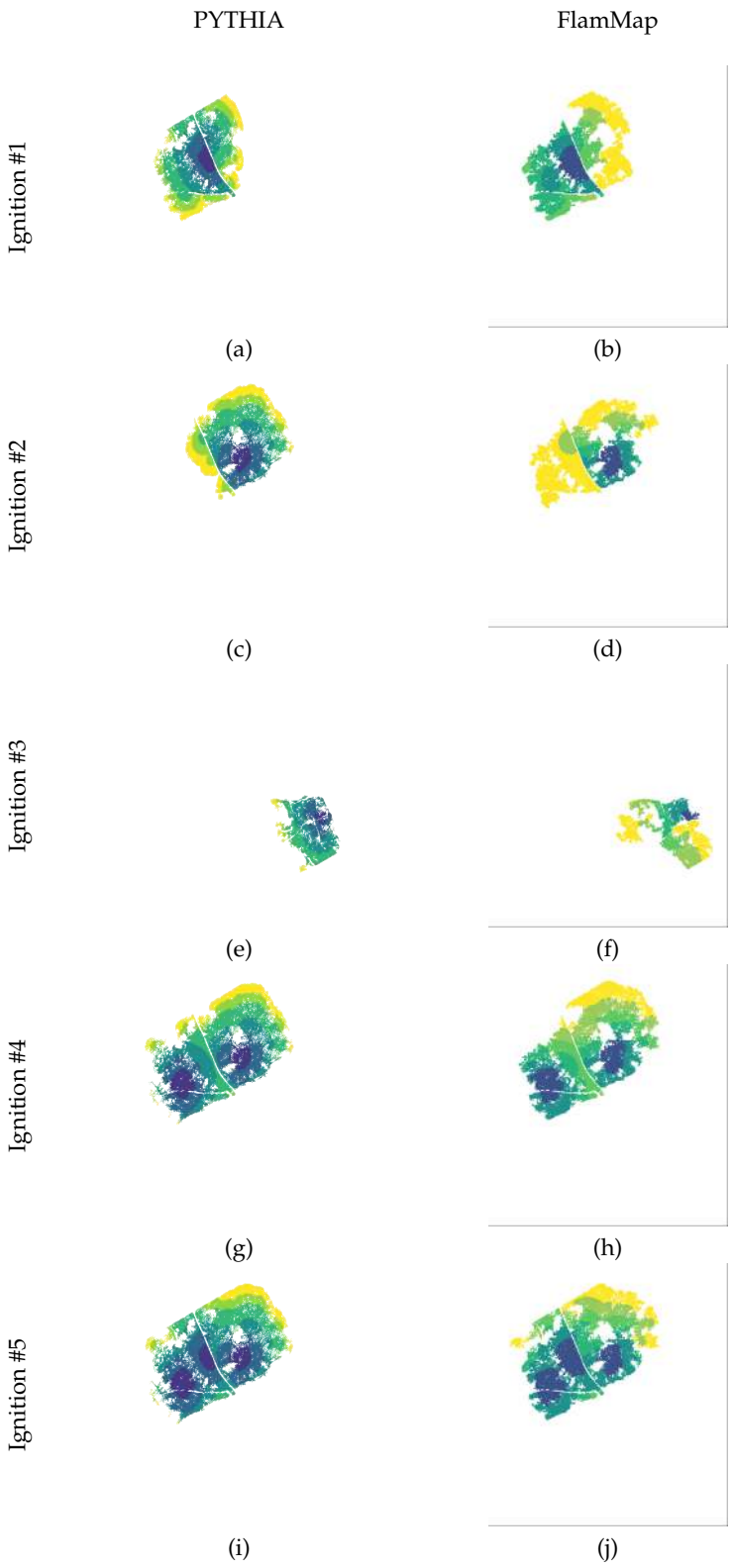

Figure 5.13: Map A fire progression results with weather preset #1, computed with a scale of 1 pixel per square meter. Each color represents one hour of advancement.

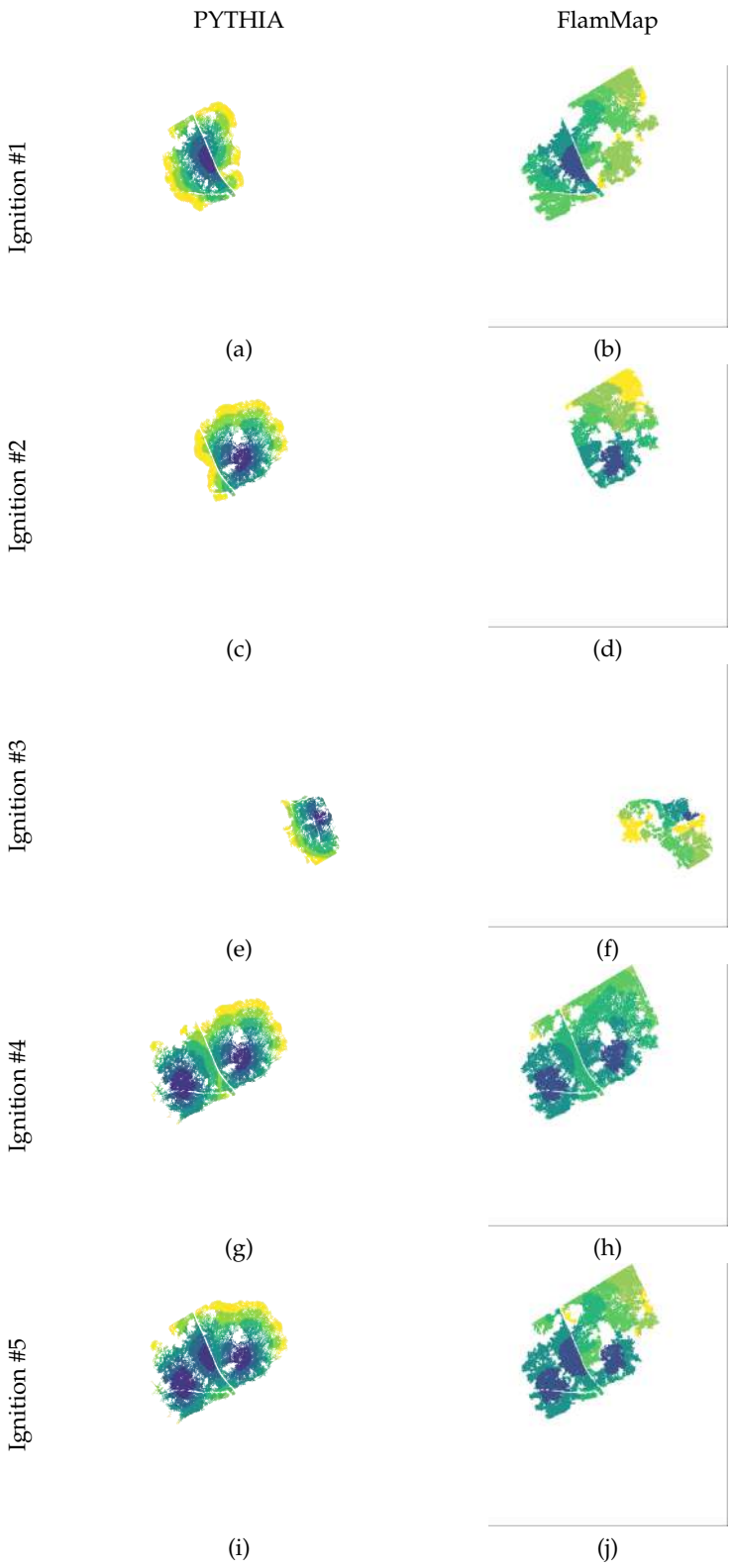

Figure 5.14: Map A fire progression results with weather preset #2, computed with a scale of 1 pixel per square meter. Each color represents one hour of advancement.

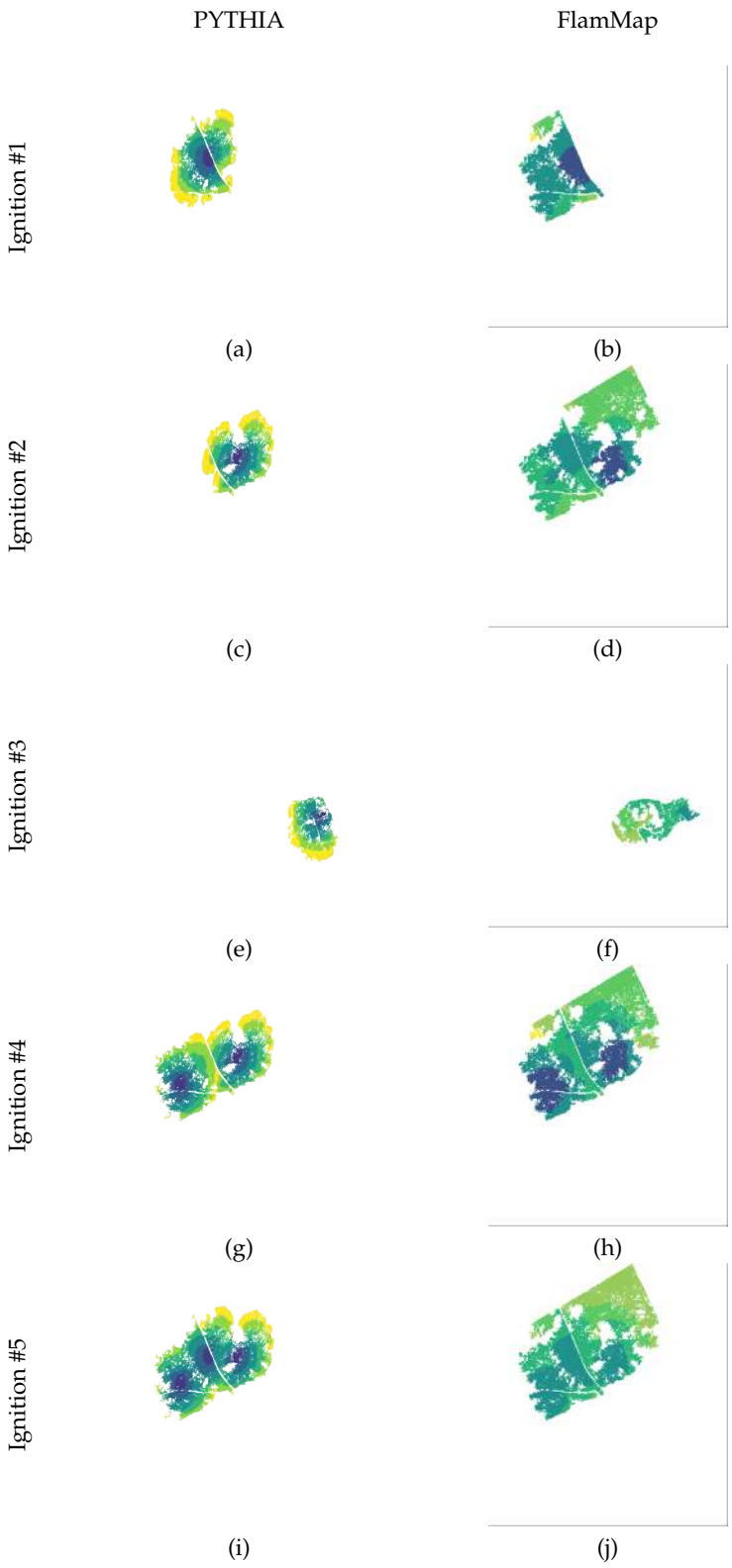

Figure 5.15: Map A fire progression results with weather preset #3, computed with a scale of 1 pixel per square meter. Each color represents one hour of advancement.

5.3.5.5 Assessment on Map B

Similar to Map A, fifteen distinct simulations were conducted on this map, each simulating the progression of a fire over a three-hour period, given the map's smaller scale.

The results for Map B are, overall, less favorable compared to the outcomes in the two preceding scenarios. However, examining W1 (Figure 5.16), it is evident that the similarity with the expected outcome remains exceptionally high. On the contrary, the performance for W2 and W3 (Figures 5.17and5.18) is noticeably weaker in comparison to our previous observations.

Despite the relatively poorer results, it is noteworthy that the overall direction of the fire and its shape propagation is still in the correct trajectory.

5.3.5.6 Results Analysis

The PYTHIA and FlamMap results were mapped to the exact same color gradient and statistically compared based on pixel value—this would give an estimation of an accuracy value that could be used to objectively evaluate the results. These can be found on Table 5.11.

Confirming previous observations, the accuracy of the Plane Map results exhibited significant variability, ranging from a maximum of $\approx 87\%$ to a minimum of $\approx 55\%$. This range, however, provides a reasonably satisfactory approximation of the expected results. In contrast, most results pertaining to Map A consistently exceeded the 80% mark, resulting in a commendable good average accuracy of $\approx 86\%$ across all tests. As anticipated, Map B yielded weaker outcomes, with an average accuracy of $\approx 86\%$, and it recorded the lowest accuracy among all tests at $\approx 32\%$.

The multiplicative coefficient, as elaborated in Section 5.3.3, proved effective in mitigating the potential burn progression loss, especially evident on Map A, which resulted from the small grid scale. The disparity in outcomes between Maps A and B can be attributed to the smaller scale and the relatively uniform terrain of Map B. It appears that has the wind speed increases—increasing the ROS—smoother surfaces yield less favorable results. This might be due to an additional equalization factor that highly textured regions impart on the ROS due to slope factor impact.

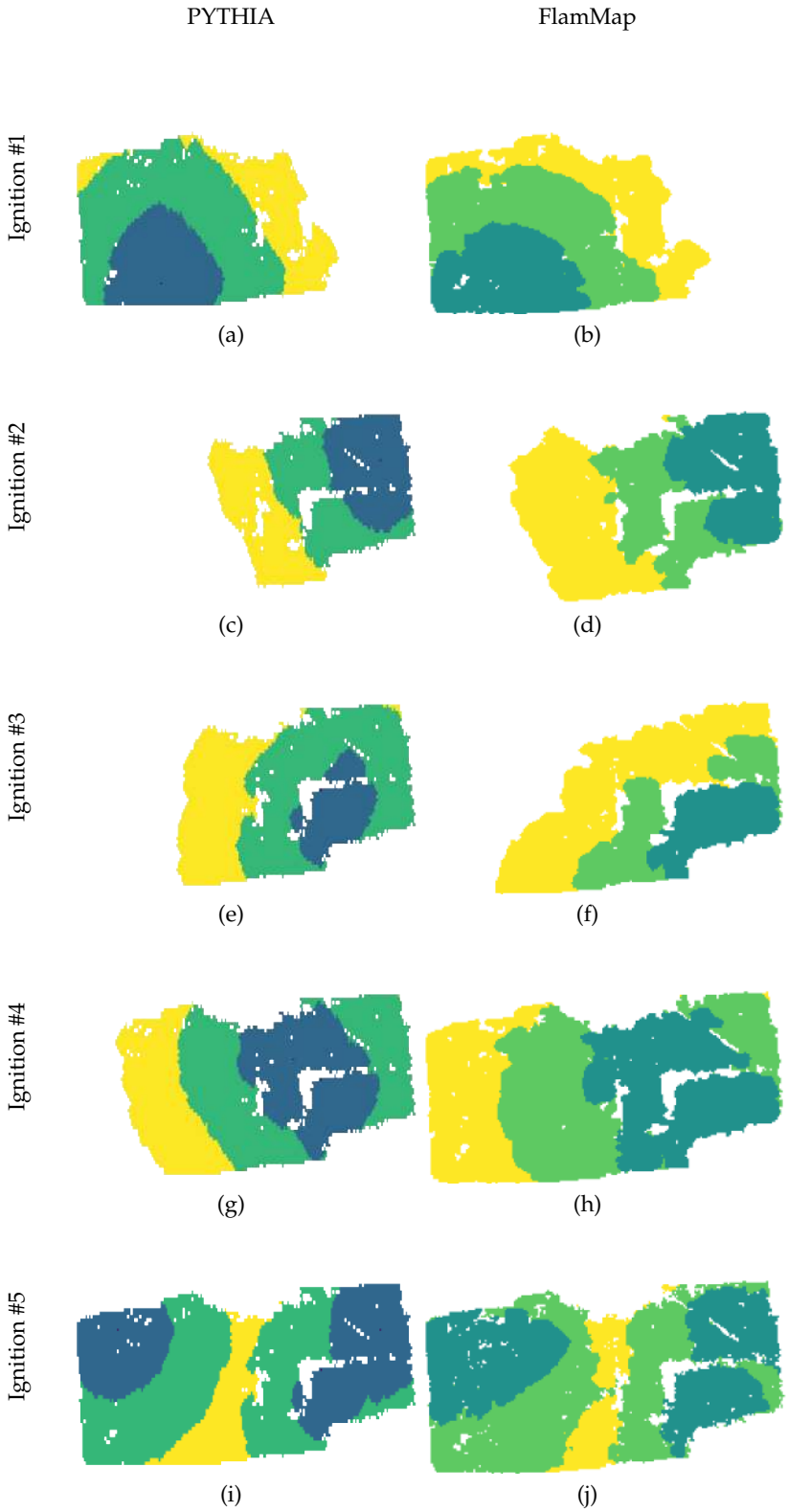

Figure 5.16: Map B results with weather preset #1, computed with a scale of 1 pixel per square meter. Each color represents one hour of advancement.

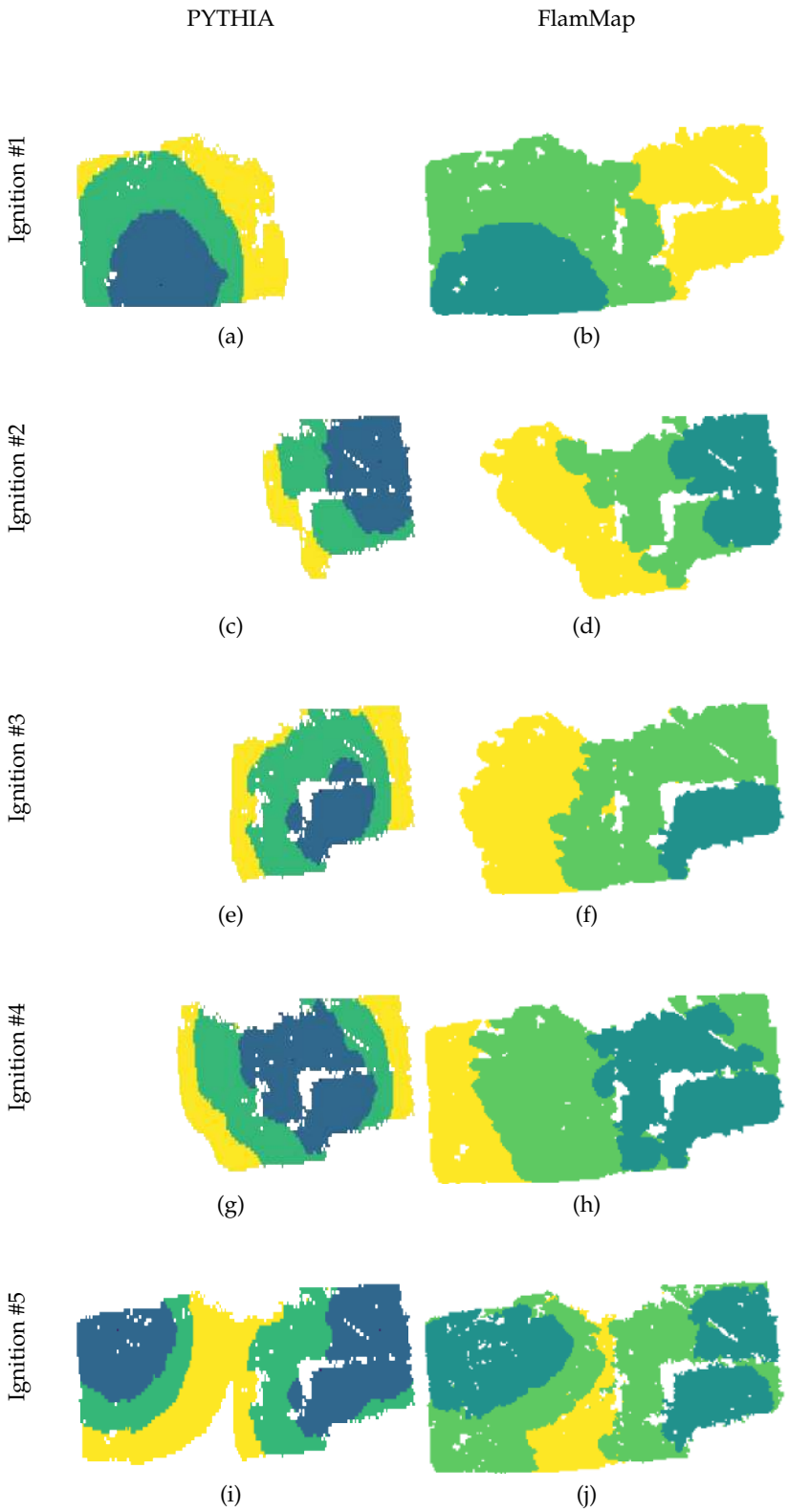

Figure 5.17: Map B results with weather preset #2, computed with a scale of 1 pixel per square meter. Each color represents one hour of advancement.

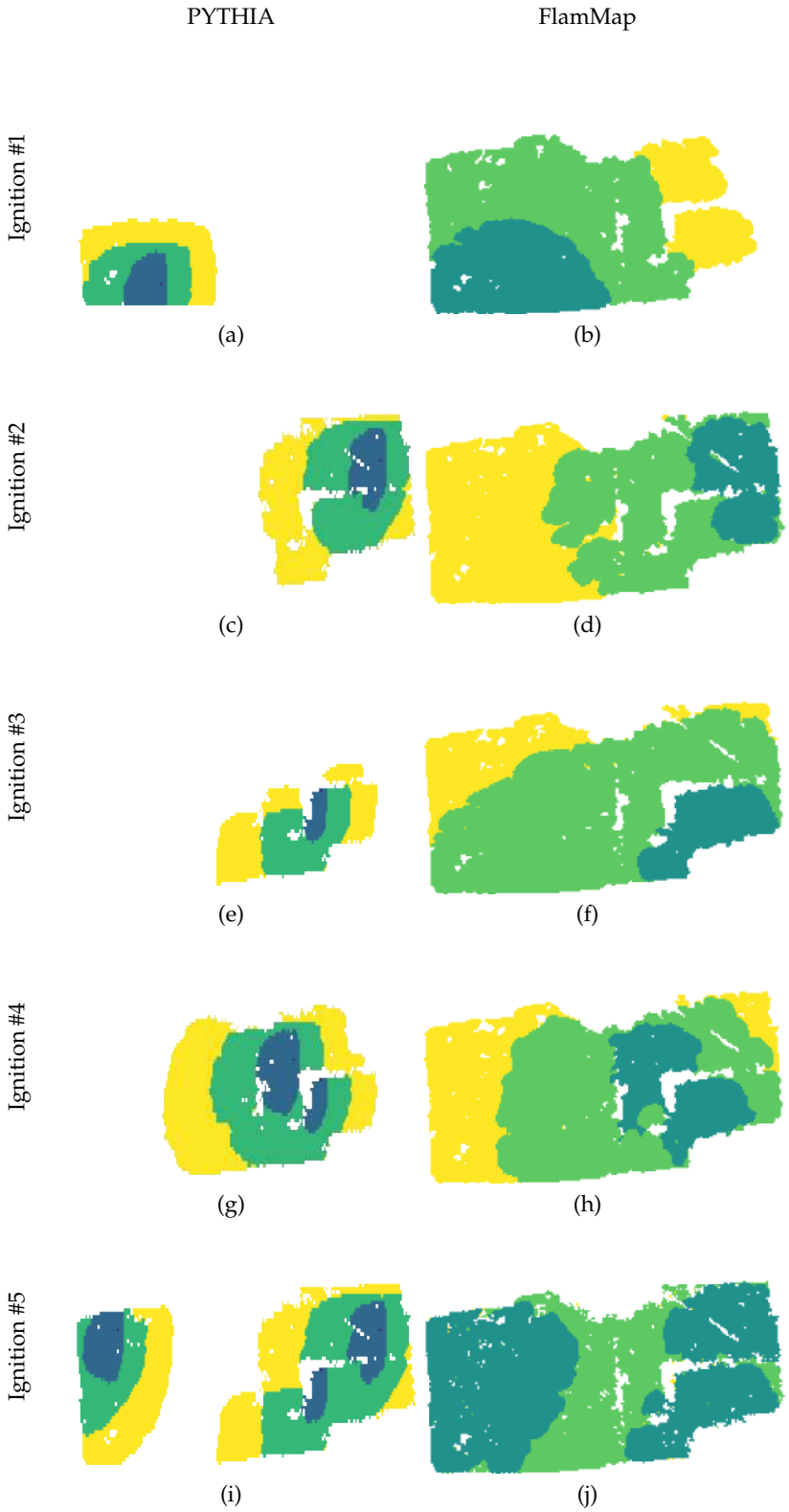

Figure 5.18: Map B results with weather preset #3, computed with a scale of 1 pixel per square meter.

Table 5.11: Accuracy of the PYTHIA results compared to the FlamMap outputs.

Map	Presets		Accuracy (%)
	Wind	Ignition	
Constant	1	1	86.52
	2	1	64.57
	3	1	54.97
Total Constant Map μ			68.69
A	1	1	88.74
		2	88.26
		3	93.74
		4	84.83
		5	84.37
	Map A, W1 μ		87.99
	2	1	82.81
		2	90.73
		3	93.96
		4	81.91
		5	84.02
	Map A, W2 μ		86.69
	3	1	89.25
		2	79.39
		3	93.61
		4	76.93
		5	84.3
	Map A, W3 μ		84.70
Total Map A μ			86.46
B	1	1	73.78
		2	84.87
		3	72.44
		4	72.45
		5	61.21
	Map B, W1 μ		72.95
	2	1	72.12
		2	79.13
		3	70.87
		4	57.34
		5	64.52
	Map B, W2 μ		68.80
	3	1	42.08
		2	65.76
		3	32.33
		4	61.15
		5	52.34
	Map B, W3 μ		50.73
Total Map B μ			64.16

6

Conclusions

This dissertation aimed to establish a comprehensive framework for wildfire simulation, encompassing the intricate task of extracting pertinent information from data collected by UAV. Notably, this work distinguishes itself from existing literature, which tends to focus primarily on either data extraction or simulation, rarely combining both to this extent.

The developed NABU module is competent in extracting terrain and fuel data, easily discerning artificial elements and water features. Furthermore, the applied methodology for vegetation data extraction demonstrates its capacity to generate a reliable representation of the terrain solely through image processing and segmentation. The automatic weather extraction feature is very beneficial within this system, facilitating both historical incident reproduction and the simulation of future events. Additionally, since the modules were designed to work independently, the outputs from the NABU module can easily be adapted for use in other applications.

Regarding the simulation aspect, the results are satisfactory. The PYTHIA module effectively replicated the outcomes of the FlamMap software with satisfactory accuracy, all while demanding fewer input data inputs. However, it does exhibit some problems in terms of progression speed, which can be attributed to the cell scale employed. Nonetheless, the module consistently reproduced the general direction and burn pattern.

During the testing phase, it became apparent that the PYTHIA's accuracy deteriorated with higher wind speeds, particularly for values exceeding 50 km/h, where instability introduced rather pronounced distortions in the results. Nevertheless, the outcomes remain within acceptable bounds. Additionally, certain aspects of the module's implementation, such as the implementation of the fire model, can serve as a starting point for future research endeavors on its own. Finally, outputs such as the burning index maps can be helpful for assessing danger levels and helping formulate effective fire management strategies.

6.1 Contributions

This dissertation makes a valuable contribution to the fields of image processing and wildfire management. Chapter 3 provides a comprehensive overview of multispectral indices specifically tailored for wildfire management. Furthermore, Chapter 5 feature descriptions are intertwined with detailed insights into their implementation. This includes solutions that were thoroughly tested but ultimately did not make it into the final implementation. This is complemented by an extensive library of figures that aid in understanding both the functionality of the modules as well the phenomena they manipulate.

Additionally, during the course of this research, an article focusing on multispectral indices for wildfire management has been produced. A pre-print version is available on arXiv (Oliveira et al., 2023).

6.2 Further Work

There are many avenues open for future work on this dissertation:

- Improvements in automatic data outlier detection and correction. While the current implementation is functioning well, there are areas where instrument errors are easily recognizable but are not affected by the correction.
- Implementation of automatic fuel type recognition rather than requiring user selection of fuel groups.
- Investigation into the possible incorporation of machine learning techniques into the two aforementioned tasks.
- Expansion of the NFDRS 2016 fire model implementation and the possibility of transforming it into a standalone implementation.
- Enhancements in the propagation system for the cellular automaton, including research into alternative grid shapes (such as hexagonal) and possible decrease in the ROS time step to address the current slight speed differences at the scale of 1.
- Improvements in code efficiency, especially concerning highly complex image processing tasks that currently slow down the system, even in a regime of GPU computing.

6.3 Closing Remarks

To conclude this document, it can be affirmed that the thesis objective has been successfully achieved, and the prospects for future work in the advancement of this system are highly promising.

May this work serve as a valuable resource for understanding the complexities of wildfire management and serve as an essential reference point for those venturing into similar development journeys. This document provides a current solution that can serve as a robust foundation for future research in the field, while also serving as a record of the challenges and limitations that may arise during development.

Bibliography

Adorjan, M. (2016). *Opensfm: A collaborative structure-from-motion system* [Doctoral dissertation, Technische Universität Wien]. (Cit. on p. 25).

Alexander, M. E. (1998). *Crown fire thresholds in exotic pine plantations of australasia* [Doctoral dissertation, School of Environment and Society, The Australian National University]. (Cit. on p. 21).

Amer, F., Zhao, Z., Tang, S., & Torres, W. (2018). Constructing locally dense point clouds using opensfm and orb-slam2. *arXiv preprint arXiv:1804.08243* (cit. on p. 25).

Andrews, P. L. (2018). *The rothermel surface fire spread model and associated developments: A comprehensive explanation* (tech. rep.). U.S. Department of Agriculture, Forest Service, Rocky Mountain Research Station. https://doi.org/10.2737/rmrs-gtr-371 (cit. on pp. 48, 113–116).

Atasoy, K., & Kocaman, S. (2021). Development of a geo-analytics platform for post-disaster ground assessment. *International Archives of the Photogrammetry, Remote Sensing & Spatial Information Sciences* (cit. on p. 25).

Ausonio, E., Bagnerini, P., & Ghio, M. (2021). Drone swarms in fire suppression activities: A conceptual framework. *Drones*, *5*(1). https://doi.org/10.3390/drones5010017 (cit. on p. 28).

Aydin, B., Selvi, E., Tao, J., & Starek, M. J. (2019). Use of fire-extinguishing balls for a conceptual system of drone-assisted wildfire fighting. *Drones*, *3*(1). https://doi.org/10.3390/drones3010017 (cit. on pp. 26, 28).

Barnes, E., Clarke, T., Richards, S., Colaizzi, P., Haberland, J., Kostrzewski, M., Waller, P., Choi, C., Riley, E., & Thompson, T. (2000). Coincident detection of crop water stress, nitrogen status, and canopy density using ground based multispectral data (cit. on p. 17).

Barnes, R. (2016). *Richdem: Terrain analysis software*. http://github.com/r-barnes/richdem (cit. on p. 41).

Bertalan, L., Holb, I., Pataki, A., Négyesi, G., Szabó, G., Kupásné Szalóki, A., & Szabó, S. (2022). Uav-based multispectral and thermal cameras to predict soil water content

– a machine learning approach. *Computers and Electronics in Agriculture*, *200*, 107262. https://doi.org/https://doi.org/10.1016/j.compag.2022.107262 (cit. on p. 19).

Berto, S., Carraro, F., Morabito, D., Bonetto, J., & Salemi, G. (2021). The photogrammetric survey of the phoenician and punic necropolis of nora and three-dimensional rendering tools for sharing data. *ArcheoFOSS XIII Workshop—Open Software, Hardware, Processes, Data and Formats in Archaeological Research*. https://doi.org/10.3390/environsciproc2021010017 (cit. on p. 25).

Birth, G. S., & McVey, G. R. (1968). Measuring the color of growing turf with a reflectance spectrophotometer1. *Agronomy Journal*, *60*(6), 640–643. https://doi.org/https://doi.org/10.2134/agronj1968.00021962006000060016x (cit. on p. 17).

Bogdos, N., & Manolakos, E. (2013). A tool for simulation and geo-animation of wildfires with fuel editing and hotspot monitoring capabilities. *Environmental Modelling & Software*, *46*, 182–195. https://doi.org/10.1016/j.envsoft.2013.03.009 (cit. on p. 29).

Bogdos, N., & Manolakos, E. S. (2019). Crowd-sourced wildfire spread prediction with remote georeferencing using smartphones. *IEEE Access*, *7*, 102102–102112. https://doi.org/10.1109/ACCESS.2019.2931456 (cit. on pp. 26, 29, 30).

Bolaño-Diaz, S., Camargo-Caicedo, Y., Tovar Bernal, F., & Bolaño-Ortiz, T. R. (2022). The effect of forest fire events on air quality: A case study of northern colombia. *Fire*, *5*(6). https://doi.org/10.3390/fire5060191 (cit. on p. 25).

California Department of Forestry and Fire Protection. (2022, November). 20 largest california wildfires. https://www.fire.ca.gov/ (cit. on p. 2).

Carey, C., Romero, J., & Laefer, D. F. (2021). New potree shader capabilities for 3d visualization of behaviors near covid-19 rich healthcare facilities. *The International Archives of Photogrammetry, Remote Sensing and Spatial Information Sciences*, *46*, 61–66 (cit. on p. 25).

Casula, M., Arca, B., Laneve, G., Cadau, E., Bua, R., Pedes, F., Salis, M., Andronico, P., Ventura, A., Casula, F., & Cao, M. (2022). Integrated platform for wildfire prevention and management: The s2igi project. *Environmental Sciences Proceedings*, *17*(1). https://doi.org/10.3390/environsciproc2022017088 (cit. on pp. 26, 28).

Centre, E. C. J. R. (2021). *Forest fires in europe, middle east and north africa 2020*. Publications Office. https://doi.org/10.2760/059331 (cit. on pp. 2, 3, 8).

Chen, J. M. (1996). Evaluation of vegetation indices and a modified simple ratio for boreal applications. *Canadian Journal of Remote Sensing*, *22*(3), 229–242. https://doi.org/10.1080/07038992.1996.10855178 (cit. on p. 17).

Chen, S., Li, W., Cao, Y., & Lu, X. (2022). Combining the convolution and transformer for classification of smoke-like scenes in remote sensing images. *IEEE Transactions on Geoscience and Remote Sensing*, *60*, 1–19. https://doi.org/10.1109/TGRS.2022.3208120 (cit. on p. 26).

Chuvieco, E., Martín, M. P., & Palacios, A. (2002). Assessment of different spectral indices in the red-near-infrared spectral domain for burned land discrimination.

International Journal of Remote Sensing, *23*(23), 5103–5110. https://doi.org/10.1080/01431160210153129 (cit. on p. 20).

Chuvieco, E., & Martín, M. (1998). Cartografía de grandes incendios forestales en la península ibérica a partir de imágenes noaa-avhrr. *Serie Geográfica*, *7* (cit. on p. 17).

Contributors, T. (2023). TRY plant database [https://www.try-db.org/TryWeb/, Last Accessed on 26-04-2023]. (Cit. on p. 33).

Cruz, H., Eckert, M., Meneses, J., & Martínez, J.-F. (2016). Efficient forest fire detection index for application in unmanned aerial systems (uass). *Sensors*, *16*(6). https://doi.org/10.3390/s16060893 (cit. on p. 28).

Daigo, M., Ono†, A., Urabe, R., & Fujiwara, N. (2004). Pattern decomposition method for hyper-multi-spectral data analysis. *International Journal of Remote Sensing*, *25*(6), 1153–1166. https://doi.org/10.1080/0143116031000139872 (cit. on p. 18).

de Castro, C. F., Serra, G., Parola, J., Reis, J., Lourenço, L., & Correia, S. (2006). Combate a incêndios florestais. *Escola Nacional de Bombeiros*, *13* (cit. on p. 7).

Deng, J., Pan, S., Zhou, M., Gao, W., Yan, Y., Niu, Z., & Han, W. (2023). Optimum sampling window size and vegetation index selection for low-altitude multispectral estimation of root soil moisture content for xuxiang kiwifruit. *Agricultural Water Management*, *282*, 108297. https://doi.org/https://doi.org/10.1016/j.agwat.2023.108297 (cit. on p. 19).

Di Biase, V., & Laneve, G. (2018). Geostationary sensor based forest fire detection and monitoring: An improved version of the sfide algorithm. *Remote Sensing*, *10*(5). https://doi.org/10.3390/rs10050741 (cit. on p. 28).

do Mar e da Atmosfera, I. P. (2023). IPMA api [https://api.ipma.pt/, Last Accessed on 20-06-2023]. (Cit. on p. 45).

Du Fei, L. J., Hou Zongze. (2001). Method of ground fire boundaries spread modeling and computer simulation. *Fire Safety science*, *10*(4), 204–208 (cit. on p. 21).

Fernandes, P., & Loureiro, C. (2022, January). *Modelos de combustível florestal para portugal - documento de referência, versão de 2021* (tech. rep.). Departamento de Ciências Florestais e Arquitetura Paisagista, UTAD. (Cit. on pp. 34, 35).

Finney, M. A. (n.d.). *Flammap: Fire mapping and analysis system* (Version 6.0). https://www.firelab.org/media/709 (cit. on p. 35).

Finney, M. A. (1998). *Farsite, fire area simulator–model development and evaluation*. US Department of Agriculture, Forest Service, Rocky Mountain Research Station. (Cit. on pp. 24, 36).

Finney, M. A. (2006). An overview of flammap fire modeling capabilities. *In: Andrews, Patricia L.; Butler, Bret W., comps. 2006. Fuels Management-How to Measure Success: Conference Proceedings. 28-30 March 2006; Portland, OR. Proceedings RMRS-P-41. Fort Collins, CO: US Department of Agriculture, Forest Service, Rocky Mountain Research Station. p. 213-220*, *41* (cit. on p. 36).

Gao, B.-c. (1996). Ndwi—a normalized difference water index for remote sensing of vegetation liquid water from space. *Remote Sensing of Environment*, *58*(3), 257–266. https://doi.org/https://doi.org/10.1016/S0034-4257(96)00067-3 (cit. on p. 17).

García, M. L., & Caselles, V. (1991). Mapping burns and natural reforestation using thematic mapper data. *Geocarto International*, *6*(1), 31–37. https://doi.org/10.1080/10106049109354290 (cit. on p. 17).

Gboloo, A. T. (2017, March). *Global environmental awareness on climate change: Forest protection*. MindStir Media. (Cit. on p. 7).

GDAL/OGR contributors. (2023). *GDAL/OGR geospatial data abstraction software library*. Open Source Geospatial Foundation. https://doi.org/10.5281/zenodo.5884351 (cit. on p. 39).

Gill, A., Groves, R., Noble, I., & of Science, A. A. (1981). *Fire and the australian biota*. Australian Academy of Science. (Cit. on p. 21).

Gitelson, A. A., Kaufman, Y. J., & Merzlyak, M. N. (1996). Use of a green channel in remote sensing of global vegetation from eos-modis. *Remote Sensing of Environment*, *58*(3), 289–298. https://doi.org/https://doi.org/10.1016/S0034-4257(96)00072-7 (cit. on p. 17).

Gonenc, A., Ozerdem, M. S., & Acar, E. (2019). Comparison of ndvi and rvi vegetation indices using satellite images. *2019 8th International Conference on Agro-Geoinformatics (Agro-Geoinformatics)*, 1–4. https://doi.org/10.1109/Agro-Geoinformatics.2019.8820225 (cit. on p. 16).

Guede-Fernández, F., Martins, L., de Almeida, R. V., Gamboa, H., & Vieira, P. (2021). A deep learning based object identification system for forest fire detection. *Fire*, *4*(4). https://doi.org/10.3390/fire4040075 (cit. on p. 26).

Guo, L., Fu, P., Shi, T., Chen, Y., Zhang, H., Meng, R., & Wang, S. (2020). Mapping field-scale soil organic carbon with unmanned aircraft system-acquired time series multispectral images. *Soil and Tillage Research*, *196*, 104477. https://doi.org/https://doi.org/10.1016/j.still.2019.104477 (cit. on p. 19).

Guo, L., Sun, X., Fu, P., Shi, T., Dang, L., Chen, Y., Linderman, M., Zhang, G., Zhang, Y., Jiang, Q., Zhang, H., & Zeng, C. (2021). Mapping soil organic carbon stock by hyperspectral and time-series multispectral remote sensing images in low-relief agricultural areas. *Geoderma*, *398*, 115118. https://doi.org/https://doi.org/10.1016/j.geoderma.2021.115118 (cit. on p. 19).

Holden, Z. A., Smith, A. M. S., Morgan, P., Rollins, M. G., & Gessler, P. E. (2005a). Evaluation of novel thermally enhanced spectral indices for mapping fire perimeters and comparisons with fire atlas data. *International Journal of Remote Sensing*, *26*(21), 4801–4808. https://doi.org/10.1080/01431160500239008 (cit. on p. 17).

Holden, Z. A., Smith, A. M. S., Morgan, P., Rollins, M. G., & Gessler, P. E. (2005b). Evaluation of novel thermally enhanced spectral indices for mapping fire perimeters and comparisons with fire atlas data. *International Journal of Remote Sensing*, *26*(21), 4801–4808. https://doi.org/10.1080/01431160500239008 (cit. on p. 20).

Horn, B. (1981). Hill shading and the reflectance map. *Proceedings of the IEEE*, *69*(1), 14–47. https://doi.org/10.1109/proc.1981.11918 (cit. on p. 41).

Huete, A. (1988). A soil-adjusted vegetation index (SAVI). *Remote Sensing of Environment*, *25*(3), 295–309. https://doi.org/10.1016/0034-4257(88)90106-x (cit. on p. 17).

Hyeong-su, K., Jin-Woo, K., Yun, S., & Kim, W.-T. (2019). A novel wildfire digital-twin framework using interactive wildfire spread simulator. *2019 Eleventh International Conference on Ubiquitous and Future Networks (ICUFN)*, 636–638. https://doi.org/10.1109/ICUFN.2019.8806107 (cit. on pp. 23, 24).

Ivanova, S., Prosekov, A., & Kaledin, A. (2022). A survey on monitoring of wild animals during fires using drones. *Fire*, *5*(3). https://doi.org/10.3390/fire5030060 (cit. on p. 25).

Jiang, H., Mao, Z.-Y., & Wang, X.-Q. (2011). A topography-adjusted vegetation index (tavi) and its application in dynamic forest monitoring. *Beijing Linye Daxue Xuebao/Journal of Beijing Forestry University*, *33*, 8–12 (cit. on p. 17).

Jiang, Z., Huete, A. R., Chen, J., Chen, Y., Li, J., Yan, G., & Zhang, X. (2006). Analysis of ndvi and scaled difference vegetation index retrievals of vegetation fraction. *Remote Sensing of Environment*, *101*(3), 366–378. https://doi.org/https://doi.org/10.1016/j.rse.2006.01.003 (cit. on p. 17).

Jiao, Z., Zhang, Y., Mu, L., Xin, J., Jiao, S., Liu, H., & Liu, D. (2020). *A yolov3-based learning strategy for real-time uav-based forest fire detection*. https://doi.org/10.1109/CCDC49329.2020.9163816 (cit. on p. 29).

Jiao, Z., Zhang, Y., Xin, J., Mu, L., Yi, Y., Liu, H., & Liu, D. (2019). A deep learning based forest fire detection approach using uav and yolov3. *2019 1st International Conference on Industrial Artificial Intelligence (IAI)*, 1–5. https://doi.org/10.1109/ICIAI.2019.8850815 (cit. on p. 28).

Jingguo, T., Shudong, W., Lifu, Z., Taixia, W., Xiaojun, S., & Hailing, J. (2015). Evaluating different vegetation index for estimating lai of winter wheat using hyperspectral remote sensing data. *2015 7th Workshop on Hyperspectral Image and Signal Processing: Evolution in Remote Sensing (WHISPERS)*, 1–4. https://doi.org/10.1109/WHISPERS.2015.8075437 (cit. on p. 18).

Kalpoma, K. A., Chowdhury, A., Arony, N. N., Nowshin, M., & Kudoh, J.-i. (2019). New modis vegetation index for boro rice model using 3d plot and k-nn: Bangladesh haor region perspective. *IGARSS 2019 - 2019 IEEE International Geoscience and Remote Sensing Symposium*, 7322–7325. https://doi.org/10.1109/IGARSS.2019.8898950 (cit. on p. 16).

Kang, Y., Özdoğan, M., Zipper, S. C., Román, M. O., Walker, J., Hong, S. Y., Marshall, M., Magliulo, V., Moreno, J., Alonso, L., Miyata, A., Kimball, B., & Loheide, S. P. (2016). How universal is the relationship between remotely sensed vegetation indices and crop leaf area index? a global assessment. *Remote Sensing*, *8*(7). https://doi.org/10.3390/rs8070597 (cit. on p. 18).

Karma, S., Zorba, E., Pallis, G., Statheropoulos, G., Balta, I., Mikedi, K., Vamvakari, J., Pappa, A., Chalaris, M., Xanthopoulos, G., & Statheropoulos, M. (2015). Use of unmanned vehicles in search and rescue operations in forest fires: Advantages and limitations observed in a field trial. *International Journal of Disaster Risk Reduction*, *13*, 307–312. https://doi.org/https://doi.org/10.1016/j.ijdrr.2015.07.009 (cit. on pp. 26, 28).

Key, C., & Benson, N. (2006, January). Landscape assessment: Ground measure of severity, the composite burn index; and remote sensing of severity, the normalized burn ratio. (Cit. on p. 20).

Ko, B., Kwak, J.-Y., & Nam, J.-Y. (2012). Wildfire smoke detection using temporospatial features and random forest classifiers. *Optical Engineering*, *51*, 7208–. https://doi.org/10.1117/1.OE.51.1.017208 (cit. on p. 26).

Kumar, A. Y., Noufia, M., Shahira, K., & Ramiya, A. (2019). Building information modelling of a multi storey building using terrestrial laser scanner and visualisation using potree: An open source point cloud renderer. *The International Archives of Photogrammetry, Remote Sensing and Spatial Information Sciences*, *42*, 421–426 (cit. on p. 25).

Leblanc, S. G., Chen, J. M., White, H. P., Cihlar, J., Lacaze, R., Roujean, J.-L., & Latifovic, R. (2001). Mapping vegetation clumping index from directional satellite measurements (cit. on p. 17).

Li, X., Gao, Z., Bai, L., & Huang, Y. (2012). Potential of high resolution rapideye data for sparse vegetation fraction mapping in arid regions. *2012 IEEE International Geoscience and Remote Sensing Symposium*, 420–423. https://doi.org/10.1109/IGARSS.2012.6351548 (cit. on p. 18).

Li, X., Zhang, M., Zhang, S., Liu, J., Sun, S., Hu, T., & Sun, L. (2022). Simulating forest fire spread with cellular automation driven by a lstm based speed model. *Fire*, *5*(1). https://doi.org/10.3390/fire5010013 (cit. on pp. 21, 22).

Lillesand, T., Kiefer, R. W., & Chipman, J. (2015). *Remote sensing and image interpretation* (7th ed.). John Wiley & Sons. (Cit. on p. 11).

Lin, Z., Liu, H. H. T., & Wotton, M. (2019). Kalman filter-based large-scale wildfire monitoring with a system of uavs. *IEEE Transactions on Industrial Electronics*, *66*(1), 606–615. https://doi.org/10.1109/TIE.2018.2823658 (cit. on p. 28).

Liu, H. Q., & Huete, A. R. (1995). A feedback based modification of the ndvi to minimize canopy background and atmospheric noise. *IEEE Transactions on Geoscience and Remote Sensing*, *33*, 457–465 (cit. on p. 17).

Liu, S., Zeng, W., Wu, L., Lei, G., Chen, H., Gaiser, T., & Srivastava, A. K. (2021). Simulating the leaf area index of rice from multispectral images. *Remote Sensing*, *13*(18). https://doi.org/10.3390/rs13183663 (cit. on p. 18).

Liu, X., He, B., Quan, X., Wen, C., & Liu, X. (2018). Estimation of wildfire spread rate from geostationary satellite data. *IGARSS 2018 - 2018 IEEE International Geoscience and*

Remote Sensing Symposium, 5457–5460. https://doi.org/10.1109/IGARSS.2018.8517934 (cit. on p. 22).

Long, J., Shelhamer, E., & Darrell, T. (2015). Fully convolutional networks for semantic segmentation. *Proceedings of the IEEE conference on computer vision and pattern recognition*, 3431–3440 (cit. on p. 27).

Lourenço, J. M. (2021). *The NOVAthesis LaTeX Template User's Manual*. NOVA University Lisbon. https://github.com/joaomlourenco/novathesis/raw/main/template.pdf (cit. on p. i).

Lu, H., Koike, T., Tsutsui, H., & Fujii, H. (2011). Monitoring vegetation water content by using optical vegetation index and microwave vegetation index: Field experiments and applications. *2011 IEEE International Geoscience and Remote Sensing Symposium*, 2468–2471. https://doi.org/10.1109/IGARSS.2011.6049711 (cit. on p. 18).

Martins, A., Almeida, J., Almeida, C., Figueiredo, A., Santos, F., Bento, D., Silva, H., & Silva, E. (2007). Forest fire detection with a small fixed wing autonomous aerial vehicle [6th IFAC Symposium on Intelligent Autonomous Vehicles]. *IFAC Proceedings Volumes*, *40*(15), 168–173. https://doi.org/https://doi.org/10.3182/20070903-3-FR-2921.00031 (cit. on p. 28).

McCarthy, N. F., Tohidi, A., Valero, M. M., Dennie, M., Aziz, Y., & Hu, N. (2020). A machine learning solution for operational remote sensing of active wildfires. *IGARSS 2020 - 2020 IEEE International Geoscience and Remote Sensing Symposium*, 6802–6805. https://doi.org/10.1109/IGARSS39084.2020.9324119 (cit. on pp. 26–28).

Meza, J., Marrugo, A. G., Ospina, G., Guerrero, M., & Romero, L. A. (2019). A structure-from-motion pipeline for generating digital elevation models for surface-runoff analysis. *Journal of Physics: Conference Series*, *1247*(1), 012039 (cit. on p. 25).

MicaSense. (2020). *Micasense rededge-mx and dls 2 integration guide*. https://support.micasense.com/hc/en-us/article_attachments/1500011727381 (cit. on p. 36).

Mourad, R., Jaafar, H., Anderson, M., & Gao, F. (2020). Assessment of leaf area index models using harmonized landsat and sentinel-2 surface reflectance data over a semi-arid irrigated landscape. *Remote Sensing*, *12*(19). https://doi.org/10.3390/rs12193121 (cit. on p. 18).

Mummoorthy, A., Chandrika, R., Ganesh, N., & Pavithra, E. (2019). Satellite image processing biomass estimation. *2019 International Conference on Emerging Trends in Science and Engineering (ICESE)*, *1*, 1–7. https://doi.org/10.1109/ICESE46178.2019.9194688 (cit. on p. 16).

National Interagency Fire Center. (2022, November). Wildfires and acres statistics. https://www.nifc.gov/fire-information/statistics/wildfires (cit. on p. 2).

Nex, F., & Remondino, F. (2019). Preface: Latest developments, methodologies, and applications based on uav platforms. *Drones*, *3*(1). https://doi.org/10.3390/drones3010026 (cit. on p. 28).

Nguyen, C. T., Chidthaisong, A., Kieu Diem, P., & Huo, L.-Z. (2021). A modified bare soil index to identify bare land features during agricultural fallow-period in southeast asia using landsat 8. *Land*, *10*(3). https://doi.org/10.3390/land10030231 (cit. on p. 17).

NWCG. (2014, July). *Fire behavior field reference guide, pms 437* (tech. rep.). National Wildfire Coordinating Group. (Cit. on pp. 33, 35).

Oliveira, A., Matos-Carvalho, J. P., Moutinho, F., & Fachada, N. (2023). Multispectral indices for wildfire management. (Cit. on p. 68).

Pham, H., La, H., Feil-Seifer, D., & Deans, M. (2017). A distributed control framework for a team of unmanned aerial vehicles for dynamic wildfire tracking. https://doi.org/10.1109/IROS.2017.8206579 (cit. on p. 26).

Puttinaovarat, S., & Horkaew, P. (2018). Multi-spectral and topographic fusion for automated road extraction. *Open Geosciences*, *10*(1), 461–473. https://doi.org/doi:10.1515/geo-2018-0036 (cit. on p. 20).

Qi, J., Chehbouni, A., Huete, A., Kerr, Y., & Sorooshian, S. (1994). A modified soil adjusted vegetation index. *Remote Sensing of Environment*, *48*(2), 119–126. https://doi.org/https://doi.org/10.1016/0034-4257(94)90134-1 (cit. on p. 17).

Redmon, J., & Farhadi, A. (2018). Yolov3: An incremental improvement. *CoRR*, *abs/1804.02767*. http://arxiv.org/abs/1804.02767 (cit. on p. 29).

Rondeaux, G., Steven, M., & Frederic, B. (1996). Optimization of soil-adjusted vegetation indices. *Remote Sensing of Environment*, *55*, 95–107. https://doi.org/10.1016/0034-4257(95)00186-7 (cit. on p. 17).

Rothermel, R. C. (1972). *A mathematical model for predicting fire spread in wildland fuels* (Vol. 115). Intermountain Forest & Range Experiment Station, Forest Service, US . . . (Cit. on p. 21).

Rouse, J., J. W., Haas, R. H., Schell, J. A., & Deering, D. W. (1974). Monitoring Vegetation Systems in the Great Plains with Erts. In *Nasa special publication* (p. 309, Vol. 351). (Cit. on p. 17).

Rui, X., Hui, S., Yu, X., Zhang, G., & Wu, B. (2018). Forest fire spread simulation algorithm based on cellular automata. *Natural Hazards: Journal of the International Society for the Prevention and Mitigation of Natural Hazards*, *91*(1), 309–319. https://doi.org/10.1007/s11069-017-3127-5 (cit. on p. 21).

Salvado, A. B., Mendonça, R., Lourenço, A., Marques, F., Matos-Carvalho, J. P., Miguel Campos, L., & Barata, J. (2019). Semantic navigation mapping from aerial multispectral imagery. *2019 IEEE 28th International Symposium on Industrial Electronics (ISIE)*, 1192–1197. https://doi.org/10.1109/ISIE.2019.8781301 (cit. on p. 16).

Sandholt, I., Rasmussen, K., & Andersen, J. (2002). A simple interpretation of the surface temperature/vegetation index space for assessment of surface moisture status [Recent Advances in Remote Sensing of Biophysical Variables]. *Remote Sensing of Environment*, *79*(2), 213–224. https://doi.org/https://doi.org/10.1016/S0034-4257(01)00274-7 (cit. on p. 19).

Schütz, M. (2016, September). *Potree: Rendering large point clouds in web browsers* [Doctoral dissertation]. (Cit. on p. 24).

Seo, M.-G., Shin, H.-S., & Tsourdos, A. (2021). Soil moisture retrieval model design with multispectral and infrared images from unmanned aerial vehicles using convolutional neural network. *Agronomy*, *11*(2). https://doi.org/10.3390/agronomy11020398 (cit. on p. 19).

Seraj, E., & Gombolay, M. (2020). Coordinated control of uavs for human-centered active sensing of wildfires. *2020 American Control Conference (ACC)*, 1845–1852 (cit. on pp. 26, 28).

Shahi, K., Shafri, H. Z., Taherzadeh, E., Mansor, S., & Muniandy, R. (2015). A novel spectral index to automatically extract road networks from worldview-2 satellite imagery. *The Egyptian Journal of Remote Sensing and Space Science*, *18*(1), 27–33. https://doi.org/https://doi.org/10.1016/j.ejrs.2014.12.003 (cit. on pp. 17, 20).

She, X., Zhang, L., Huang, C., & Wang, S. (2016). Comparison of hyperspectral vegetation indices based on casi airborne data. *2016 IEEE International Geoscience and Remote Sensing Symposium (IGARSS)*, 4532–4534. https://doi.org/10.1109/IGARSS.2016.7730182 (cit. on p. 18).

Smith, A. B. (2020). U.s. billion-dollar weather and climate disasters, 1980 - present (ncei accession 0209268). https://doi.org/https://doi.org/10.25921/STKW-7W73 (cit. on p. 2).

Stipaničev, D. (2010). Intelligent forest fire monitoring system–from idea to realization. *Annual 2010/2011 of the Croatian Academy of Engineering*, 58 (cit. on p. 26).

Stipaničev, D., Šerić, L., Braović, M., Krstinić, D., Jakovčević, T., Štula, M., Bugarić, M., & Maras, J. (2012). Vision based wildfire and natural risk observers. *2012 3rd International Conference on Image Processing Theory, Tools and Applications (IPTA)*, 37–42. https://doi.org/10.1109/IPTA.2012.6469518 (cit. on pp. 26, 27).

Sun, Y., Ren, H., Zhang, T., Zhang, C., & Qin, Q. (2018). Crop leaf area index retrieval based on inverted difference vegetation index and ndvi. *IEEE Geoscience and Remote Sensing Letters*, *15*(11), 1662–1666. https://doi.org/10.1109/LGRS.2018.2856765 (cit. on pp. 16, 17).

Swain, S. R., Chakraborty, P., Panigrahi, N., Vasava, H. B., Reddy, N. N., Roy, S., Majeed, I., & Das, B. S. (2021). Estimation of soil texture using sentinel-2 multispectral imaging data: An ensemble modeling approach. *Soil and Tillage Research*, *213*, 105134. https://doi.org/https://doi.org/10.1016/j.still.2021.105134 (cit. on p. 19).

Team, O. M. (2023). Open Meteo api [https://open-meteo.com/, Last Accessed on 28-06-2023]. (Cit. on p. 45).

The National Wildfire Coordinating Group. (2019, January). *Guide to wildland fire origin and cause determination*. Independently Published. (Cit. on p. 7).

Tsouros, D. C., Terzi, A., Bibi, S., Vakouftsi, F., & Pantzios, V. (2020). Towards a fully open-source system for monitoring of crops with uavs in precision agriculture. *24th Pan-Hellenic Conference on Informatics*, 322–326 (cit. on p. 25).

Tucker, C. J. (1979). Red and photographic infrared linear combinations for monitoring vegetation. *Remote Sensing of Environment*, *8*(2), 127–150. https://doi.org/https://doi.org/10.1016/0034-4257(79)90013-0 (cit. on p. 17).

Vaz, G., Raposo, J., Reis, L., Monteiro, P., & Viegas, D. (2022). Rigid protection system of infrastructures against forest fires. *Fire*, *5*(5). https://doi.org/10.3390/fire5050145 (cit. on p. 25).

Wagner, C. E. V. (1977). Conditions for the start and spread of crown fire. *Canadian Journal of Forest Research*, *7*(1), 23–34. https://doi.org/10.1139/x77-004 (cit. on p. 21).

Wardihani, E., Ramdhani, M., Suharjono, A., Setyawan, T., Hidayat, S. S., Helmy, Widodo, S., Triyono, E., & Saifullah, F. (2018). Real-time forest fire monitoring system using unmanned aerial vehicle. *Journal of Engineering Science and Technology*, *13*, 1587–1594 (cit. on pp. 26, 28).

Weise, D., & Biging, G. (1996). Effects of wind velocity and slope on flame properties. *Canadian Journal of Forest Research-revue Canadienne De Recherche Forestiere - CAN J FOREST RES*, *26*, 1849–1858. https://doi.org/10.1139/x26-210 (cit. on p. 21).

Xie, Q., Huang, W., Liang, D., Chen, P., Wu, C., Yang, G., Zhang, J., Huang, L., & Zhang, D. (2014). Leaf area index estimation using vegetation indices derived from airborne hyperspectral images in winter wheat. *IEEE Journal of Selected Topics in Applied Earth Observations and Remote Sensing*, *7*(8), 3586–3594. https://doi.org/10.1109/JSTARS.2014.2342291 (cit. on p. 18).

Xu, G., & Zhong, X. (2017). Real-time wildfire detection and tracking in australia using geostationary satellite: Himawari-8. *Remote Sensing Letters*, *8*(11), 1052–1061. https://doi.org/10.1080/2150704X.2017.1350303 (cit. on p. 23).

Xu, H. (2006). Modification of normalised difference water index (ndwi) to enhance open water features in remotely sensed imagery. *International Journal of Remote Sensing*, *27*(14), 3025–3033. https://doi.org/10.1080/01431160600589179 (cit. on p. 17).

Yan, K., Gao, S., Chi, H., Qi, J., Song, W., Tong, Y., Mu, X., & Yan, G. (2022). Evaluation of the vegetation-index-based dimidiate pixel model for fractional vegetation cover estimation. *IEEE Transactions on Geoscience and Remote Sensing*, *60*, 1–14. https://doi.org/10.1109/TGRS.2020.3048493 (cit. on p. 18).

Yassemi, S., Dragićević, S., & Schmidt, M. (2008). Design and implementation of an integrated gis-based cellular automata model to characterize forest fire behaviour. *Ecological Modelling*, *210*(1), 71–84. https://doi.org/https://doi.org/10.1016/j.ecolmodel.2007.07.020 (cit. on p. 49).

Yongzhong, Z., Feng, Z.-D., Tao, H., Liyu, W., Kegong, L., & Xin, D. (2004). Simulating wildfire spreading processes in a spatially heterogeneous landscapes using an

improved cellular automaton model. *IGARSS 2004. 2004 IEEE International Geoscience and Remote Sensing Symposium*, *5*, 3371–3374 vol.5. https://doi.org/10.1109/IGARSS.2004.1370427 (cit. on p. 21).

Yun, S., Chen, C., Li, J., & Tang, L. (2011). Wildfire spread simulation and visualization in virtual environments. *Proceedings 2011 IEEE International Conference on Spatial Data Mining and Geographical Knowledge Services*, 315–319. https://doi.org/10.1109/ICSDM.2011.5969054 (cit. on p. 24).

Zhang, L., Furumi, S., Muramatsu, K., Fujiwara, N., Daigo, M., & Zhang, L. (2007). A new vegetation index based on the universal pattern decomposition method. *International Journal of Remote Sensing*, *28*(1), 107–124. https://doi.org/10.1080/01431160600857402 (cit. on p. 17).

Zhang, L., Mitsushita, Y., Furumi, S., Muramatsu, K., Fujiwara, N., Daigo, M., & Zhang, L. (2003). Universality of modified pattern decomposition method for satellite sensors. *Asia GIS Conference Publications, Wuhan University, China* (cit. on p. 18).

Zhao, Y., Ma, J., Li, X., & Zhang, J. (2018). Saliency detection and deep learning-based wildfire identification in uav imagery. *Sensors*, *18*(3). https://doi.org/10.3390/s18030712 (cit. on pp. 26, 28, 29).

Zhao, Y., & Zhu, Z. (2022). Asi: An artificial surface index for landsat 8 imagery. *International Journal of Applied Earth Observation and Geoinformation*, *107*, 102703. https://doi.org/https://doi.org/10.1016/j.jag.2022.102703 (cit. on p. 17).

Zhen, Z., Chen, S., Qin, W., Yan, G., Gastellu-Etchegorry, J.-P., Cao, L., Murefu, M., Li, J., & Han, B. (2020). Potentials and limits of vegetation indices with brdf signatures for soil-noise resistance and estimation of leaf area index. *IEEE Transactions on Geoscience and Remote Sensing*, *58*(7), 5092–5108. https://doi.org/10.1109/TGRS.2020.2972297 (cit. on pp. 17, 18).

Zhou, J., & Chen, J. (2019). Analysis of topographic effects on vegetation indices. *IGARSS 2019 - 2019 IEEE International Geoscience and Remote Sensing Symposium*, 6059–6062. https://doi.org/10.1109/IGARSS.2019.8900603 (cit. on p. 16).

A

NABU Results (Map A)

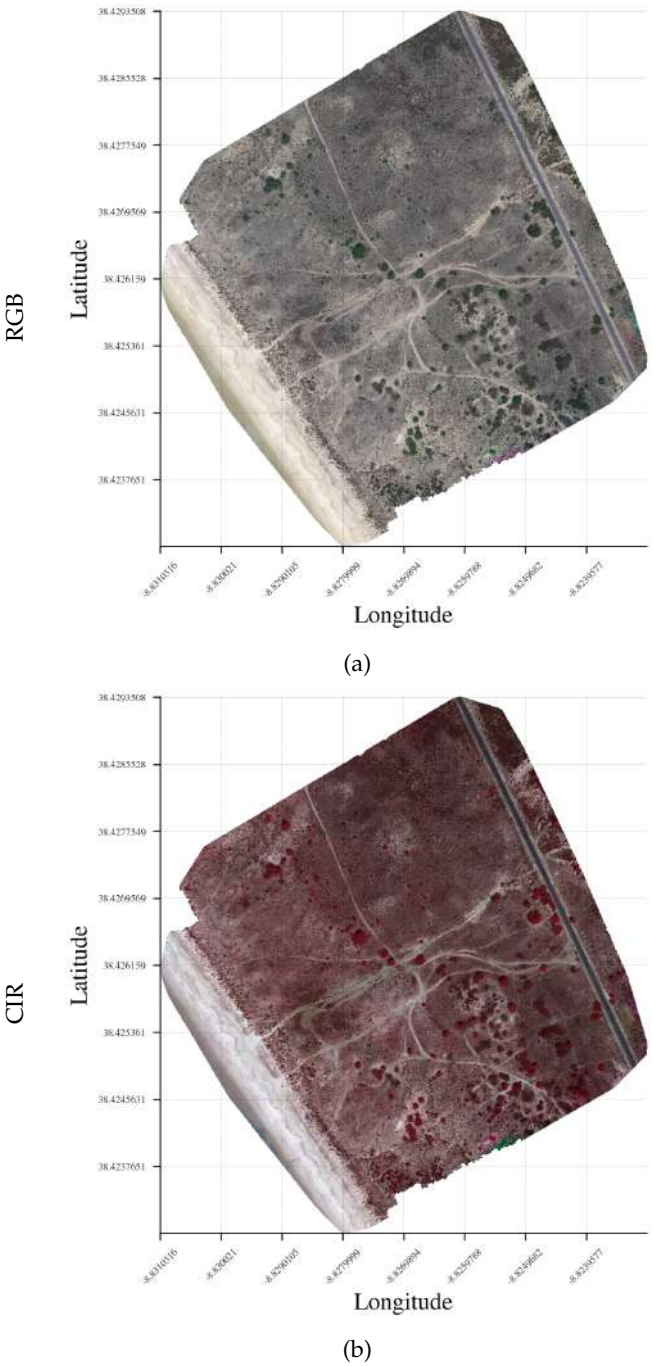

Figure A.1: RGB and CIR (Map A).

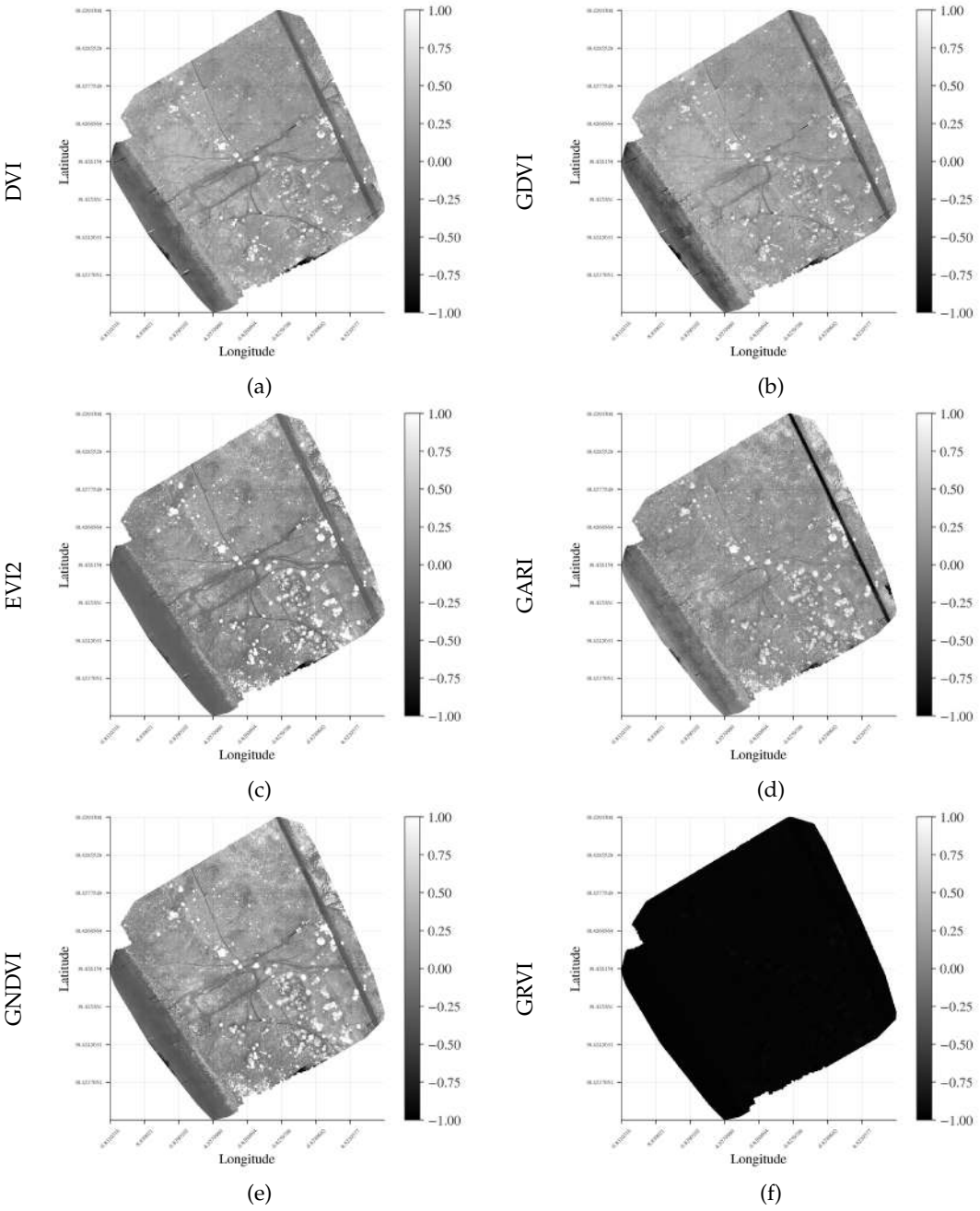

Figure A.2: DVI, GDVI, EVI2, GARI, GNDVI and GRVI (Map A).

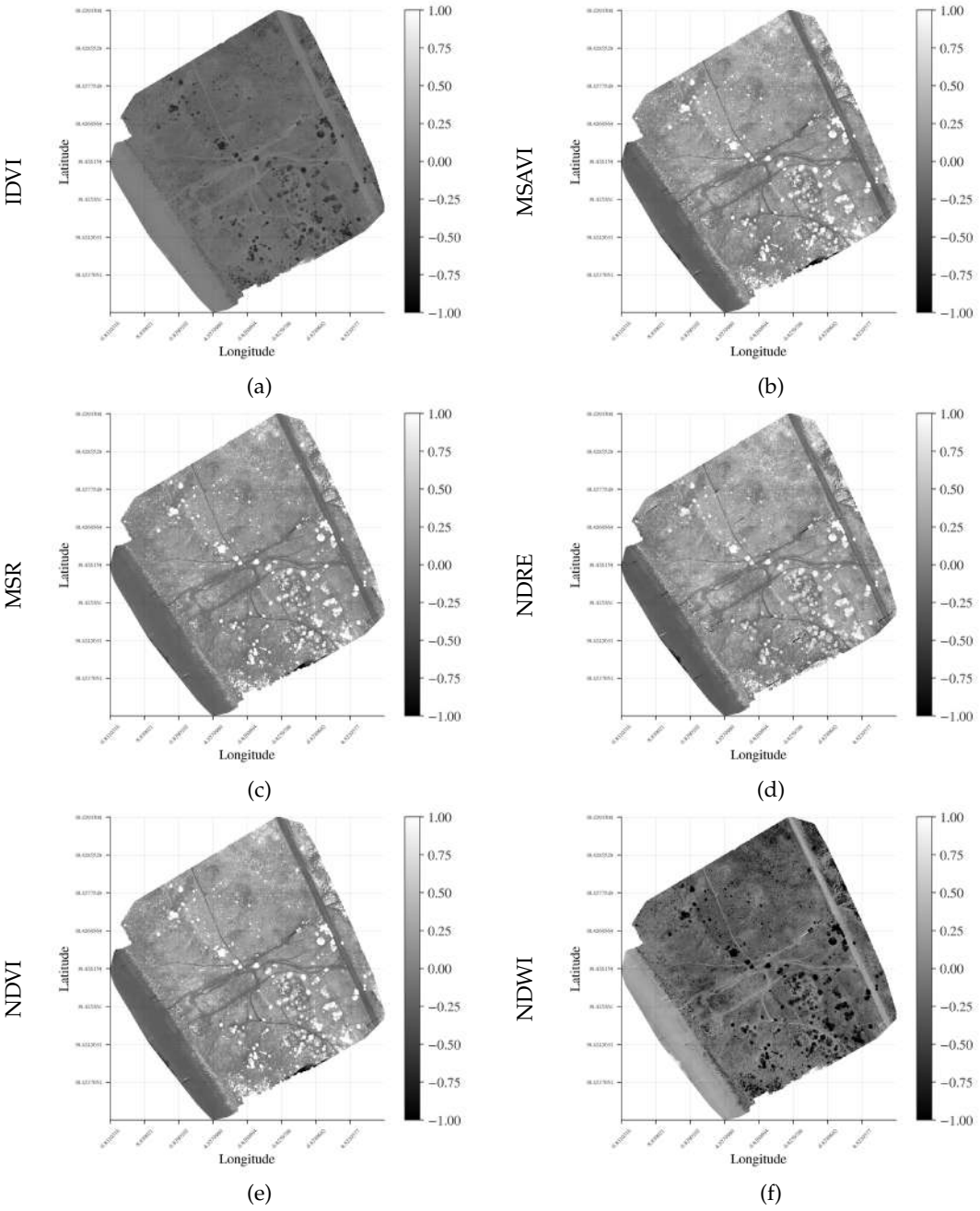

Figure A.3: IDVI, MSAVI, MSR, NDRE, NDVI and NDWI (Map A).

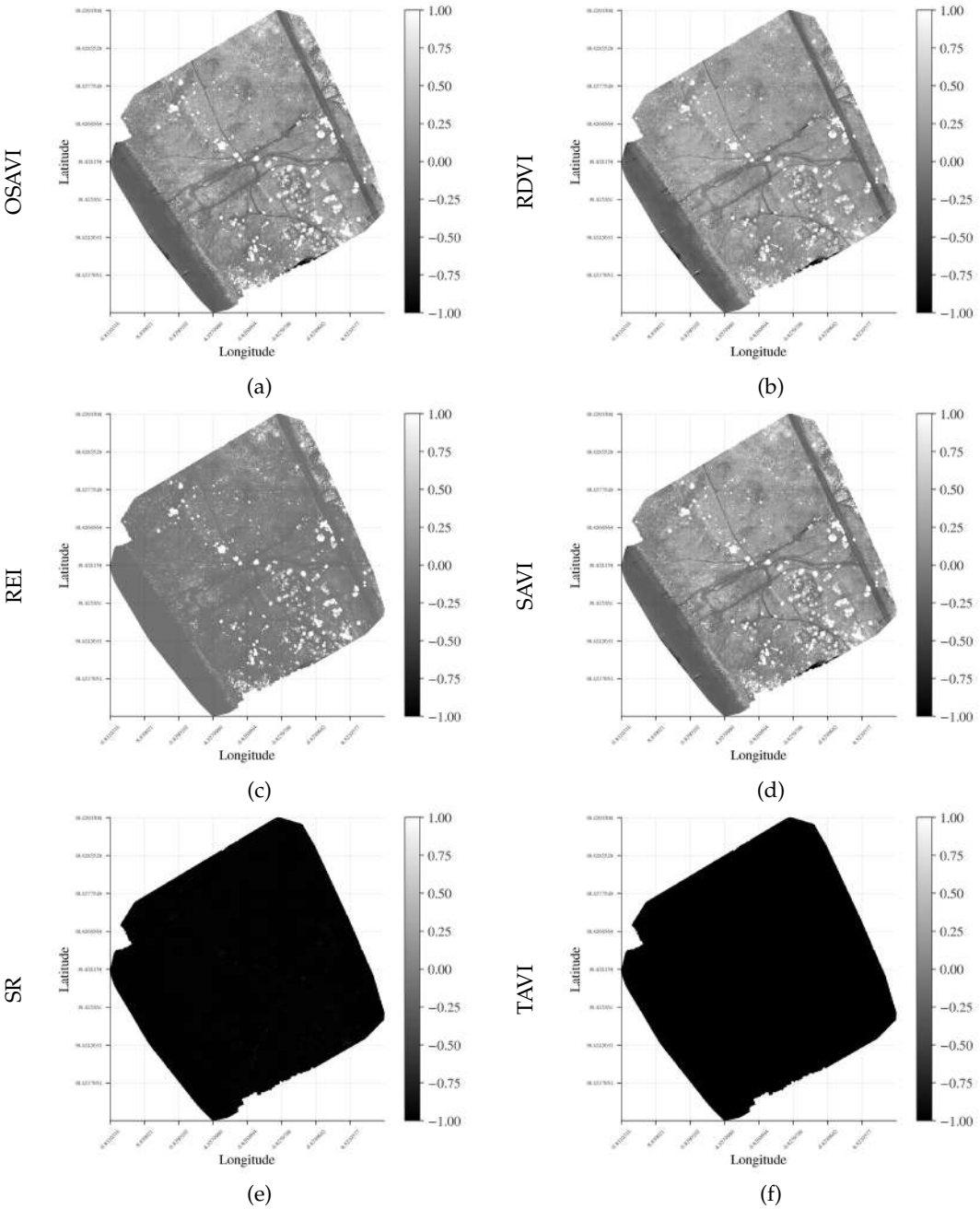

Figure A.4: OSAVI, RDVI, REI, SAVI, SR and TAVI (Map A).

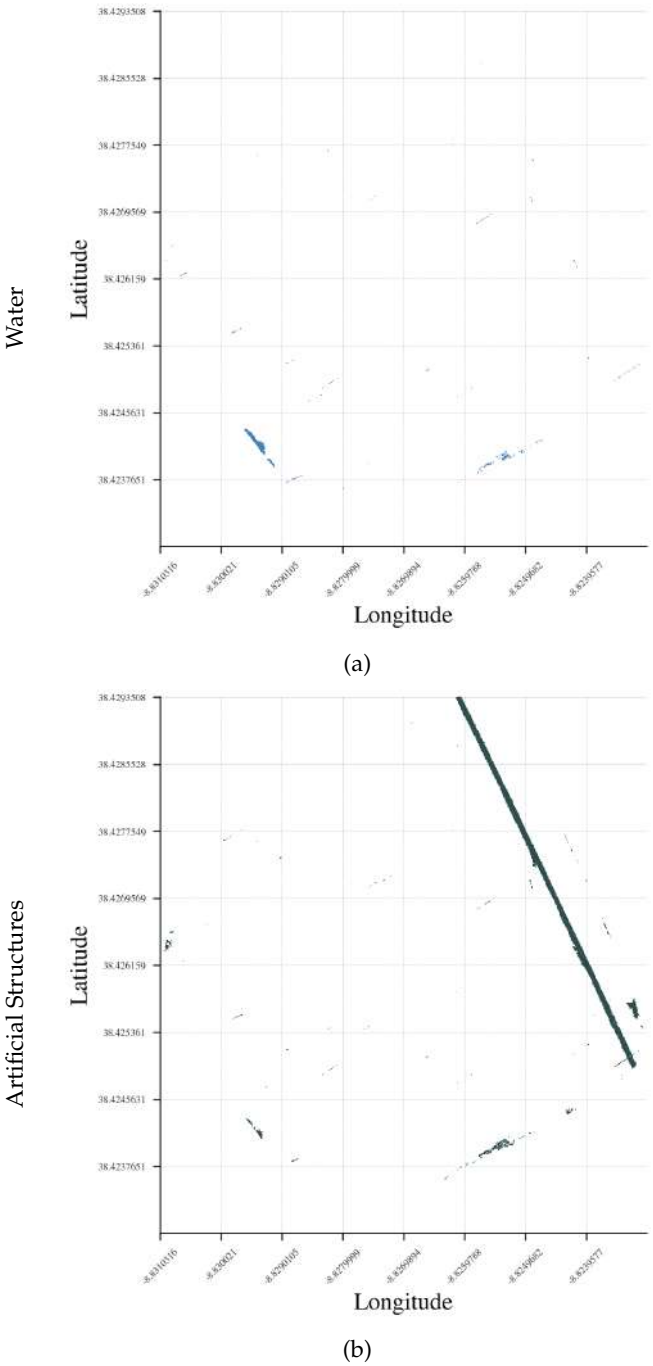

Figure A.5: Water and Artificial Structures (Map A).

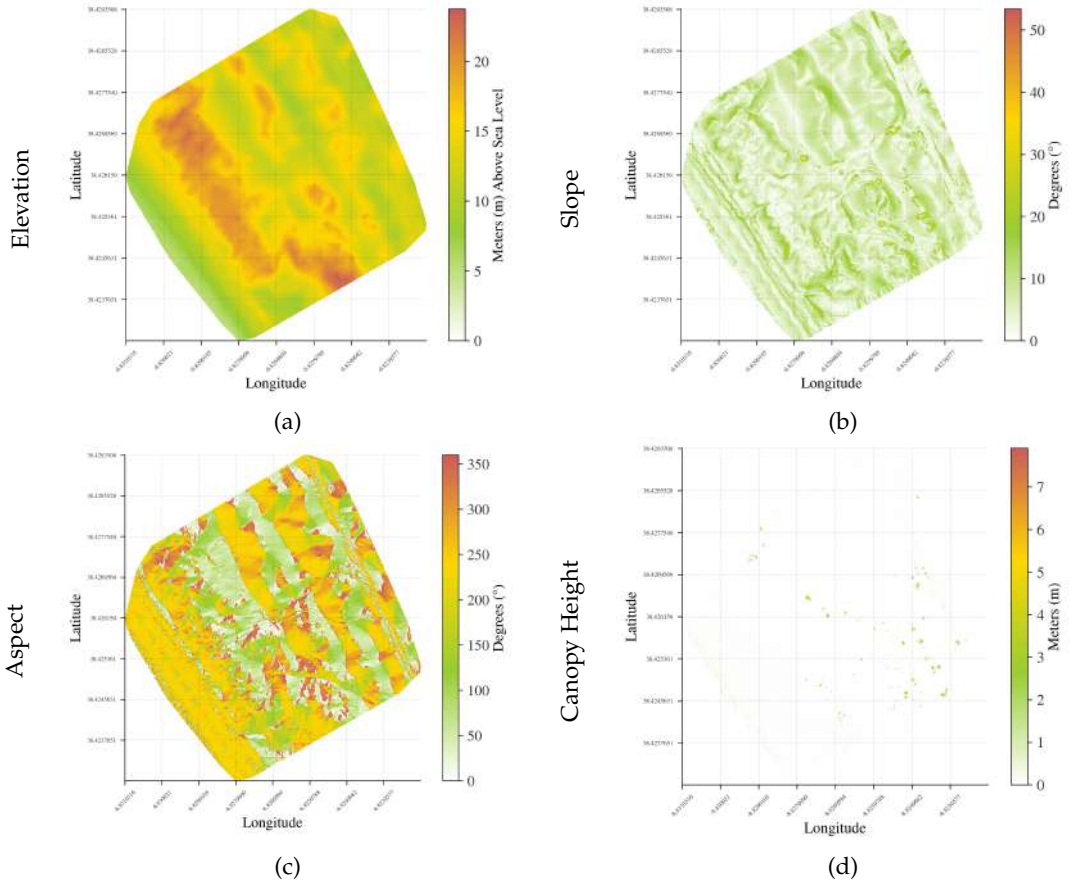

Figure A.6: Elevation, Slope, Aspect and Canopy Height (Map A).

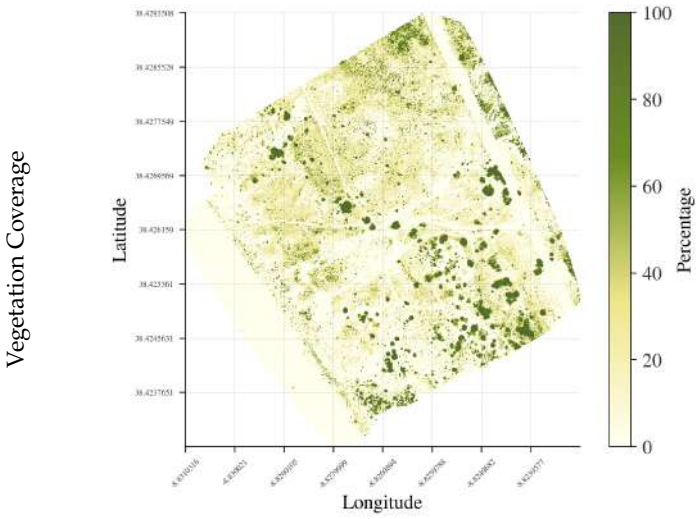

(a)

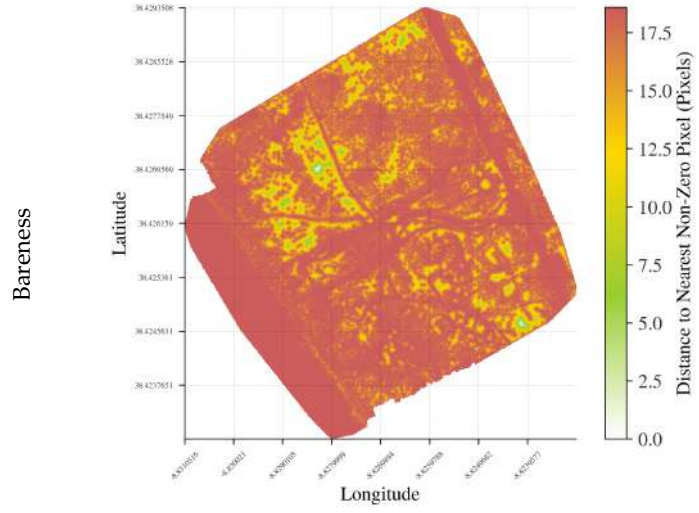

(b)

Figure A.7: Vegetation Coverage and Bareness (Map A).

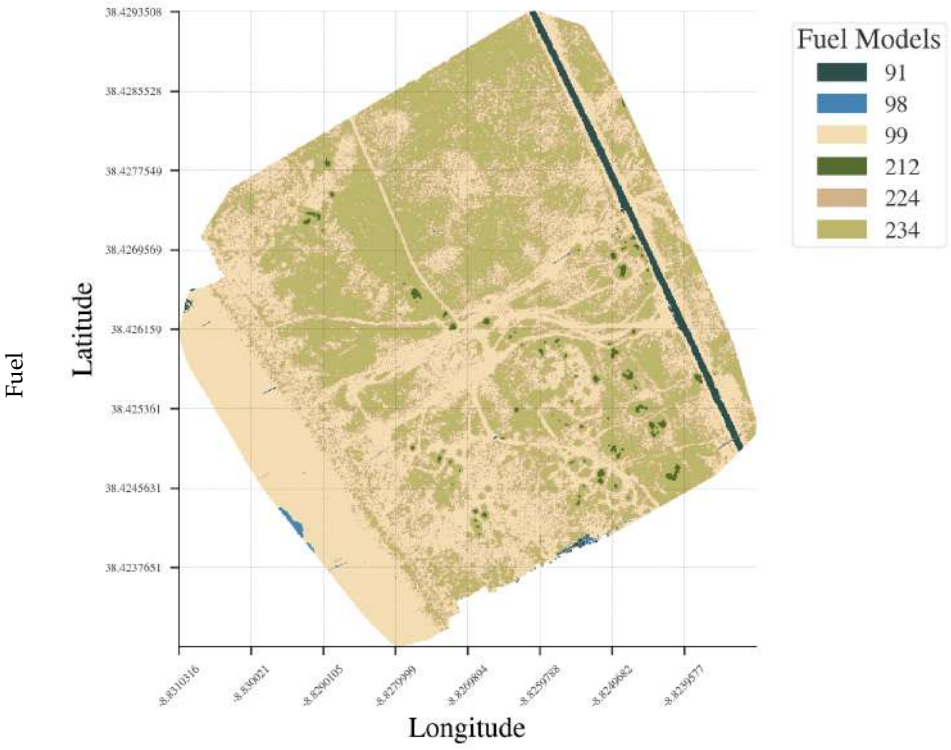

(b)

Figure A.8: Fuel (Map A).

B

NABU Results (Map B)

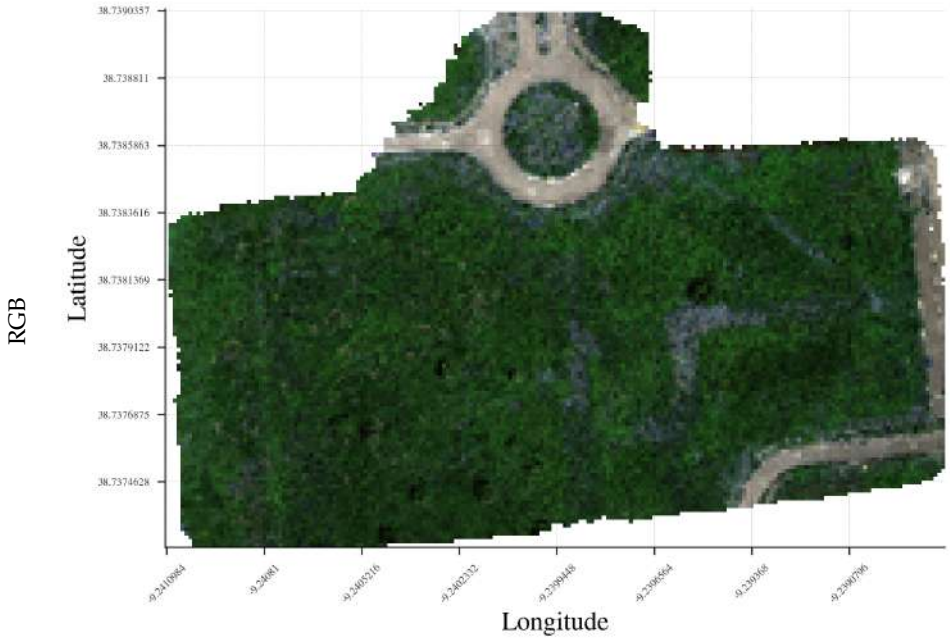

(a)

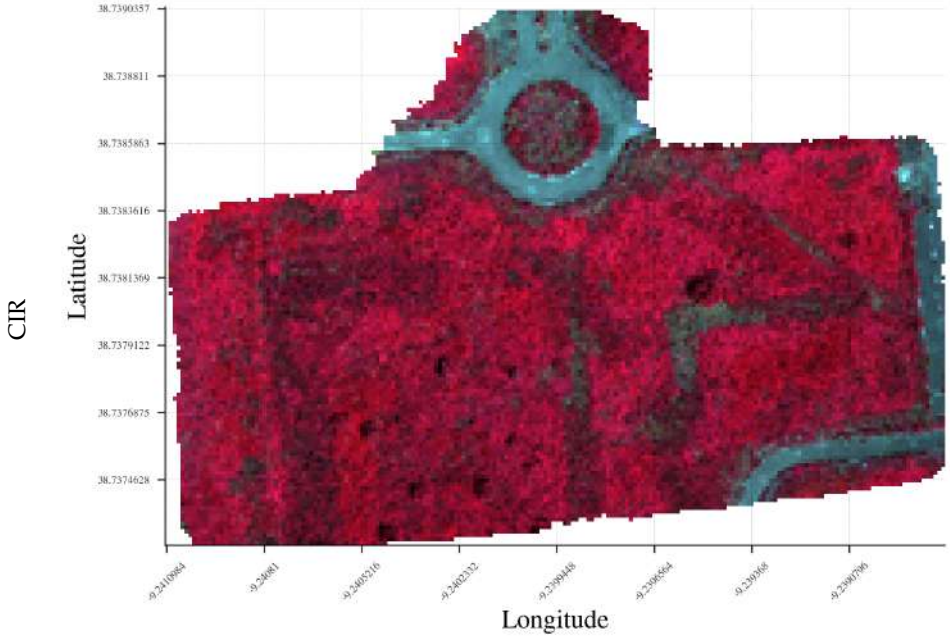

(b)

Figure B.1: RGB and CIR (Map B).

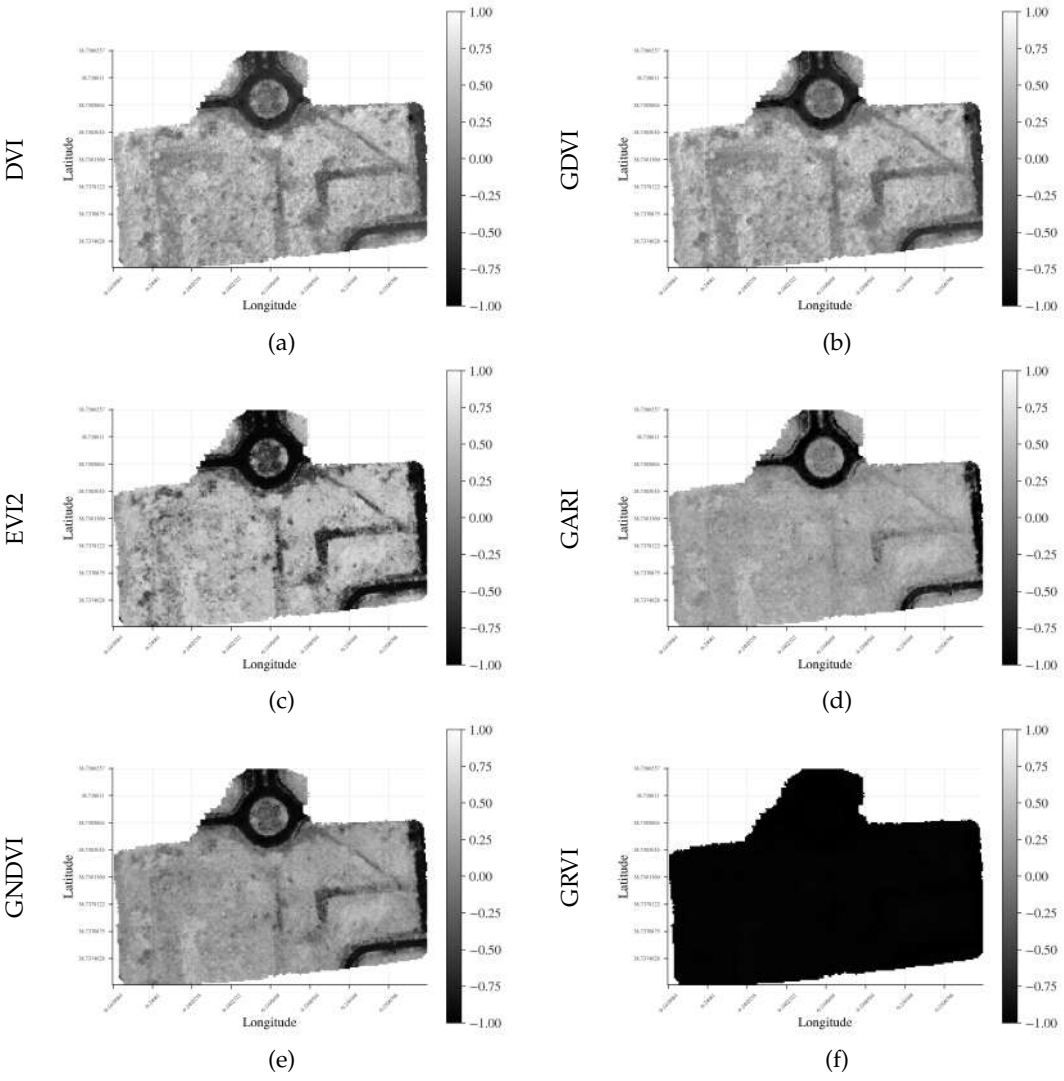

Figure B.2: DVI, GDVI, EVI2, GARI, GNDVI and GRVI (Map B).

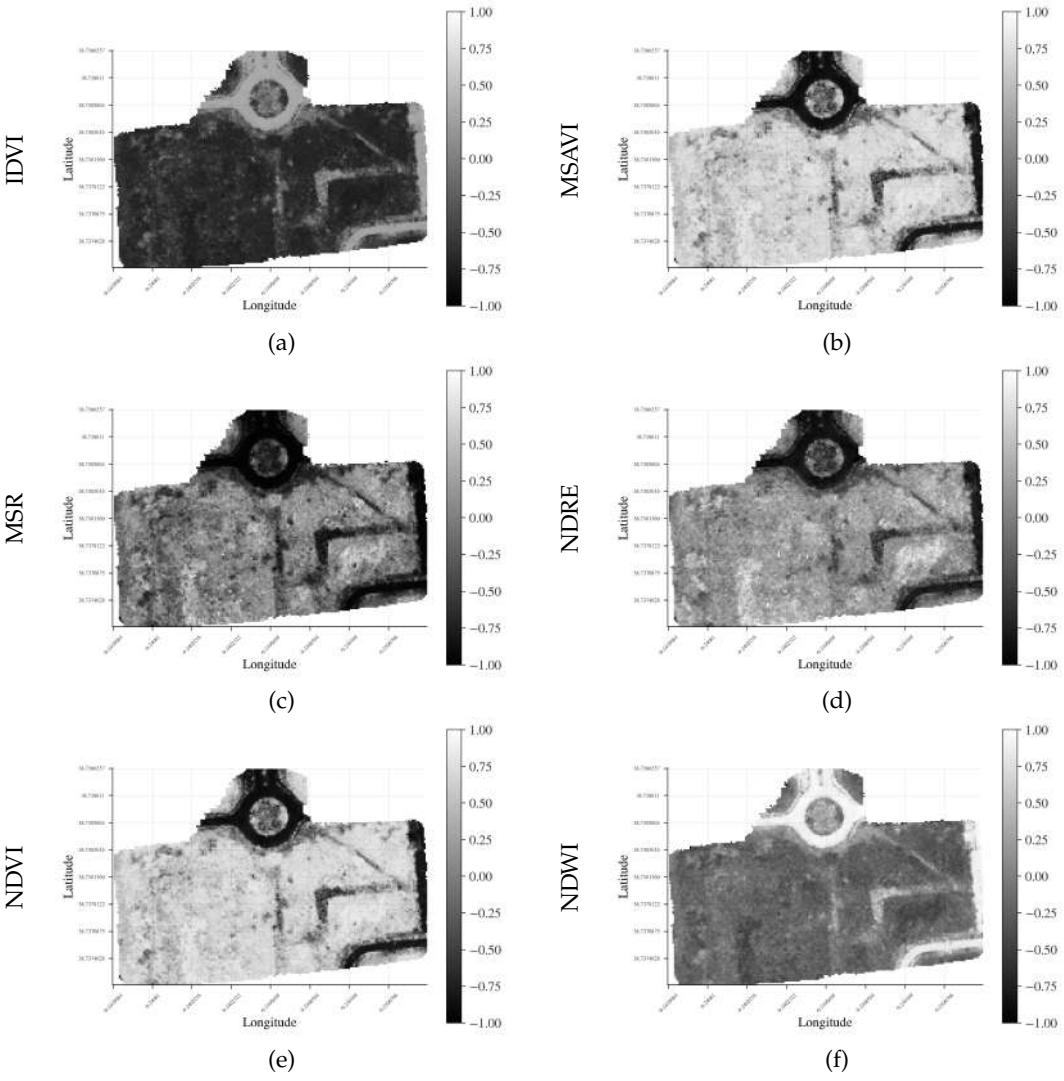

Figure B.3: IDVI, MSAVI, MSR, NDRE, NDVI and NDWI (Map B).

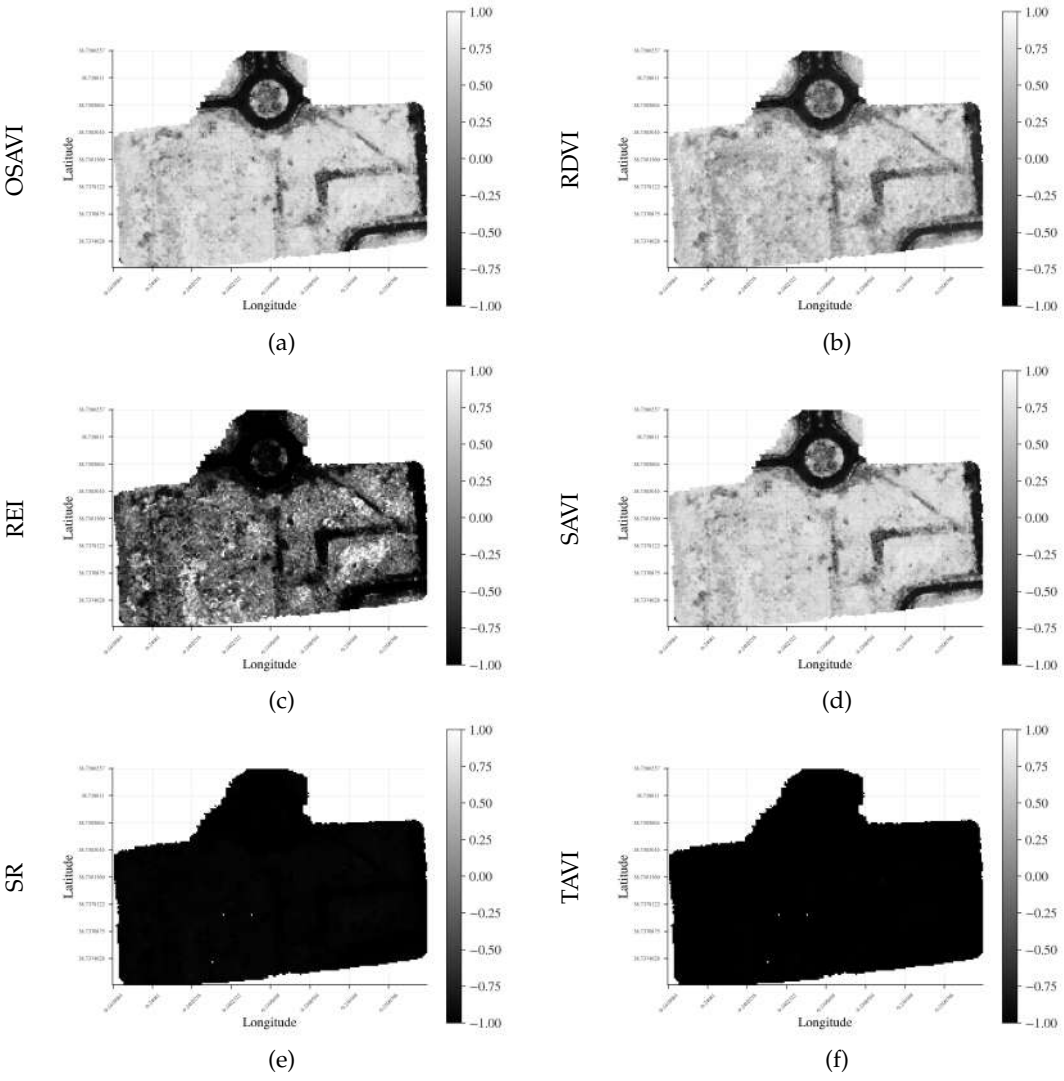

Figure B.4: OSAVI, RDVI, REI, SAVI, SR and TAVI (Map B).

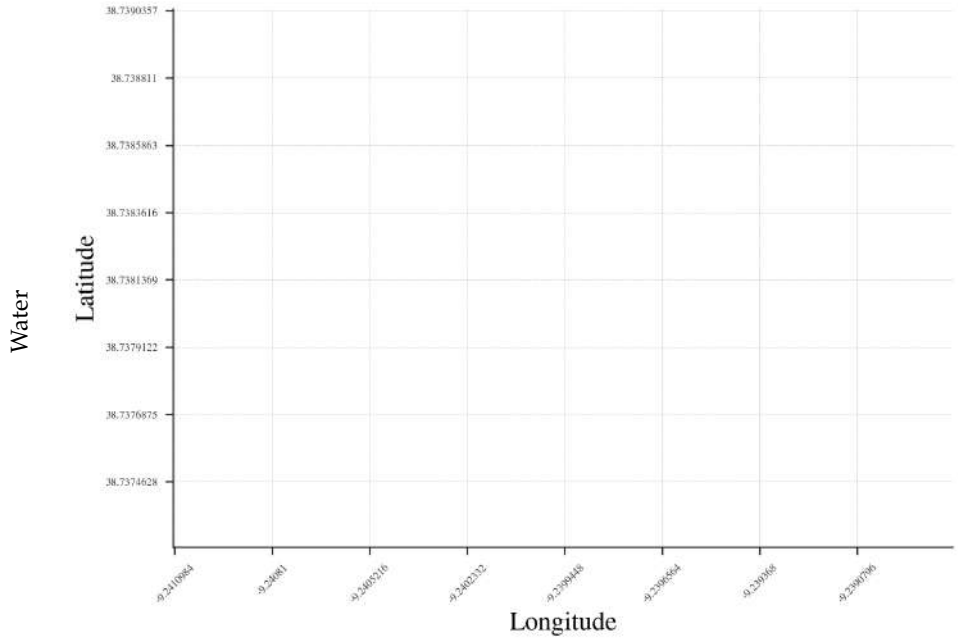

(a)

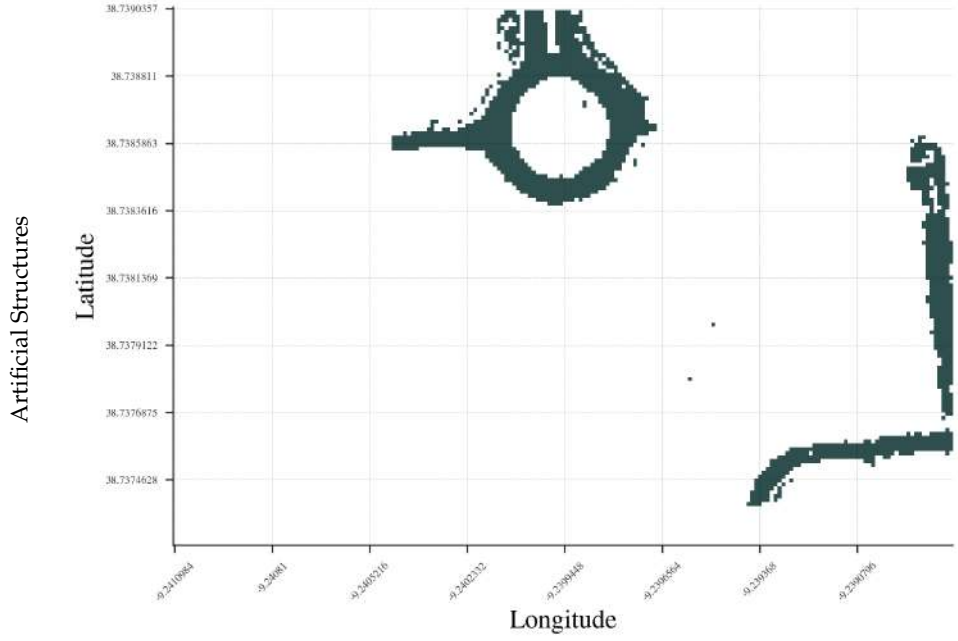

(b)

Figure B.5: Water and Artificial Structures (Map B).

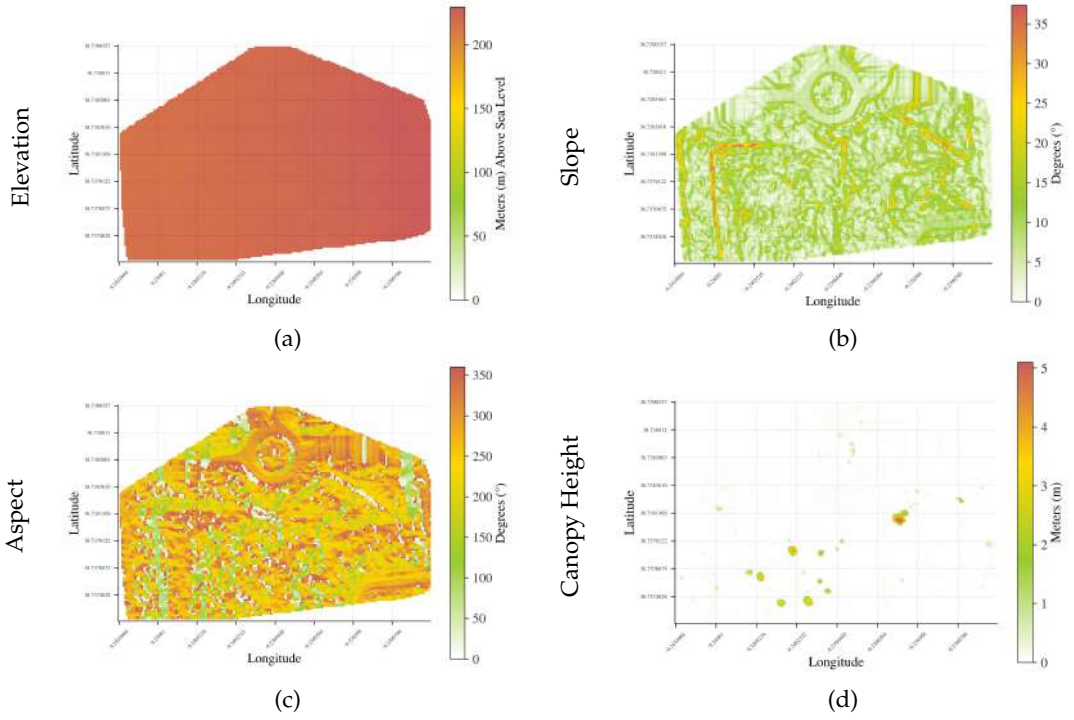

Figure B.6: Elevation, Slope, Aspect and Canopy Height (Map B).

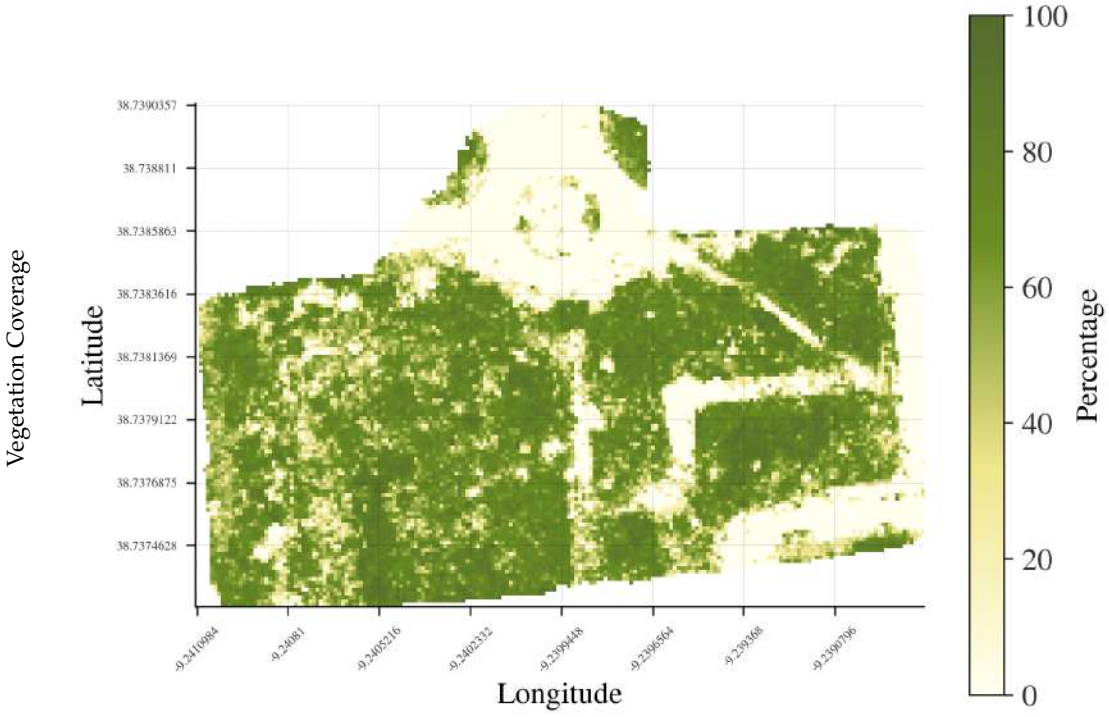

(a)

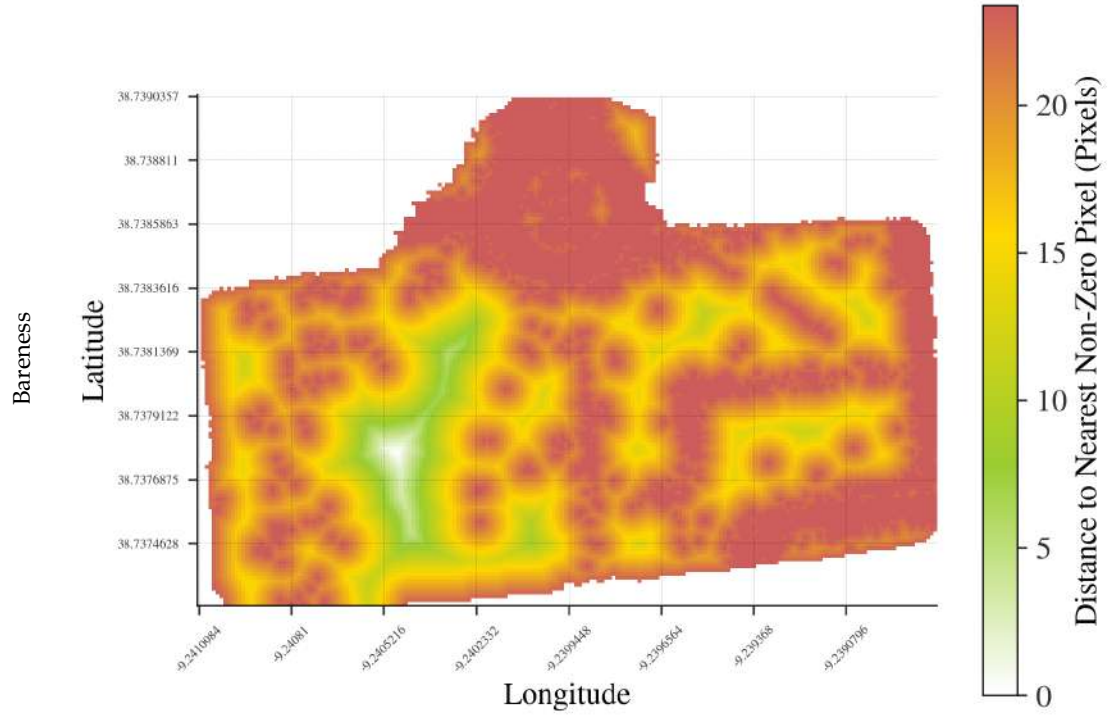

(b)

Figure B.7: Vegetation Coverage and Bareness (Map B).

(b)

Figure B.8: Fuel (Map B).

C

NABU Results (Map C)

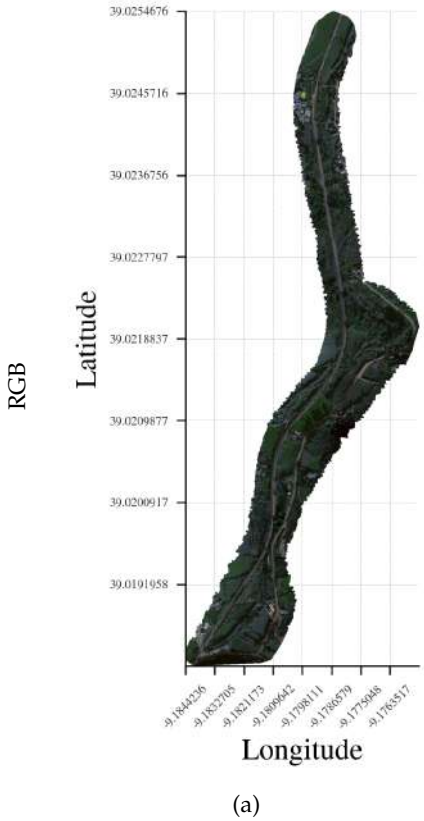

(a)

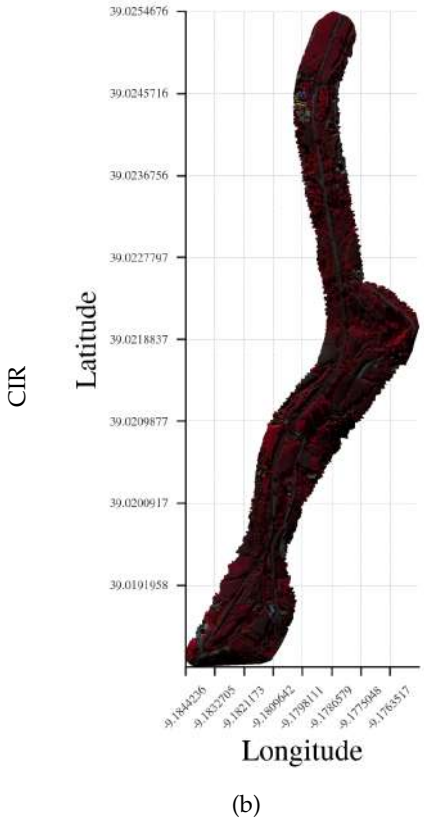

(b)

Figure C.1: RGB and CIR (Map C).

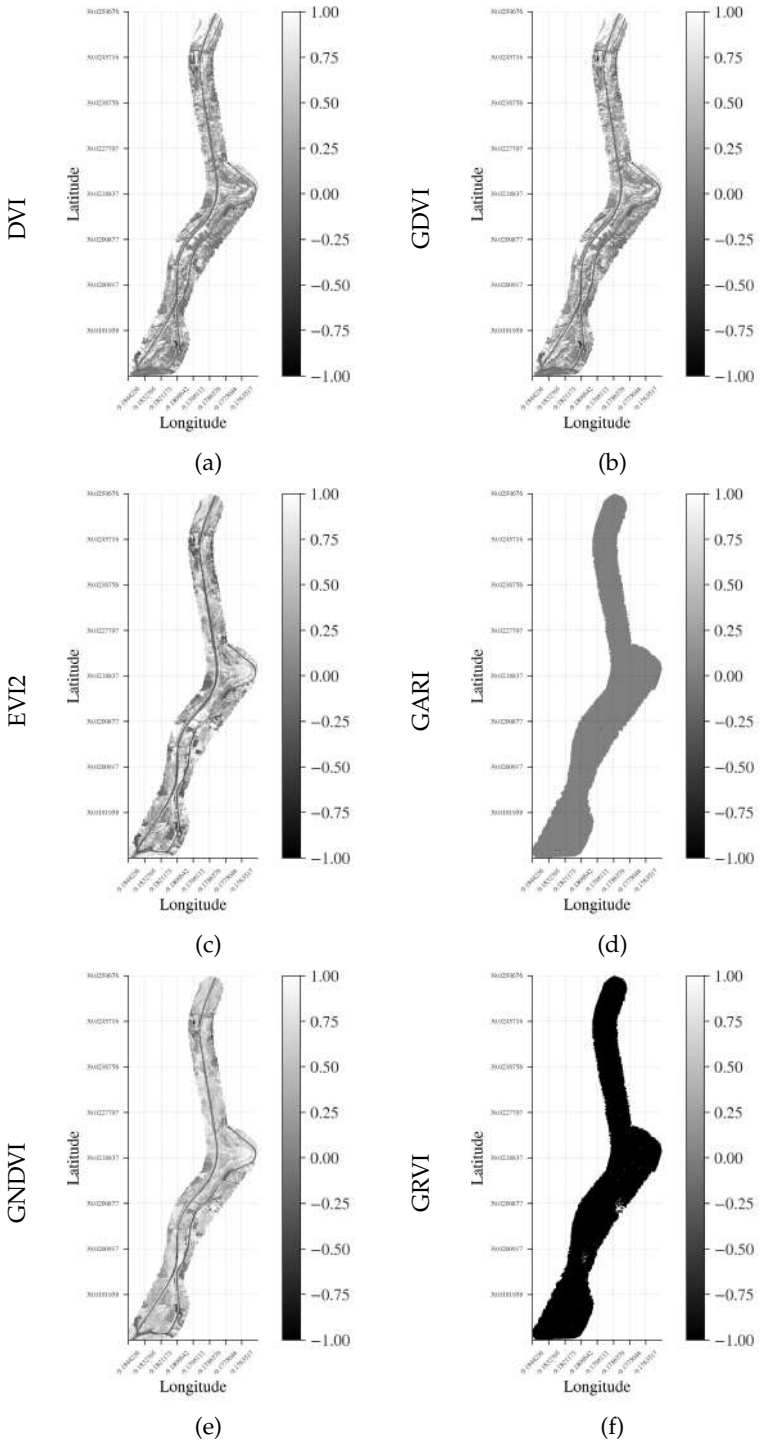

Figure C.2: DVI, GDVI, EVI2, GARI, GNDVI, and GRVI (Map C).

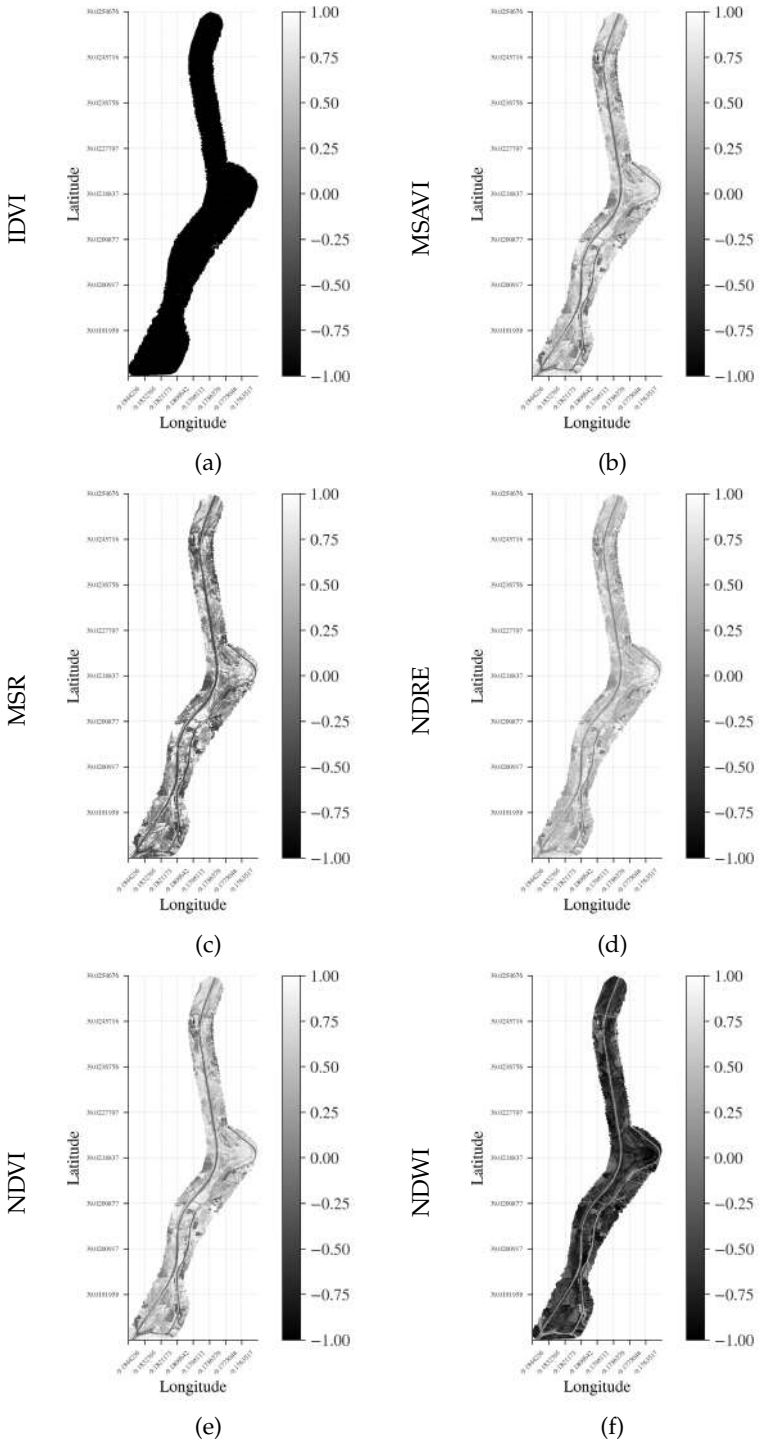

Figure C.3: IDVI, MSAVI, MSR, NDRE, NDVI and NDWI (Map C).

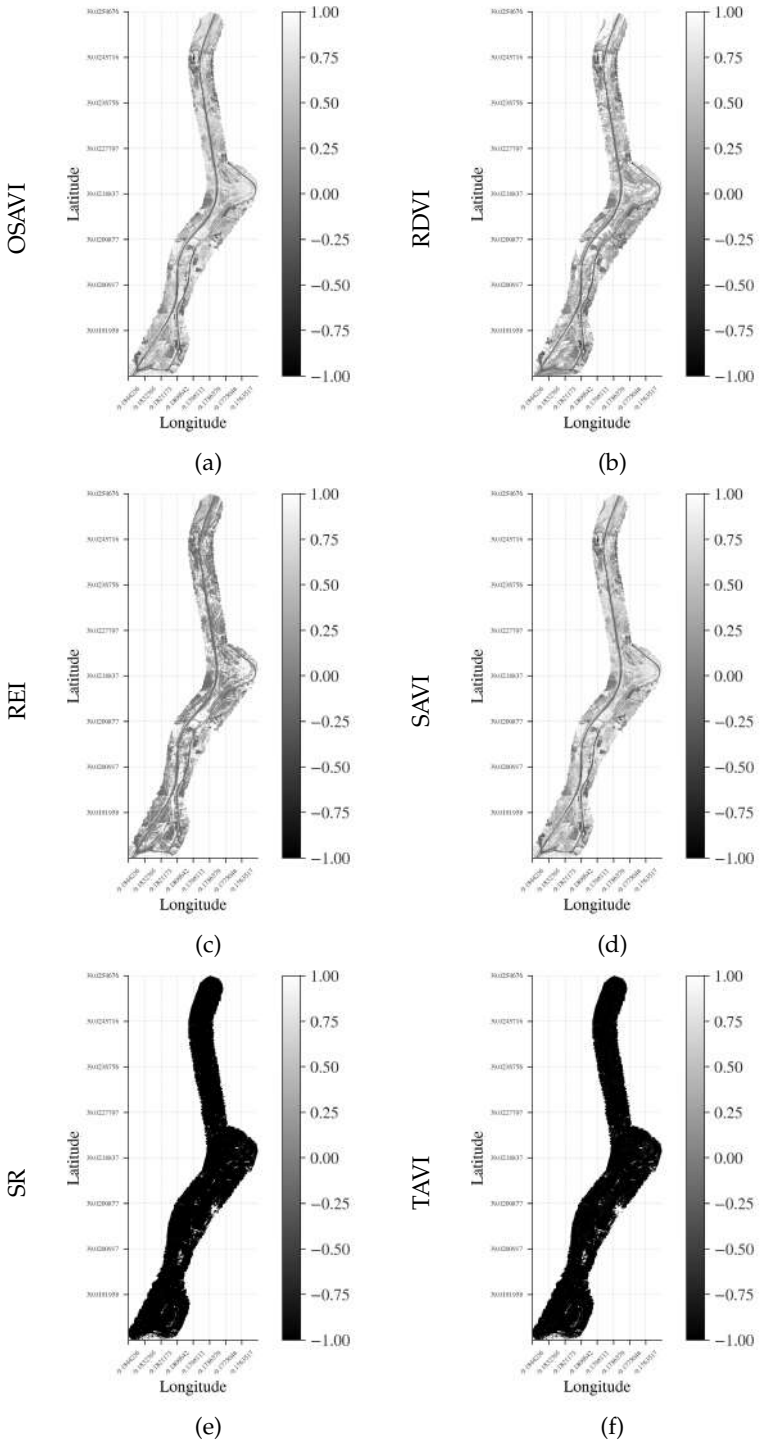

Figure C.4: OSAVI, RDVI, REI, SAVI, SR and TAVI (Map C).

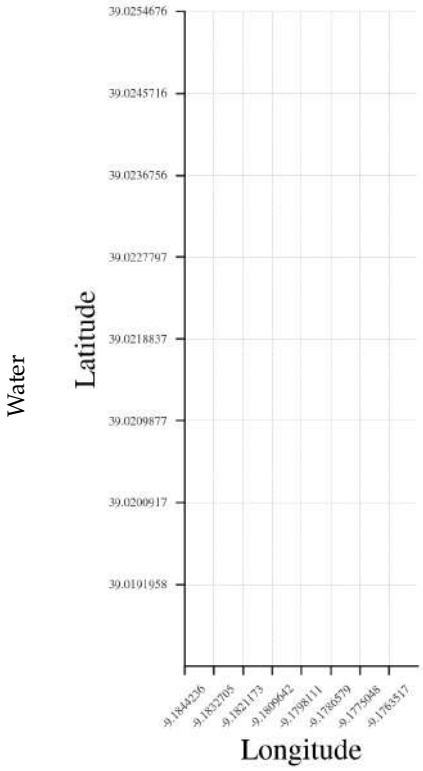

(a)

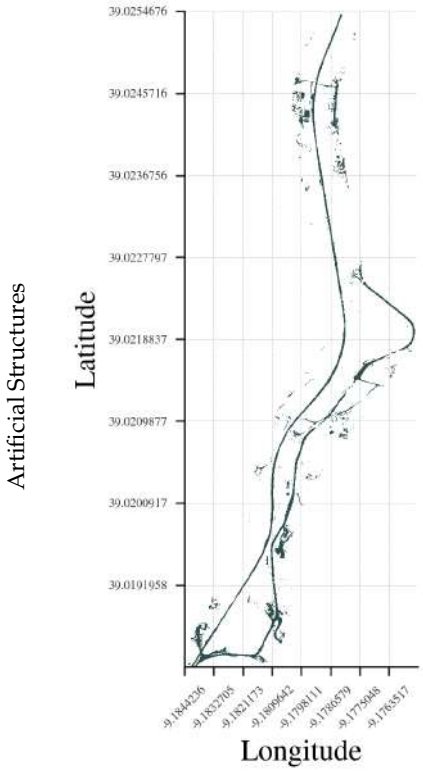

(b)

Figure C.5: Water and Artificial Structures (Map C).

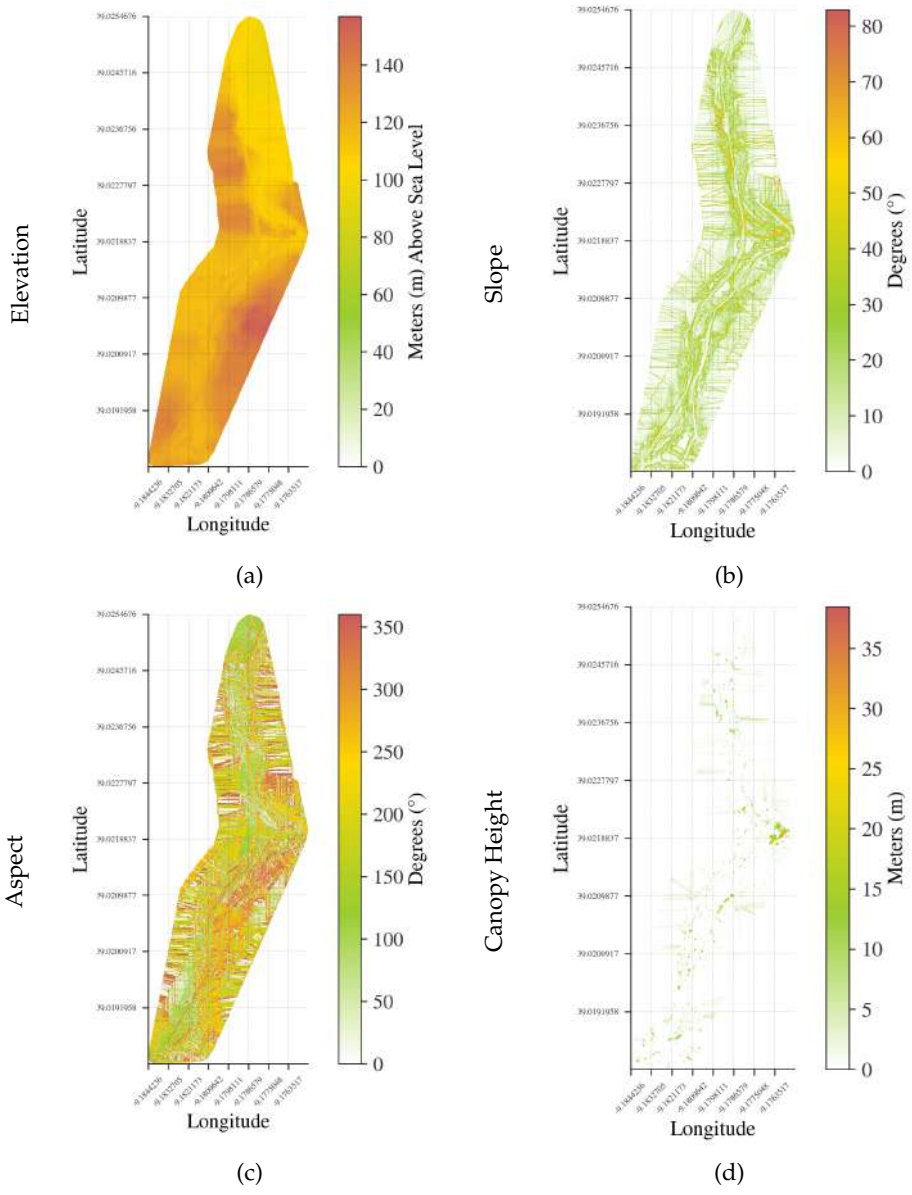

Figure C.6: Elevation, Slope, Aspect and Canopy Height (Map C).

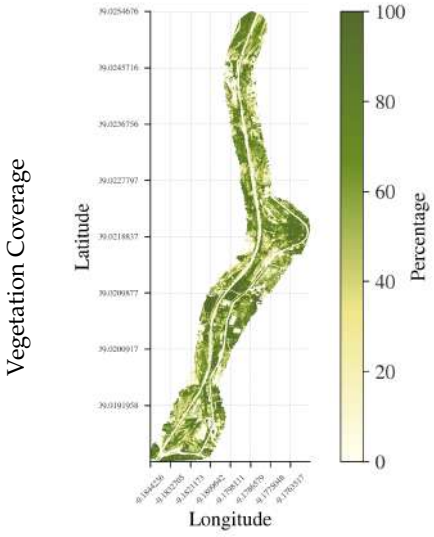

(a)

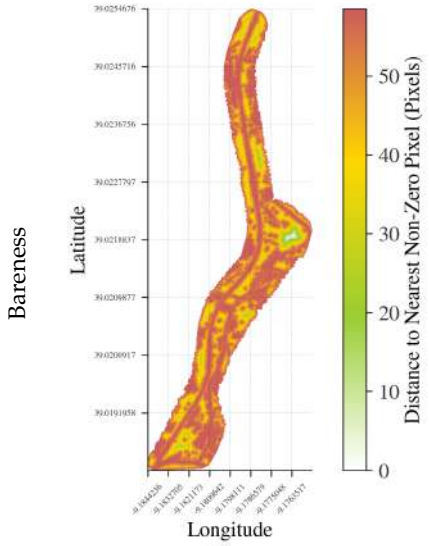

(b)

Figure C.7: Vegetation Coverage and Bareness (Map C).

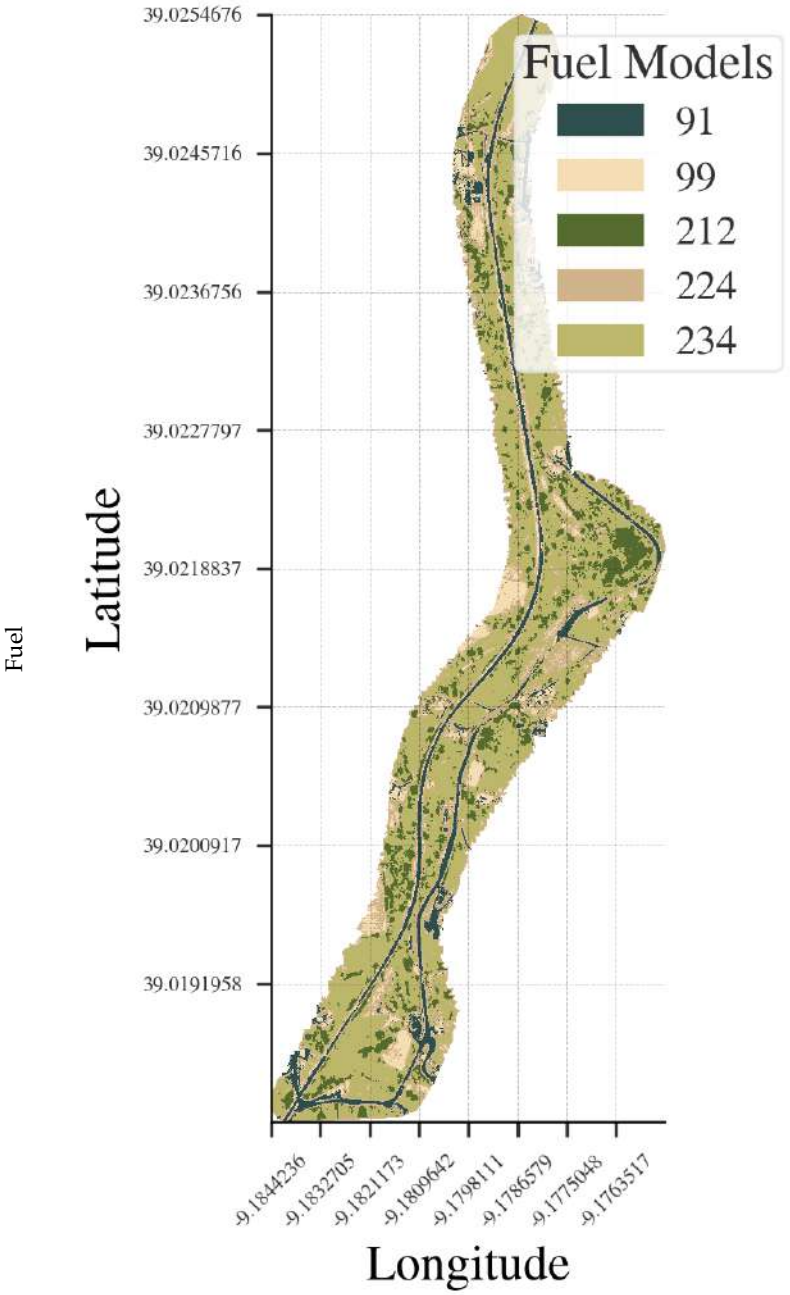

(b)

Figure C.8: Fuel (Map C).

D

NFDRS 2016 Fire Model Elements

Table D.1: Equations for the Spread Component (SC) and the Energy Release Component (ERC) of the NFDRS 2016 fire model (Weighting Factors). Adapted from Andrews, 2018.

Element	SC	ERC
Weighting Factors Based on Surface Area	$A_{ij} = \sigma_{ij} \times \frac{(w_0)_{ij}}{(\rho_p)_{ij}}$ $A_i = \sum_j A_{ij}$ $A_\tau = \sum_i A_i$ $f_{ij} = \frac{A_{ij}}{A_i}$ $f_i = \frac{A_i}{A_\tau}$	Same as SC
Weighting Factors Based on Fuel Load	N/A N/A N/A N/A	$L_i = \sum_j (w_0)_{ij}$ $L_\tau = \sum_i L_i$ $k_{ij} = \sum_j \frac{(w_0)_{ij}}{L_i}$ $k_i = \frac{L_i}{L_\tau}$

$i = 1 \Rightarrow$ Dead fuel. $i = 2 \Rightarrow$ Live fuel.
$j = 1, 2, 3, 4 \Rightarrow$ 1H, 10H, 100H and 1000H values.

Table D.2: Equations for the Spread Component (SC) and the Energy Release Component (ERC) of the NFDRS 2016 fire model (Moisture of Extinction). Adapted from Andrews, 2018.

Element	SC	ERC
Live Fuel Moisture of Extinction	$(M_x)_2 = 2.9 \times W \times (1 - \frac{M_{f,dead}}{(M_x)_1}) - 0.226$ $W = \frac{\sum_j (w_0)_{1j} \times e^{-138/\sigma_{1j}}}{\sum_j (w_0)_{2j} \times e^{-500/\sigma_{2j}}}$ $M_{f,dead} = \frac{\sum_j (M_f)_{1j} (w_0)_{1j} \times e^{-138/\sigma_{1j}}}{\sum_j (w_0)_{1j} \times e^{-138/\sigma_{1j}}}$	Same as SC

$i = 1 \Rightarrow$ Dead fuel. $i = 2 \Rightarrow$ Live fuel.
$j = 1, 2, 3, 4 \Rightarrow$ 1H, 10H, 100H and 1000H values.

Table D.3: Equations for the Spread Component (SC) and the Energy Release Component (ERC) of the NFDRS 2016 fire model (Characteristic Values for Live and Dead Categories). Adapted from Andrews, 2018.

Element	SC	ERC
Net Fuel Loaf (lb/ft^2)	$(w_n)_{ij} \times (1 - ((S_\tau)_{ij})$ $(w_n)_i = \sum_j f_{ij} \times (w_n)_{ij}$	$(w_n)_{ij} \times (1 - ((S_\tau)_{ij})$ $(w_n)_i = \sum_j (w_n)_{ij}$
Heat Content (Btu/lb)	$h_1 = h_2$	Same as SC
Effective Mineral Content	$(S_e)_1 = (S_e)_2 = 0.01$	Same as SC
Mineral Damping Coefficient	$(\eta_s)_i = 0.174 \times (S_e)_i^{-0.19}, max = 1$	Same as SC
Moisture Content (%)	$(M_f)_i = \sum_j f_{ij} \times (M_f)_{ij}$	$(M_f)_i = \sum_j k_{ij} \times (M_f)_{ij}$
Moisture Damping Coefficient	$(\eta_M)_i = 1 - 2.59 \times (\gamma_M)_i + 5.11 \times (\gamma_M)_i^2 - 3.52 \times (\gamma_M)_i^3$ $(\gamma_M)_i = \frac{(M_f)_i}{(M_x)_i}, max = 1$	$(\eta_M)_i = 1 - 2.0 \times (\gamma_M)_i + 1.5 \times (\gamma_M)_i^2 - 0.5 \times (\gamma_M)_i^3$ $(\gamma_M)_i = \frac{(M_f)_i}{(M_x)_i}, max = 1$
SA/V Ratio (ft^2/ft^3)	$\sigma_i = \sum_i f_{ij} \times \sigma_{ij}$	$\sigma_i = \sum_i k_{ij} \times \sigma_{ij}$

$i = 1 \Rightarrow$ Dead fuel. $i = 2 \Rightarrow$ Live fuel.
$j = 1, 2, 3, 4 \Rightarrow$ 1H, 10H, 100H and 1000H values.

Table D.4: Equations for the Spread Component (SC) and the Energy Release Component (ERC) of the NFDRS 2016 fire model (Fuel Bed Characteristic Values). Adapted from Andrews, 2018.

Element	SC	ERC
SA/V Ratio (ft^2/ft^3)	$\sigma = \sum_{ij} f_i \times \sigma_i$	$\sigma = \sum_{ij} k_i \times \sigma_i$
Mean Bulk Density (lb/ft^3)	$\rho_b = \frac{1}{\delta} \sum_i \sum_j (w_0)_{ij}$	$\rho_b = \frac{1}{\delta} \sum_i \sum_j (w_0)_{ij}, i \in [1, 3]$
Mean Packing Ratio	$\beta = \sum_i \sum_j \frac{\rho_b)_{ij}}{\rho_p)_{ij}}$	Same as SC
Optimum Packing Ratio	$\beta_o p = 3.348 \times \sigma^{-0.8189}$	Same as SC

$i = 1 \Rightarrow$ Dead fuel. $i = 2 \Rightarrow$ Live fuel.
$j = 1, 2, 3, 4 \Rightarrow$ 1H, 10H, 100H and 1000H values.

Table D.5: Equations for the Spread Component (SC) and the Energy Release Component (ERC) of the NFDRS 2016 fire model (Wind and Slope). Adapted from Andrews, 2018.

Element	SC	ERC
Slope Factor	$\phi_S = 5.27 \times \beta^- 0.3 \times tan(\phi)^2$	N/A
Wind Factor	$\phi_W = C \times (U_{20} \times 88 \times WAF)^B \times \frac{\beta}{\beta_o p}^- E$	N/A
	$C = 7.47 \times e^{-0.133 \times \sigma^{0.55})}$	N/A
	$B = 0.025 \times \sigma^{0.54}$	N/A
	$E = 0.715 \times e^{-3.59 \times 10^{-4} \times \sigma}$	N/A
Wind Limit (ft/min)	$U = 0.9 \times I_R$	N/A

$i = 1 \Rightarrow$ Dead fuel. $i = 2 \Rightarrow$ Live fuel.
$j = 1, 2, 3, 4 \Rightarrow$ 1H, 10H, 100H and 1000H values.

Table D.6: Equations for the Spread Component (SC) and the Energy Release Component (ERC) of the NFDRS 2016 fire model (Heat Source). Adapted from Andrews, 2018.

Element	SC	ERC
Maximum Reaction Velocity ($min^{-}1$)	$\Gamma'_{max} = \sigma^{1.5} \times (495 + 0.0594 \times \sigma^{1.5})^{-1}$	Same as SC
Optimum Reaction Velocity ($min^{-}1$)	$\Gamma' = \Gamma'_{max} \times (\frac{\beta}{\beta_{op}})^{A} \times e^{A \times (1 - \frac{\beta}{\beta_{op}})}$	Same as SC
	$A = 133 \times \sigma^{-0.7913}$	Same as SC
Reaction Intensity (Btu/ft^2-min)	$I_R = \Gamma' \times \sum_i (w_n)_i \times h_i \times (\eta_M)_i \times (\eta_S)_i$	$I_R = \Gamma' \times \sum_i k_i \times (w_n)_i \times h_i \times (\eta_M)_i \times (\eta_S)_i$
Propagating Flux Ratio	$\xi = (192 + 0.2595 \times \sigma)^{-1} \times e^{(0.792 + 0.681 \times \sigma^{0.5}) \times (\beta + 0.1)}$	N/A
Heat Source	$I_R \times \xi \times (1 + \phi_W + \phi_S)$	N/A

$i = 1 \Rightarrow$ Dead fuel. $i = 2 \Rightarrow$ Live fuel.
$j = 1, 2, 3, 4 \Rightarrow$ 1H, 10H, 100H and 1000H values.

Table D.7: Equations for the Spread Component (SC) and the Energy Release Component (ERC) of the NFDRS 2016 fire model (Heat Sink). Adapted from Andrews, 2018.

Element	SC	ERC
Heat of Pre-Ignition	$(Q_{ig})_{ij} = 250 + 11.16 \times (M_f)_{ij}$	N/A
Heat Sink (Btu/ft^3)	$\rho_b \times \sum_i f_i \sum_j f_{ij} \times e^{\frac{-138}{\sigma_{ij}}} \times (Q_{ig})_{ij}$	N/A

$i = 1 \Rightarrow$ Dead fuel. $i = 2 \Rightarrow$ Live fuel.
$j = 1, 2, 3, 4 \Rightarrow$ 1H, 10H, 100H and 1000H values.

Table D.8: Equations for the Spread Component (SC) and the Energy Release Component (ERC) of the NFDRS 2016 fire model (Rate of Spread). Adapted from Andrews, 2018.

Element	SC	ERC
Base Rate of Spread (ft/min)	$R_0 = \frac{I_R \times \xi}{\rho_b \times \sum_i f_i \sum_j f_{ij} \times e^{\frac{-138}{\sigma_{ij}}} \times (Q_{ig})_{ij}}$	N/A
Rate of Spread (ft/min)	$R = R_0 \times (1 + \phi_W + \phi_S)$	N/A

$i = 1 \Rightarrow$ Dead fuel. $i = 2 \Rightarrow$ Live fuel.
$j = 1, 2, 3, 4 \Rightarrow$ 1H, 10H, 100H and 1000H values.

Table D.9: Equations for the Spread Component (SC) and the Energy Release Component (ERC) of the NFDRS 2016 fire model (Flame Length). Adapted from Andrews, 2018.

Element	SC	ERC
Residence Time (min)	N/A	$t_\gamma = \frac{384}{\sigma}$
Heat per Unit Area (Btu/ft^2)	N/A	$H_A = I_R \times t_\gamma$
Flame Length (ft)	N/A	$F_B = 0.45 \times I_B^{0.46}$
Fireline Intensity (Btu/ft/sec)	N/A	$I_B = I_R \times t_\gamma \times \frac{R}{60}$

$i = 1 \Rightarrow$ Dead fuel. $i = 2 \Rightarrow$ Live fuel.
$j = 1, 2, 3, 4 \Rightarrow$ 1H, 10H, 100H and 1000H values.

Table D.10: Equations for the Spread Component (SC) and the Energy Release Component (ERC) of the NFDRS 2016 fire model (NFDRS Indices and Components). Adapted from Andrews, 2018.

Element	SC	ERC
Spead Component (SC)	$SC = ROUNDD(R)$	N/A
Energy Release Component (ERC)	N/A	$ERC = ROUNDD(0.04 \times H_A)$
Buring Index (BI)	N/A	$BI = ROUND(3.01 \times (R \times 0.04 \times H_A)^{0.46})$

$i = 1 \Rightarrow$ Dead fuel. $i = 2 \Rightarrow$ Live fuel.
$j = 1, 2, 3, 4 \Rightarrow$ 1H, 10H, 100H and 1000H values.

E

Fuel Model Specifications

Table E.1: Fuel model component values.

Model	ID	Depth	Fuel Load						SA/V						PC	HX	WAF
			1H	10H	100H	1000H	Arb.	Herb.	1H	10H	100H	1000H	Herb.	Arb.			
F-RAC	214	0.05	3.75	2.00	1.00	1.00	1.18	0.00	6500	6500	6500	6500	0	4500	20500	0.28	0.15
M-CAD	221	0.63	4.54	1.87	0.61	0.61	9.08	0.00	6000	6000	6000	6000	0	5000	20000	0.30	0.20
M-F	225	0.30	4.50	1.50	0.50	0.50	0.48	2.35	6000	6000	6000	6000	8000	4500	19500	0.35	0.20
V-Hb	232	0.35	0.30	0.00	0.00	0.00	0.00	1.20	6000	6000	6000	6000	6000	0	19000	0.24	0.35
F-PIN	213	0.10	6.50	1.50	0.00	0.00	0.00	0.00	5500	5500	5500	5500	0	0	20500	0.45	0.25
M-PIN	227	0.50	7.21	3.00	0.00	0.00	6.89	0.00	5500	5500	5500	5500	0	6000	21000	0.40	0.20
M-H	226	0.10	2.71	1.00	0.00	0.00	0.10	0.66	5500	5500	5500	5500	8000	4500	20500	0.30	0.20
M-ESC	222	0.50	5.65	1.50	0.48	0.48	7.89	0.00	5000	5000	5000	5000	0	5500	20500	0.25	0.20
M-EUC	223	0.64	8.37	3.81	0.00	0.00	4.51	0.00	4700	4700	4700	4700	0	5000	21000	0.32	0.20
F-FOL	212	0.15	2.67	1.27	0.69	0.69	1.16	0.00	4500	4500	4500	4500	0	5000	20500	0.25	0.20
M-EUCd	224	0.40	1.37	2.89	1.59	1.59	1.84	0.00	4500	4500	4500	4500	0	5000	21000	0.26	0.20
V-MAb	234	0.50	6.00	0.50	0.00	0.00	7.50	0.00	4500	4500	4500	4500	0	4500	21000	0.35	0.35
V-MH	235	0.55	1.00	1.00	0.00	0.00	5.50	1.50	4500	4500	4500	4500	8500	4000	19500	0.25	0.35
F-EUC	211	0.32	4.63	2.96	1.27	1.27	1.12	0.00	4200	4200	4200	4200	0	5000	21000	0.26	0.30
V-Ha	231	0.60	0.65	0.15	0.00	0.00	0.40	2.35	4000	4000	4000	4000	5500	4000	19000	0.24	0.35
V-MAa	233	1.05	9.50	2.50	0.00	0.00	14.50	0.00	3500	3500	3500	3500	0	4000	21000	0.35	0.45
V-MMb	237	0.90	4.00	0.50	0.00	0.00	7.00	0.00	3000	3000	3000	3000	0	3000	20500	0.20	0.35
V-MMa	236	1.70	6.00	4.00	0.00	0.00	13.00	0.00	2500	2500	2500	2500	0	3000	20500	0.25	0.45
NB-BARE	99	0	0	0	0	0	0	0	0	0	0	0	0	0	0	0	0
NB-WAT	98	0	0	0	0	0	0	0	0	0	0	0	0	0	0	0	0
NB-URB	91	0	0	0	0	0	0	0	0	0	0	0	0	0	0	0	0

SA/V: Surface area per volume.

Arb.: Arboreous. Herb.: Herbaceous.

PC: Heat content. HX: Extinction moisture. WAF: Wind adjusting factor.

2023 Decision Support Platform for Enhanced Wildfire Prevention and Management Afonso Oliveira

NOVA SCHOOL OF SCIENCE & TECHNOLOGY